Dissertation

submitted to the
Combined Faculties for the Natural Sciences and for
Mathematics
of the Ruperto-Carola University of Heidelberg, Germany
for the degree of

Doctor of Natural Sciences

presented by

Dipl.-Phys. Dominik Hauser

born in Sigmaringen, Germany

Oral examination: 17 October 2007

Analysis of H.E.S.S. Data on the Supernova Remnants Kepler's SNR, Vela Junior and SN1006

and

The Smart Pixel Camera: A Camera for Future Cherenkov Telescopes

Referees: Prof. Dr. Werner Hofmann
Prof. Dr. Karl-Tasso Knöpfle

Abstract

One of the most violent events in our Universe is the death of a star in a supernova. The remnants of these supernovae are believed to be sources of the Galactic cosmic rays (CRs). However, it is still an open question which processes take place in the production of CRs. The CRs itself arrive isotropically on Earth, as they get deflected by interstellar magnetic fields. To study the acceleration regions of CRs, gamma rays which are produced in the vicinity of these regions are observed. In the very-high-energy waveband these gamma rays are detected with Imaging Atmospheric Cherenkov Telescopes making use of the atmosphere as a part of the detector. To date the H.E.S.S. experiment is the most sensitive telescope array in this field. In this work the analysis of H.E.S.S. data from three supernova remnants is presented and it is shown that two of them emit very-high-energy gamma rays. In the second part of this work a new type of camera for future arrays containing of multiple Imaging Atmospheric Cherenkov Telescopes is presented. It is shown that this camera is well-suited to be operated in such telescopes.

Kurzfassung

Eines der gewaltigsten Ereignisse in unserem Universum ist der Tod eines Sterns in einer Supernova. Die Reste dieser Supernoae werden als Quellen der galaktischen kosmischen Strahlung gehandelt. Allerdings ist noch immer nicht geklärt, welche Prozesse die Teilchen der kosmischen Strahlung erzeugen. Aufgrund der interstellaren Magnetfelder trifft die kosmische Strahlung isotrop auf der Erde auf. Um die Beschleunigung der Teilchen der kosmischen Strahlung zu erforschen wird Gamma-Strahlung beobachtet, welche im Umfeld der Beschleunigungsregionen erzeugt wird. Im Wellenlängenbereich der sehr hochenergetischen Strahlung wird bei der Abbildenden Atmospherischen Cherenkov Technik die Atmosphere als Teil des Detektors benutzt. Derzeit ist das H.E.S.S. Experiment das empfindlichste Teleskop-Array in diesem Bereich. In dieser Arbeit wird die Analyse von H.E.S.S. Daten dreier Supernovaüberreste vorgestellt und es wird gezeigt, daß zwei davon sehr hochenergetische Strahlung emittieren. Im zweiten Teil der Arbeit wird eine neue Art Kamera für zukünftige Arrays, bestehend aus mehreren Cherenkov Teleskopen, vorgestellt. Es wird gezeigt, daß diese Kamera sehr gut geeignet ist in einem solchen Teleskop betrieben zu werden.

Contents

1 Introduction **1**

I Physical Background **3**

2 Supernovae and their Remnants **5**
- 2.1 Introduction 5
- 2.2 Types of SN Explosions 7
  - 2.2.1 Type Ia 8
  - 2.2.2 Type II, Ib, Ic 10
- 2.3 The Different Stages of SN Explosion 10
- 2.4 Particle Acceleration in Shock Fronts 13
- 2.5 Hadronic and Leptonic Scenario of Particle Acceleration 15
  - 2.5.1 Hadronic Scenario 15
  - 2.5.2 Leptonic Scenario 16
- 2.6 Determination of the Distance 18

3 H.E.S.S. **19**
- 3.1 Air Shower 19
  - 3.1.1 Electromagnetic Shower 19
  - 3.1.2 Hadronic Shower 20
  - 3.1.3 Cherenkov radiation 21
- 3.2 Imaging Atmospheric Cherenkov Technique 21
- 3.3 The H.E.S.S. Array 21
  - 3.3.1 Mount and Dish 22
  - 3.3.2 Camera 22
  - 3.3.3 Central Trigger 24

II Analysis of HESS data **25**

4 Analysis Technique **27**
- 4.1 Data Selection 27
- 4.2 Calibration 27
- 4.3 Image Cleaning 28
- 4.4 The Standard Analysis 28
  - 4.4.1 Hillas Parameters 28

4.4.2 Direction Reconstruction . . . 29
4.4.3 Image Cuts . . . 30
4.4.4 Muon Correction . . . 32
4.4.5 Background Estimation . . . 32
4.4.6 Energy Reconstruction . . . 36
4.4.7 Spectrum Determination . . . 37
4.4.8 Upper Limit Determination . . . 37

5 Kepler's SNR 43
5.1 H.E.S.S. Observations and Results . . . 44
5.2 Upper Limit on the Integrated Energy Flux . . . 45
5.3 Nature of the Accelerated Particles . . . 47
5.3.1 Hadronic Scenario . . . 48
5.3.2 Leptonic Scenario . . . 49
5.4 Comparison with Theory . . . 51
5.5 Distance . . . 53

6 RX J0852.0-4622 (Vela Junior) 55
6.1 H.E.S.S. Observations and Analysis . . . 56
6.2 Morphology . . . 56
6.2.1 General Morphology of the Remnant . . . 57
6.2.2 Width of the shell . . . 58
6.3 Spectral Analysis . . . 59
6.4 Comparison with X-rays . . . 62
6.5 Energy in Accelerated Protons . . . 63

7 SN1006 65
7.1 H.E.S.S. Observations and Analysis . . . 66
7.2 Results . . . 66
7.2.1 The whole Remnant . . . 66
7.2.2 Analysis on the north-eastern Spot . . . 67
7.2.3 Spectral Analysis . . . 71
7.2.4 Comparison with the CANGAROO result . . . 71

III Smart Pixel Camera 73

8 Components of the Smart Pixel Camera 75
8.1 Smart Pixel . . . 76
8.1.1 Trigger Logic . . . 77
8.1.2 Signal Integration . . . 78
8.1.3 Timing Information . . . 80
8.1.4 Anode Current Information . . . 80
8.1.5 Rate Measurement . . . 81
8.1.6 Temperature . . . 81
8.1.7 Further Monitoring . . . 82
8.1.8 Programmable Parameters on the Pixel . . . 82

8.2 Segment 82
8.3 Camera Controller 83
8.4 Trigger Management Board 84
8.5 Housing 87
8.6 Software 87

9 Tests with the Prototype **89**
9.1 Test Bench 90
9.2 Calibration of the Delays 91
9.3 Amplitude Measurement 93
    9.3.1 Calibration 93
    9.3.2 Amplitude Resolution 95
    9.3.3 Noise 96
9.4 Pixel Timing Information 98
    9.4.1 Time Measurement Resolution 98
    9.4.2 Effective Trigger Gate 99
    9.4.3 Diagnostic Power of the Time Measurement 99
9.5 Trigger Performance 101
    9.5.1 Pixel Threshold 101
    9.5.2 Discriminator Rate 101
    9.5.3 Accidental Rate 103
    9.5.4 Dead Time 103

Conclusion **105**

Bibliography **113**

Danksagung **115**

List of Figures

2.1 The SNRs in the Galaxy 7
2.2 Pressure, density and velocity in the SNR evolution 12
2.3 Second order Fermi acceleration 13
2.4 First order Fermi acceleration 14

3.1 Shower profiles from simulations 20
3.2 The H.E.S.S. telescope array 22
3.3 A H.E.S.S. telescope 23
3.4 Drawer of the H.E.S.S. cameras 23

4.1 Single photo electron spetrum in H.E.S.S. 29
4.2 Scheme of shower images 30
4.3 Simulated MRSW distributions 31
4.4 The two most common background estimations 34
4.5 Example of four wobble positions around Kepler's SNR 34
4.6 Off regions for the theta squared distribution 36
4.7 Construction of confidence intervals 38
4.8 Feldman&Cousins approach to get acceptance intervals 40

5.1 Kepler's SNR in radio, optical and X-rays 44
5.2 Significance sky map around Kepler 46
5.3 θ^2-distribution for Kepler's SNR 47
5.4 Kepler upper limits with $\Gamma = 2.0$ and $\Gamma = 3.0$ 48
5.5 Fit to the X-ray data from RXTE on Kepler's SNR 50
5.6 Kepler energy flux predicted by theory 52

6.1 Excess sky map of Vela Junior 57
6.2 Radial profiles of Vela Junior 58
6.3 Toy model for the emission of a shell 59
6.4 Radial profile of Vela Junior with a toy model fit 60
6.5 Spectrum of Vela Junior; Fit 1 60
6.6 Spectrum of Vela Junior; Fit 2 61
6.7 X-ray and gamma-ray excess from Vela Junior 62
6.8 Comparison of the radial profiles of Vela Junior 63

7.1 Excess sky map around SN1006 with ASCA contours 67
7.2 Significance sky map around SN1006 68

7.3 Slice through SN1006 69
7.4 Region for the analysis of the north-eastern spot 69
7.5 Significance distribution around SN1006 70
7.6 Significance versus time for the spot region of SN1006 70
7.7 Spectrum from the north-eastern spot of SN1006 71
7.8 SN1006 flux derived by H.E.S.S. and CANGAROO 72

8.1 Block diagram of the SPC 76
8.2 Smart Pixel 76
8.3 Block diagram of the SPE 77
8.4 Gated integrator 79
8.5 Phase error of the signal integration 79
8.6 Circuit diagram of the TAC 81
8.7 Multiplexing scheme 85
8.8 Trigger Management Board 86

9.1 The camera prototype 89
9.2 Light sources for the tests 90
9.3 Calibration of the discriminator delay 92
9.4 Calibration of the gate delay 94
9.5 Single photo electron spectrum 95
9.6 Relative resolution of the high gain channel 96
9.7 Square pedestal width over the number of photo electrons 97
9.8 Time resolution 99
9.9 Trigger timing 100
9.10 Arrival time vs. arrival time for coincidences 100
9.11 Threshold determination 102
9.12 Distribution of the threshold and its width 102
9.13 Discriminator rate 103
9.14 Calculated dead time 104

List of Tables

2.1 Different types and classifications of SNe 8

6.1 Spectra derived with different fits and cuts 61

8.1 Programmable parameters on the pixel electronics 82

9.1 Effective gates for the night sky background 98

Chapter 1

Introduction

Following the discovery of the cosmic rays in 1912 by Victor Hess an era of intense cosmic-ray research was began, giving birth to a new branch in physics, the particle physics. Particles like the positron, pions and kaons were all discovered in interactions of cosmic rays with atmospheric nuclei.

Some of the cosmic rays have very high energies, up to 10^{20} eV, and it is still an open question which objects are capable to accelerate particles to such energies. From about 10^9 eV up to the *knee* at 10^{14} eV the energy spectrum of the cosmic rays follows a simple power-law with a photon index of 2.7. Above the knee the spectrum steepens to an index of 3.0. The flux of particles with energies in the knee region is approximately 1 particle per square meter and year.

Supernova remnants (SNR), the remainders of the violent deaths of stars, are believed to accelerate cosmic rays to energies up to the knee and beyond. In the explosion of a supernova a shock front forms and fast charged particles gain energy by crossing the shock front over and over again until they are released from the shock as cosmic rays.

The majority of the cosmic-ray particles are charged and therefore they get deflected by interstellar magnetic fields, causing them to arrive at Earth isotropically. This makes it difficult to study the acceleration regions of the cosmic rays as these particles do not trace back to their sources. Fortunately, at the acceleration sites of cosmic rays gamma rays and neutrinos are produced in interactions of cosmic rays with the interstellar medium and photon fields. Being neutral, they are not disturbed by magnetic fields and allow a direct view to their sources.

The Earth's atmosphere is opaque for gamma rays. Satellites and balloons have been used to measure the gamma rays directly before they are absorbed in the atmosphere. Because of the steep spectrum of the cosmic rays, which is reproduced in the spectrum of the gamma rays, the limited detection area in satellites and balloons allows the detection only up to energies of 10^{11} eV. Beyond this point another detection principle, the Imaging Atmospheric Cherenkov Technique, has proven to be very successful. This technique allows to detect Cherenkov light emitted by very fast charged particles, which where produced in the interaction of the primary gamma ray with nuclei in the atmosphere. Gamma rays with energies in the range from 10^{11} eV to 10^{14} eV, called very

high energy (VHE) gamma rays, can be studied using this technique.
The most successful experiment in this field today is H.E.S.S., consisting of four imaging atmospheric Cherenkov telescopes situated in the Khomas highland of Namibia. One of the most remarkable results of the H.E.S.S. observations is the recording of the first resolved pictures in VHE gamma rays of supernova remnants (Aharonian et al. (2004b) and Aharonian et al (2005)). It was shown by these measurements that particles get accelerated in the shells of supernova remnants.
In this work the analysis of three supernova remnants, Kepler's SNR, Vela Junior and SN1006, is presented. Kepler's SNR has not been detected in VHE gamma rays yet. However, the derived upper limits on the flux allow to constrain parameters of a theoretical model of the emission in VHE gamma rays from Kepler's SNR. A lower limit on the distance is derived, lying well above the present lower limit. Detailed measurements of VHE gamma rays from Vela Junior have been presented before in a publication (Aharonian et al., 2007). The data presented in this work dispose of additional observation time. The morphology and the spectrum of this widely extended source is studied. This work presents for the first time a significant signal in VHE gamma rays from SN1006 from H.E.S.S. observations.
In the second part of this work a new type of camera is presented, designed to run in a Cherenkov telescope of the next generation of large Cherenkov arrays. Tests of a prototype camera with 128 pixels are shown.

In Chapter 2 the physics of supernovae and their remnants is discussed. Acceleration and production process of cosmic rays are presented. Chapter 3 describes the H.E.S.S. experiment, which detects VHE gamma rays with the Imaging Atmospheric Cherenkov Technique. The analysis technique of H.E.S.S. data is presented in Chapter 4. The analysis of the three supernova remnants is presented in the Chapters 5, 6 and 7. In Chapters 8 and 9 the new type of camera, the Smart Pixel Camera, and tests on a prototype are discussed.

Part I

Physical Background

Chapter 2

Supernovae and their Remnants

2.1 Introduction

Supernovae (SNe) are amongst the most impressive events in the Universe. They are believed to be the violent end of stellar evolution. Two different physical processes are thought to take place in SNe, either the collapse of the core of a massive star or the thermonuclear disruption of a white dwarf in a binary system. Both processes release a huge amount of matter into the interstellar medium (ISM) which was produced in both hydrostatic (during stellar evolution) and explosive (during the explosion) nucleosynthesis. These processes are believed to be the main source of most of the heavy elements in the Universe.
During the explosion a huge amount of energy is also released. For this reason SNe and their remnants, the SNRs, are discussed as potential sources of the cosmic rays up to energies of $\sim 10^{14}$ eV and beyond. To explain the flux and the spectrum of the observed cosmic rays the fraction of explosion energy which has to be transfered was estimated by Drury et al. (1989) to be between 10% and 30%. The values obtained by numerical simulations are indeed in this range (Dorfi (2000) and Berezhko (2001)).
Some of the SNe (of type Ia, see below) show a quite narrow distribution of total brightness. This property is used to measure the distance to these SNe by comparing the observed luminosity to the estimated total luminosity. The derived distances of several of these SNe have been used to constrain cosmological models by measuring the expansion of the Universe (see e.g. Riess et al. (1998), Perlmutter et al. (1999) and Riess et al. (2004)).
Beside the movement of the planets and solar eclipses, near-by SNe are the only variable events in the sky which can be observed by naked eye (i.e. with an apparent magnitude of > 6 mag). Events which can be associated with SN explosions by the detection of their SNRs, can be found in historical records. These are called *historical SNe.*

In 1054 the Chinese observed a SN whose remnant is now believed to be the Crab nebula. It could be seen for 23 days during the day and for seven more months at night by naked eye. These events shook at the belief that the universe, except for the movement of the planets, is invariant. The Chinese used the name *guest stars* for these events and believed that they were signs concerning the future of the current emperor. Interestingly no contemporary recordings exist from Europe about the guest star from 1054. One speculation is that it had been misinterpreted as a planet (Stephenson and Green, 2002).

Since then other guest stars or *novae*, as they were called later, have been observed. The word nova comes from the Latin word for "new" and was used for all new "appearing" stars. Especially the novae from 1572 (observed e.g. by Tycho Brahe) and 1604 (observed e.g. by Johannes Kepler), with the detailed recordings by Brahe and Kepler, give insight into the physical conditions at the time of the explosion. Events like these observed by Brahe and Kepler were thousands of times as bright as the bulk of the novae and much less frequent. Therefore, later on, Baade and Zwicky (1934) suggested to use the term supernovae for these events.

Unfortunately no SN was observed in our galaxy since Kepler's SN, apart from the controversial observation of Cas A by John Flamsteed in 1680. Based on observations of similar galaxies it is believed that $2-3$ SNe explode per century in the Milky Way (Cappellaro et al., 1999). The same number is estimated from the measurement of the amount of radioactive ^{26}Al in the Galaxy (Diehl et al., 2006) which is produced in massive stars and released into the Galaxy by core-collapse SNe and which decays with a half life of $\sim 7.2 \times 10^5$ yr. The fact that no SN have been observed in the last 400 years is most likely due to the absorption of the visible light by dust in the Galactic disk, which prevents the detection of light from distant objects.

Baade and Zwicky (1934) were the first who suggested that a SN represents the transition of an ordinary star into a neutron star. Hoyle and Fowler (1960) added as an alternative explanation the explosion of an electron-degenerated stellar core, triggered by thermonuclear burning.

The top part of Figure 2.1 shows the distribution of all historical SNe in a face-on view of the Galactic disk. The bottom part shows an edge-on view with all SNRs from the Green's catalogue (Green, 2004). As the historical SNe have been observed by naked eye they must have been near-by or off the Galactic plane. As more and more observations of the Milky Way at other wavelengths (radio, X-ray, gamma rays) are performed there should be detections of new Galactic SNe in the future. The detection of many neutrinos within a short time span by the large neutrino detectors (AMANDA, IceCube, ANTARES, Super-Kamiokande) could serve as a hint for a SN explosion (see below). However, the neutrino detection can hardly serve as a trigger for other telescopes because the current neutrino detectors obtain only poor direction reconstruction for SN neutrinos (within $5-20$ deg, Beacom and Vogel (1999)). Nevertheless, a supernova early warning system has been build making additionally use of triangulation with the timing information from different neutrino detectors (Scholberg, 2000), which can in some cases improve the direction reconstruction.

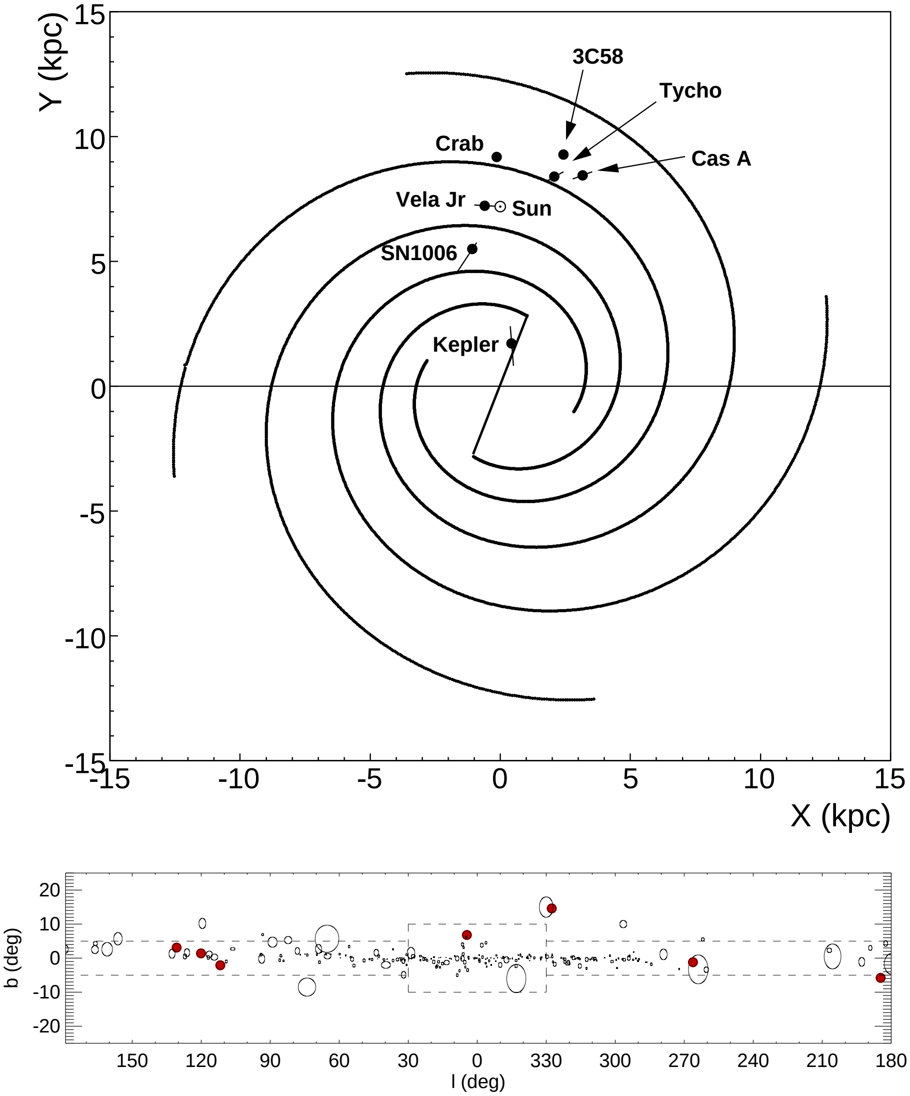

FIGURE 2.1: *Top:* A face-on view of the Galaxy with the historical SNe recorded during the last millennium. The circle denotes the position of the Sun. The black filled circles are the positions of the SNRs believed to be the remnants of the historical SNe. The overlaid lines show the distance uncertainties. The Galaxy-model is taken from Vallée (2002). *Bottom:* An edge-on view of the Galaxy (i.e. as seen from the Earth) with the SNRs from the Green's catalogue (Green, 2004). The historical events are drawn as red dots (not at scale). The three oldest historical SNe (AD185, AD386, AD393) are not taken into account as their association with known SNRs is still controversial.

2.2 Types of SN Explosions

The historical classification of SNe is based on observational parameters. SNe which exhibit hydrogen lines in their spectra are called type II, while those without hydrogen lines are called type I. With more observations the classification was refined. The type I was divided into SNe which show strong Si II lines (Ia) and those which do not (Ib, Ic). The type Ic differs from type Ib by the absence of helium lines. For type II also a subdivision exists based on the shape of the light curve (type II-P and II-L). The SNe of type II, Ib, Ic are only observed in spiral galaxies whereas the type Ia SNe are observed in both spiral and elliptical galaxies. Therefore the type II (Ib, Ic) SNe could be associated with ongoing star formation which is not present in elliptical galaxies.

An additional classification exists based on the assumed physical process leading to the explosion. One distinguishes core-collapse and thermonuclear SNe. The types II, Ib and Ic correspond to the collapse of the core of a massive star. This explains the occurrence of these types in spiral galaxies as in those massive stars are still present. Type Ia SNe are the thermonuclear disruption of an accreting white dwarf. The absence of H lines arises from the composition of the white dwarf. In Table 2.1 an overview of the different types is given.

	thermonuclear disruption	core-collapse
no H lines	Ia (Si)	Ib (no Si, He) Ic (no Si, no He)
H lines		II

TABLE 2.1: Different types and classifications of SNe

2.2.1 Type Ia

It is believed that a SN of type Ia is the explosion of an accreting white dwarf in a binary system exceeding the Chandrasekhar mass limit ($M_{\text{Chan}} = 1.49 M_{\odot}$). This limit was introduced by the Indian physicist Subrahmanyan Chandrasekhar as the upper limit for the mass of a stable white dwarf.

A white dwarf is the final configuration of the evolution of a star with an initial mass of $M \leq 8 M_{\odot}$. As the stellar fusion in the progenitor of the white dwarf stops before burning silicon it consists mainly of carbon and oxygen.

The matter in white dwarfs (or more precisely the electron gas) is degenerated. This means that nearly all quantum states in terms of the Pauli principle are occupied. The Fermi pressure of the electrons prevents the white dwarf from collapsing under the pressure of the gravitational force. The white dwarf is in an equilibrium state. Without any perturbation it cools down from its initial temperature $T_{\text{eff}} \sim 27000\,\text{K}$ over typical time scales of $8 \times 10^{9}\,\text{yr}$ (Koester and Chanmugam, 1990) and becomes a brown dwarf.

However, if the white dwarf has a companion from which it accretes matter the gravitational pressure in the white dwarf increases. When the white dwarf's mass reaches the Chandrasekhar limit, the Fermi pressure of the electrons is not sufficient to counteract the gravitational pressure. The white dwarf collapses and is disrupted by the thermonuclear fusion of carbon and oxygen. The exact mechanism of the explosion is still not clear. Two recent models of the explosion (pure turbulent deflagration and delayed detonation) are presented below together with the historically first attempt, a model assuming prompt detonation.

Because of the uniform conditions leading to the explosion the light curve and the total brightness are quite uniform. Therefore these events are used as *standard candles* for which the maximum brightness and the energy output scatters only little. The estimated total luminosity and the observed luminosity are used to measure the distance. This has been used to constrain cosmological parameters (see e.g. Riess et al. (1998), Perlmutter et al. (1999) and Riess et al. (2004)).

Unfortunately, the explosion energy and maximum brightness of type Ia SNe are not as uniform as thought in the past. Big efforts have been made to model the explosion. However, there are several different models with different explosion energies. In the following a short description of the main models is given. The discussion follows that of Hillebrandt and Niemeyer (2000).

Prompt Detonation. The scenario of a detonation wave passing through the entire star at the speed of sound (Arnett, 1969) fails to explain the observed amounts of intermediate mass elements (Filippenko, 1997). The white dwarfs carbon and oxygen are almost completely burned into iron-peak nuclei.

In addition the ignition of a detonation in the high density medium of a white dwarf is thought to be an unlikely event (Niemeyer and Woosley, 1997).

Pure Turbulent Deflagration. In the pure turbulent deflagration model a sub-sonic thermonuclear flame becomes highly convoluted by turbulence produced by various flame instabilities. The flame burns through the star until it either transitions into a detonation or is quenched by expansion.

A very good agreement with the observed spectra and light curves is reached in the frame of one-dimensional modeling, when the effective turbulent speed of the flame S_t accelerates up to roughly 30% of the speed of sound. A problem of the one-dimensional models is the overproduction of neutron-rich iron-group isotopes.

Multidimensional models failed to reach the effective turbulent flame speed of 30% of the speed of sound. To overcome the low S_t multi-point ignition and active turbulent combustion, i.e. the generation of additional turbulence by thermal expansion within the turbulent flame brush, were suggested.

Delayed Detonation. In this model the initial flame speed is roughly 1% of the speed of sound and transitions to a detonation at a density of $\rho \approx 10^7\,\mathrm{g\,cm^{-3}}$. Many one-dimensional simulations of delayed detonation have shown excellent fits to SN Ia spectra and light curves, as well as reasonable nucleosynthesis products. The transition density could serve as a convenient parameter to explain differences in the explosion strength.

Up to now there is no type Ia SN for which the progenitor has been observed. If the assumption about the progenitor is correct, this is not surprising as white dwarfs are faint compact objects.

2.2.2 Type II, Ib, Ic

The discussion in this section follows Woosley and Janka (2005) and Perkins (2003), chapter 7. A star with $M > 8M_{\odot}$ is believed to evolve in a different way at the end of its life. The burning does not stop at carbon and oxygen, but proceeds up to iron, which is the element with the highest binding energy per nucleon of all elements and therefore iron is the lightest element which does not release energy by nuclear fusion. After the burning phases the degeneracy pressure of the electron gas is not hight enough to stop the contraction of the core of the star.

Due to the high density ($> 10^{10}\,\mathrm{g\,cm^{-3}}$) in the core of the dying star, electrons are squeezed into the nuclei of the iron-group atoms. By inverse-beta decay

$$\mathrm{p} + \mathrm{e} \rightarrow \mathrm{n} + \nu_{\mathrm{e}}, \tag{2.1}$$

the neutron number increases and at the same time the electrons are taken away from the core. As the Fermi pressure of the electrons is the main counterpart to the gravitational pressure the loss of the electrons robs the core of both energy (inverse-beta) and support (degeneracy pressure).

Another process that accelerates the collapse of the core is photo-disintegration. As some of the gravitational energy is released the core is heated to temperatures well above $10^{10}\,\mathrm{K}$. Some of the thermal photons (with mean energies of 2.5 MeV) can melt down iron-group nuclei into alpha particles reversing the fusion processes

$$^{56}\mathrm{Fe} + \gamma \rightarrow 13\,^{4}\mathrm{He} + 4n. \tag{2.2}$$

The absorption of energy in this endothermic reaction (145 MeV for the complete photo-disintegration of one iron nucleus into alphas) speeds up the gravitational collapse. As a result the core is further heated and even the helium nuclei undergo photo-disintegration, being split into protons and neutrons.

As the core is robbed of all supporting pressures acting against gravitation the matter falls nearly freely with velocities of about a quarter of the speed of light. The collapse is stopped due to the repulsive component of the nuclear force when the core density exceeds the atomic nuclear density by a factor of 2-3. The outer parts of the core continue to crash down and a shock wave is produced. A few milliseconds later the shock wave stalls because of photo-disintegration and neutrino interactions. The dense, hot, neutron-rich core accretes mass at a rate of a few tenths of a solar mass per second. During that time the core emits a high luminosity of neutrinos. Over the next few seconds 10% of its rest mass is radiated as neutrinos. The neutrinos deposit a part of their energy in the medium surrounding the core and produce electrons and positrons in interactions with protons and neutrons. A large bubble of radiation and electron-positron pairs is inflated and an outgoing shock wave is produced which ejects the rest of the star and makes the explosion.

2.3 The Different Stages of SN Explosion

In the following the different phases of the SN explosion are discussed. For simplicity spherical symmetry and uniformity of the ejected material is assumed.

Additionally, the ambient medium is assumed to be uniform and stationary with low pressure and density (see e.g. Longair (1994), Stephenson and Green (2002)).

Free expansion. The ejecta, accelerated to velocities of about $(10-20)\times 10^3\,\mathrm{km\,s^{-1}}$ by the release of energy during the explosion, expand nearly freely into the ambient medium. The expansion is highly supersonic and therefore a shock front forms. The pressure of the shock heated ambient medium causes a weak reverse shock in the ejecta moving backwards to the core. As it is a nearly free expansion the radius r of the remnant evolves with time t as

$$r = v \cdot t, \tag{2.3}$$

where v is the average velocity of the ejected material. Because of the free expansion it is given by $v \approx \sqrt{2E_0/M_{\mathrm{ej}}}$.
Figure 2.2 shows the pressure, the density and the velocity as a function of the radius for the free-expansion phase (top three figures).

Sedov phase. When the swept-up mass exceeds the initial ejected mass, after approximately 200 years, the dynamics are described by the adiabatic blast-wave similarity solution of Taylor and Sedov (see Sedov (1959)). A shock wave propagates into the interstellar matter and a reverse shock propagates back into the ejecta. The overall dynamics are dominated by the amount of swept-up mass and the energy released in the explosion. Radiative losses are negligible, the energy is conserved. Because of this, this phase is also called *adiabatic phase.* The fraction of energy in form of kinetic energy is roughly constant (E_{kin} = const.). Therefore

$$\begin{aligned} \frac{1}{2}\rho_0 r^3 v^2 &\simeq E_{\mathrm{kin}} = \mathrm{const.} \\ \Rightarrow \sqrt{r^3 v^2} &= r^{3/2}\frac{dr}{dt} = \mathrm{const.} \end{aligned} \tag{2.4}$$

Separation of variables results in

$$r^{5/2} \propto t \quad \Rightarrow \quad r \propto t^{2/5} \tag{2.5}$$

The three bottom figures of Figure 2.2 shows the pressure, the density and the velocity as a function of the radius in the Sedov phase.
This phase lasts approximately 10^4 years.

Snow-plow phase. The temperature behind the shock drops below 10^6 K and cooling by line emission of heavy ions becomes important.

Dispersion phase. Finally, after approximately 10^5 years, the expansion velocity becomes sub-sonic, i.e. the shock has disappeared, and the supernova remnant loses its identity.

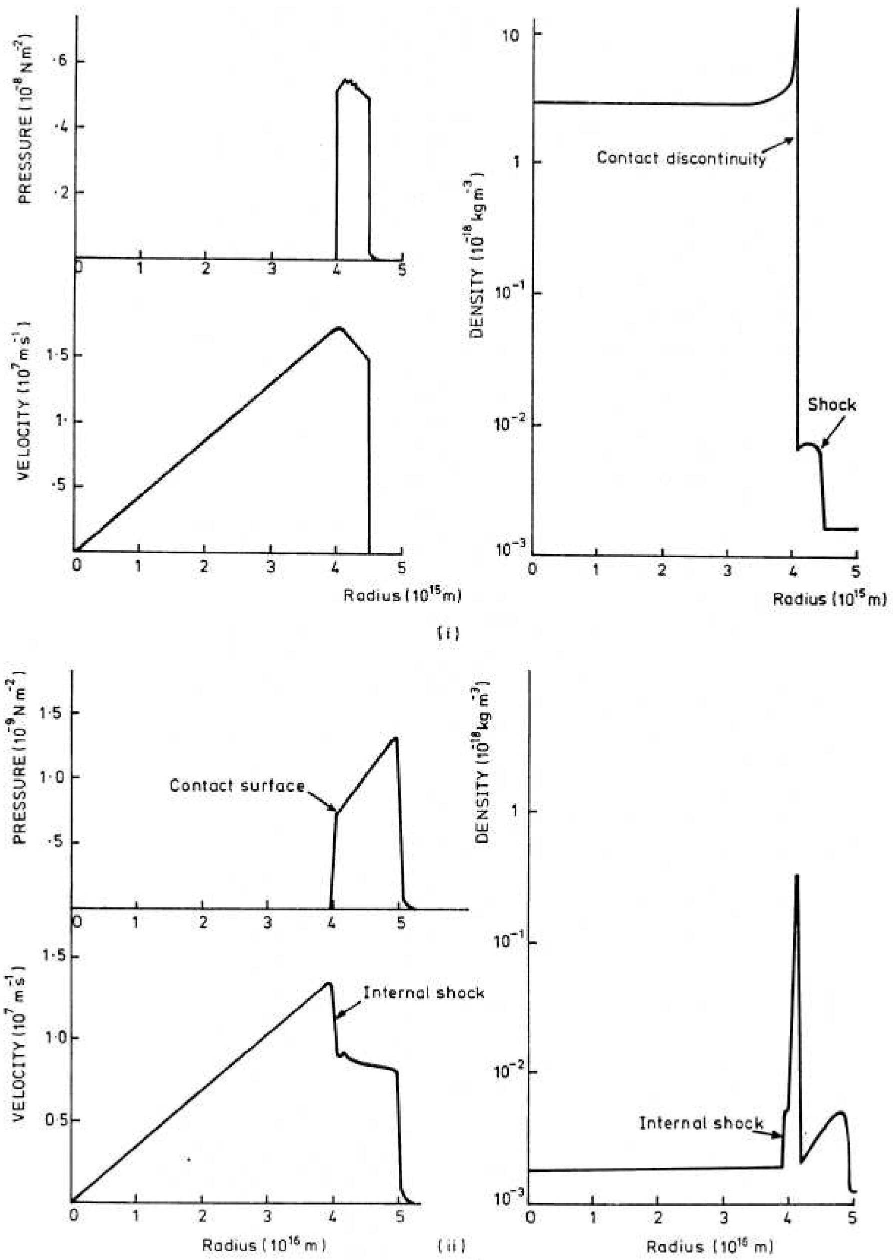

Figure 2.2: Pressure, density and velocity in the SNR evolution as a function of the radius. The top three figures (i) correspond to the free-expansion phase. A dense shell of material forms just behind the contact discontinuity. The three pictures in the bottom (ii) correspond to an SNR in the Sedov phase. Note the different scales of the radius. The reverse shock is heating up the material inside the expanding sphere. The figure is taken from Gull (1975).

2.4 Particle Acceleration in Shock Fronts

SNRs are the main candidates for the acceleration of cosmic rays to energies up to 10^{14} eV. This coincides with a slight softening of the cosmic ray spectrum, called the *knee* of the spectrum.

It was argued that SNe have to transfer 10% to 30% of their explosion energy into cosmic rays to account for the observed flux (Drury et al., 1989). Therefore the acceleration process needs to be very efficient. In the following a possible process is discussed which could indeed reach such an efficiency. The discussion follows that of Longair (1994).

In 1949 Fermi introduced a mechanism being capable to accelerate charged particles to high energies. In his picture, charged particles being reflected by randomly moving magnetic mirrors, with typical velocity V_{mirror}, gain energy statistically (see Figure 2.3). The calculation can easily be done in the center of mass frame. In the relativistic limit (where the particle velocity $v \to c$) the average energy gain per reflection is

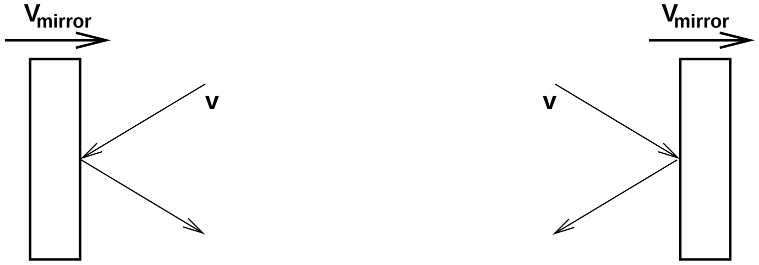

FIGURE 2.3: A particle being reflected by magnetic mirrors. The left side shows a head-on collision and the right side shown a following collision.

$$\left\langle \frac{\Delta E}{E} \right\rangle = \frac{8}{3} \left(\frac{V_{\mathrm{mirror}}}{c} \right)^2 . \tag{2.6}$$

As the average increase in energy is only *second order* in V_{mirror}/c this is called *second order Fermi acceleration.* Only a fraction of the collisions are head-on collisions, as can be seen in Figure 2.3. The particles gain energy only in head-on collisions.

If one assumes that the particle remains within the acceleration region for some characteristic time τ_{acc} one can show thatone can show that the energy distribution of the accelerated particles follows a power-law.

Assuming molecular clouds serving as magnetic mirrors, the process is not sufficiently fast to accelerate particles to the energies observed in cosmic rays. The time scales needed to accelerate particles up to these energies are much longer than the age of the Universe.

The situation changes for particle acceleration in strong shocks like those in SNRs. It will be shown in the following that in this case every collision is a head-on collision. Therefore this process is much more efficient as a particle accelerator.

To derive the energy gain per collision a strong shock moving through the ISM is considered. It is assumed that high-energy particles exist both in front of and behind the shock front. The velocity of the particles is assumed to be largely greater than the velocity of the shock. The thickness of the shock is normally very much less than the gyro-radius ($r = \gamma m_0 v \sin(\theta)/zeB$) of the particles and therefore the particles hardly notice the shock. After passing through the shock the particles are scattered. Because of turbulence behind the shock front and irregularities ahead of it their velocity distribution rapidly becomes isotropic in the rest frame of the gas on either side of the shock.

The following discussion is performed in the rest frame of the shock front. The mass passing through the shock front has to be conserved, hence

$$\rho_\mathrm{u} v_\mathrm{u} = \rho_\mathrm{d} v_\mathrm{d}, \tag{2.7}$$

where the index "d" stands for *downstream* and "u" for *upstream*. In the case of a very strong shock, for which the velocity of the shock front is much larger than the sound velocity in the undisturbed gas, the ratio of the density behind and in front of the shock is $\rho_\mathrm{d}/\rho_\mathrm{u} = (\gamma+1)/(\gamma-1)$, where γ is the ratio of specific heats of the gas. If one assumes that the gas is mono-atomic or fully ionized the ratio of specific heats is $\gamma = \frac{5}{3}$ and the density ratio becomes $\rho_\mathrm{d}/\rho_\mathrm{u} = 4$. The velocity of the gas in the downstream region is then given by $v_\mathrm{d} = \frac{1}{4} v_\mathrm{u} = \frac{1}{4} v_\mathrm{shock}$. This leads to the result that in the rest frame of the downstream region the particles from the upstream region are traveling towards the high-energy particles with the velocity $v = \frac{3}{4} v_\mathrm{shock}$ (see left panel of Figure 2.4). This is exactly the same in the rest frame of the upstream region (right panel of Figure 2.4). This means that particles crossing the shock suffer head-on collisions and are then scattered by turbulence or irregularities such that their velocity distribution becomes isotropic with respect to their new surrounding.

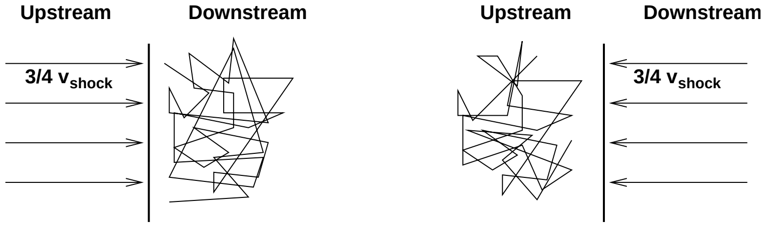

FIGURE 2.4: On the left side the flow of gas in the rest frame of the downstream region is shown. The figure on the right side shows the situation in the rest frame of the upstream region.

Using simple arguments, first introduced by Bell (1978), the energy gain for a complete cycle is given by

$$\left\langle \frac{\Delta E}{E} \right\rangle = \frac{4}{3} \frac{v_\mathrm{shock}}{c} \tag{2.8}$$

This process is called *first order Fermi acceleration*, as it is of first order in v_shock/c. It is much more efficient as the particle gains energy in each crossing of the shock front. In the calculation of the energy gain per cycle it has to be assumed that the particles that are injected into the shock region have velocities which are large compared to the velocity of the shock front. In this case the particles cross the shock front without being significantly deflected.

The shape of the resulting spectrum of accelerated particles is derived by simple arguments. It is assumed that the average energy after one collision is $E = \beta E_0$ and that the probability for the particle to stay in the acceleration region is p. After k collisions there are $N = N_0 p^k$ particles with an average energy of $E = E_0 \beta^k$. The number of collisions can be eliminated by combining both equations

$$\frac{\ln(N/N_0)}{\ln(E/E_0)} = \frac{\ln(p)}{\ln(\beta)}. \tag{2.9}$$

Therefore the number of particles with energies greater than E is $N(\geq E) = \text{const.} \cdot E^{\ln(p)/\ln(\beta)}$. The total differential of N is then

$$N(E)dE = \text{const.} \cdot E^{-1+\ln(p)/\ln(\beta)}. \tag{2.10}$$

This form is a power-law. In the case of a very strong shock it is

$$\frac{\ln(p)}{\ln(\beta)} = -1, \tag{2.11}$$

and hence

$$N(E)dE \propto E^{-2}. \tag{2.12}$$

2.5 Hadronic and Leptonic Scenario of Particle Acceleration

In the analysis of the SNRs Kepler (Chapter 5), Vela Junior (Chapter 6) and SN1006 (Chapter 7) very-high-energy gamma rays, which are produced in the vicinity of acceleration sides of cosmic rays, are studied. The gamma rays are produced by interactions of the charged cosmic rays with the interstellar matter or magnetic fields.

In the following the parameters and implications of two asymptotic cases, pure leptonic and pure hadronic acceleration, are discussed. In a real scenario both cases are expected to take place in SNRs. However, from the hypothesis of pure scenarios, useful statements can be derived.

2.5.1 Hadronic Scenario

Relativistic protons and nuclei colliding inelastically with the nuclei of the ambient matter produce π-mesons. The charged pions $\pi^{\pm}$ decay into muons and neutrinos. The neutral pion π^0 decays into two gamma rays with a lifetime of $10^{-17} s$ (Perkins, 2003).

From the threshold at 0.3 GeV, the cross-section for inelastic proton-proton collision σ_{pp} rises rapidly to about $(28-30)$ mb at energies about $E_{\mathrm{kin}} \approx 2$ GeV.

Above this energy σ_{pp} increases only logarithmically (Aharonian, 2004). Therefore the characteristic cooling time above 2 GeV of the protons via inelastic proton-proton interaction is almost independent of the proton energy. If one assumes an average cross-section at very high energies of 40 mb and takes into account that the proton loses a fraction of $f \approx 0.5$ of its energy in every interaction the characteristic cooling time becomes

$$\tau_{\mathrm{pp}} = \frac{1}{n_0 \sigma_{\mathrm{pp}} f c} \approx 1.7 \times 10^{15} \left(\frac{n}{1\,\mathrm{cm}^{-3}} \right)^{-1} \mathrm{s}, \tag{2.13}$$

where n is the density of the ambient medium. For simplicity it is assumed that all proton-proton interactions result in π-production ($\pi^{\pm}$ or π^0) and that 1/3 of the released energy is given to a π^0. The energy-loss time through π^0 production is then given by

$$\tau_{\mathrm{pp}\to\pi^0} = 3 \cdot \tau_{\mathrm{pp}\to(\pi^{\pm},\pi^0)} \approx 5.1 \times 10^{15} \left(\frac{n}{1\,\mathrm{cm}^{-3}} \right)^{-1} \mathrm{s}. \tag{2.14}$$

This value is used later in the analysis of gamma-ray emission from SNRs to estimate the total energy, W_{p}, in accelerated protons by using $W_{\mathrm{p}} = L_{\gamma} \cdot \tau_{\mathrm{pp}\to\pi^0}$, where L_{γ} is the luminosity in gamma rays.

2.5.2 Leptonic Scenario

There are three main processes in which ultra-relativistic electrons produce high-energy gamma rays. These are:

Bremsstrahlung. Free electrons being decelerated in the interaction of the ambient medium emit gamma rays. The important parameter in the description of this so-called bremsstrahlung is the radiation length X_0, which is the average distance over which an ultra-relativistic electron looses $1 - 1/e$ of its energy due to bremsstrahlung. In comparison with the inverse Compton scattering (see below) this process is only important for electron energies below $\sim$ 1 TeV and densities well above $1\,\mathrm{cm}^{-3}$. As in this work only gamma rays with energies above $\sim$ 100 GeV and emission regions with densities in the order of $1\,\mathrm{cm}^{-3}$ are studied bremsstrahlung is not taken into account in the discussion of the results.

Inverse Compton. High-energy electrons can up-scatter photons via the inverse Compton (IC) effect. This process is determined by the Klein-Nishina cross-section $\sigma_{\text{K-N}}$ (see e.g. Longair (1992)). When the photon energy $\hbar\omega$, in the center of momentum frame, is much lower than the rest mass of the electron

$$\frac{\hbar\omega}{mc^2} \ll 1 \tag{2.15}$$

the Klein-Nishina cross-section becomes the Thomson cross-section

$$\sigma_{\text{K-N}} \simeq \sigma_{\mathrm{T}} = \frac{8\pi}{3} r_{\mathrm{e}}^2, \tag{2.16}$$

which was published by Thomson in 1906 in a publication discussing the X-ray scattering of atomic electrons. In the ultra-relativistic limit $\sigma_{\text{K-N}}$ becomes

$$\sigma_{\text{K-N}} = \pi r_{\text{e}}^2 \frac{mc^2}{\hbar\omega} \left(\ln\left(\frac{2\hbar\omega}{mc^2} \right) + \frac{1}{2} \right), \tag{2.17}$$

so that the cross-section decreases roughly with $\frac{mc^2}{\hbar\omega}$ for very high energies.

The main target field for electrons with energies on the order of 10 TeV, which are believed to be present in cosmic particle accelerators, is the cosmic microwave background (CMB) (Aharonian et al., 1997). The interaction of electrons with photons in optical and X-ray wavelengths is highly suppressed by the Klein-Nishina cross-section. For a given electron energy E_e the corresponding energy in IC gamma rays in the Thomson limit is given by

$$E_{\text{IC}} \approx 5 \cdot \left(\frac{h\nu_0}{10^{-3}\,\text{eV}} \right) \left(\frac{E_{\text{e}}}{1\,\text{TeV}} \right)^2 \text{GeV}, \tag{2.18}$$

where $h\nu_0$ is the energy of the target photons. As the distribution of the CMB is a narrow Planckian distribution this energy can be taken to be equal to the mean energy of the target photons, which is $h\bar{\nu}_0 = 2.7\,kT \approx 6 \times 10^{-4}\,\text{eV}$.

The calculation of the average loss of an electron with velocity v by this process can be found in Longair (1992), section 4.3.3, and is given by

$$-\left(\frac{dE}{dt} \right) = \frac{4}{3} \sigma_{\text{T}} c U_{\text{rad}} \frac{v^2}{c^2} \gamma^2, \tag{2.19}$$

where σ_{T} is the Thomson cross-section and U_{rad} is the energy density of radiation in the rest frame of the electron.

Synchrotron radiation. Electrons which are deflected by magnetic fields emit synchrotron radiation. The characteristic energy of the emitted synchrotron photon depends on the magnetic field B and is given by

$$E_{\text{syn}} = 0.2 \left(\frac{B}{10\,\mu\text{G}} \right) \left(\frac{E_{\text{e}}}{1\,\text{TeV}} \right)^2 eV. \tag{2.20}$$

The average loss of an electron by synchrotron radiation is calculated in Longair (1994), section 18.1.1. It is

$$-\left(\frac{dE}{dt} \right) = \frac{4}{3} \sigma_{\text{T}} c U_{\text{mag}} \frac{v^2}{c^2} \gamma^2, \tag{2.21}$$

where $U_{\text{mag}} = B^2/2\mu_0$ is the energy density of the magnetic field. Note the remarkable similarity to Equation 2.19.

The energy of the IC gamma rays and that of the synchrotron photons emitted by the same electron can be connected using (2.18) and (2.20):

$$E_{\mathrm{syn}} \approx 0.07 \left(\frac{E_{\mathrm{IC}}}{1\,\mathrm{TeV}}\right)\left(\frac{B}{10\,\mu\mathrm{G}}\right)\ \mathrm{keV}. \tag{2.22}$$

The ratio of the relevant energy fluxes $f_i(E) = E^2 F(E)$, with the differential photon flux $F(E)$, is given by Aharonian et al. (1997)

$$\frac{f_\gamma(E_{\mathrm{IC}})}{f_x(E_{\mathrm{syn}})} \approx 0.1 \left(\frac{B}{10\,\mu\mathrm{G}}\right)^{-2} \cdot \xi. \tag{2.23}$$

The factor ξ takes into account possible differences in the size of the emission region for the different wavelengths.

2.6 Determination of the Distance

The distance determination of Galactic SNRs is difficult. The measurement of spectral lines gives mainly the movement of the emitting material which has, in the case of SNR, large relative velocities. Therefore this cannot be used for the measurement of the distance. One possibility is to check for absorption features due to material (mainly molecular clouds) in the line of sight of the SNR. In the case of absorption the SNR has to be behind the molecular cloud. In the case of strong variations in the column density without variations in the emission from the SNR the remnant has to be in front of the molecular cloud.

The distance to molecular clouds is determined by the measurement of HI line (at a wavelength near 21 cm) and the use of a rotation model of the Galaxy. Because of the differential rotation of the Galaxy different parts of the Galactic disk show different velocities compared to the movement of the sun.

Another technique has long been used for the distance estimation, the surface-brightness/diameter relation. From the observed surface brightness a physical diameter is derived and compared to the angular diameter. However, Green (1984) showed that the remnants with reliable distances have a wide spread of their intrinsic properties and therefore the usefulness of this technique is limited.

Chapter 3

H.E.S.S.

In this chapter the Imaging Atmospheric Cherenkov Technique is described used to detect VHE gamma rays from SNRs and from other objects like active galactic nuclei, pulsar wind nebula, X-ray binaries and the Galactic center. First an introduction of the development of air showers in the atmosphere is given. Then the Imaging Atmospheric Cherenkov Technique is discussed and finally the H.E.S.S. array is described.

3.1 Air Shower

VHE cosmic-ray particles and gamma rays induce air showers in interaction with nuclei in the atmosphere. In these showers particles are produced either through strong or electromagnetic interactions. At a height of about 10 km above see level the number of particles reaches its maximum. At this point the energy of most of the shower particles is not big enough to produce further particles. The dominating energy loss comes from ionization instead of from the production of particles and bremsstrahlung. Finally the shower dies out.
As there are charged particles in the shower propagating faster than the local speed of light Cherenkov radiation is produced. Two different shower types are distinguished, electromagnetic and hadronic showers.

3.1.1 Electromagnetic Shower

A pure electromagnetic shower is induced either by a gamma ray, an electron or a positron. The processes in the shower development are mainly bremsstrahlung and electromagnetic pair production. The secondary electrons and positrons emit photons via bremsstrahlung. Secondary photons produce electrons and positrons via pair production. This results in a cascade of secondary particle production. Bremsstrahlung and pair production determine the longitudinal development of the shower. The energy of the particles in the shower decrease following

$$-\left(\frac{dE}{dx}\right) = \frac{E_0}{X_0}, \tag{3.1}$$

where X_0 is the characteristic length of energy loss of the particles. The production of new particles stops roughly at the point where the energy of the electrons and the positrons drops below $E_c \simeq 80\,\mathrm{MeV}$. At this energy the energy loss due to ionization of atoms in the atmosphere becomes comparable with that due to bremsstrahlung. This point is called *shower maximum* as at this point the number of particles in the shower is maximal. The number of particles $N_{\max}$ at the shower maximum is roughly given by $N_{\max} \approx E_{\mathrm{incident}}/E_c$, where E_{incident} is the energy of the primary particle that initiated the shower.
The lateral development of the shower is determined by multiple Coulomb scattering. The mean scattering angle is rather small. Therefore the lateral spread of the shower is small. A simulation of an electromagnetic shower is shown in the left panel of Figure 3.1. .

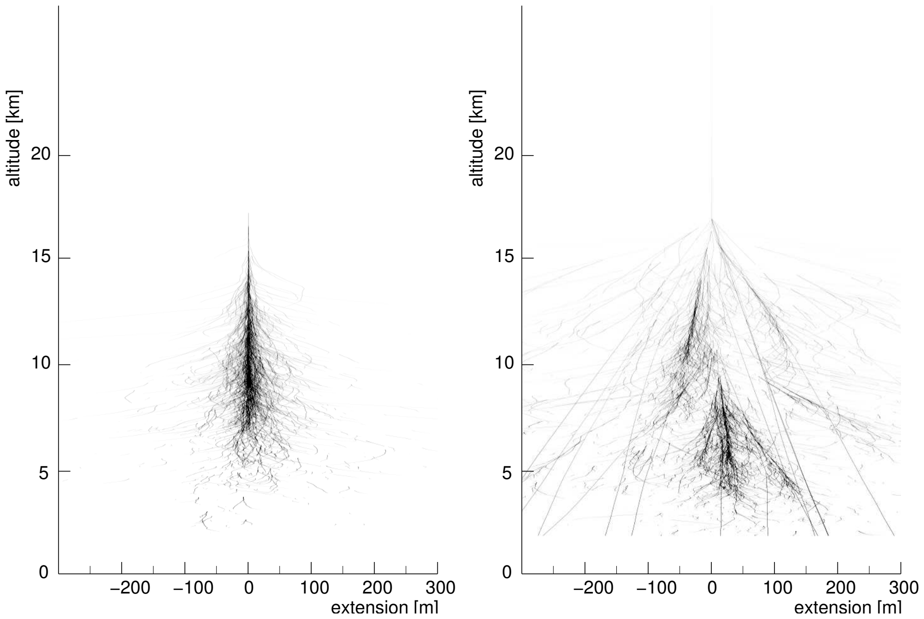

FIGURE 3.1: Shower profiles from simulations. *Left:* Gamma-ray shower induced by a gamma ray of 300 GeV. *Right:* Proton shower induced by a proton of 1 TeV (by courtesy of K. Bernlöhr)

3.1.2 Hadronic Shower

Air showers induced by hadrons are more complex as additionally strong interactions take place. By inelastic scattering of the cosmic-ray hadron off atmospheric nuclei, mesons like pions and kaons as well as nuclei and hyperons are produced. From the decay of mesons electromagnetic sub-showers develop within the hadronic shower. On average 30% of the energy of the incident particle is transfered to electromagnetic sub-showers. The rest of the energy is taken away from the shower by neutrinos and muons.
In the right panel of Figure 3.1 the profile of a simulated shower induced by a proton is shown.

3.1.3 Cherenkov radiation

The particles in the shower are faster than the speed of light in the atmosphere and therefore, in the case of charged particles, emit Cherenkov light. The angle θ between the emitted photons and the propagation path of the charged particle follow

$$\cos(\theta) = \frac{c}{v \cdot n}, \tag{3.2}$$

where c is the speed of light in vacuum, v is the particle velocity and n is the local refractive index. The distribution of the shower particles together with their different Cherenkov emission angles over the development of the shower through the atmosphere results in an roughly homogeneously illuminated circle on the ground with a diameter of about 250 m.

3.2 Imaging Atmospheric Cherenkov Technique

In the Imaging Atmospheric Cherenkov Technique the Cherenkov radiation of the shower particle is collected by a large mirror and imaged onto a sensitive pixelized camera. The resulting image is a two-dimensional projection of the shower into the camera plane. This technique was for the first time used by the Whipple collaboration to study VHE gamma rays (Weekes et al., 1989).

The shower development in the atmosphere is very fast, the Cherenkov light from the whole shower reaches the mirror within few nanoseconds. The image of the shower in the camera is clumpy as it reflects the distribution of charged particles. The cameras are triggered by clusters of pixels with signals above a set threshold and integrate the arriving signal over typically $10 - 20$ ns.

From the shape of the image in the camera shower parameters like size, orientation, width and length are reconstructed. With more than one telescope in the light cone of the Cherenkov light a three dimensional reconstruction of the shower location in space and hence the determination of the original direction of the primary particle can be derived. This stereoscopic technique was pioneered by the HEGRA collaboration (Daum et al., 1997).

3.3 The H.E.S.S. Array

H.E.S.S. is an array of imaging atmospheric Cherenkov telescopes located in the Khomas highland of Namibia. It was designed to investigate the gamma rays in the range from 100 GeV to 100 TeV. Figure 3.2 shows a picture of the H.E.S.S. telescope array. The name H.E.S.S. stands for High Energy Stereoscopic System, and it should also remind of Victor Hess, who discovered the cosmic rays in 1912 and received the Noble Prize in 1936 for this discovery. The array consists of four telescopes with a mirror dish each of 13 meters diameter. They are arranged on the corners of a square with side length of 120 m. The spacing has been optimized for maximum sensitivity at an energy of 100 GeV.

To date, the H.E.S.S. array is the most sensitive detector for VHE gamma rays in its energy range. It can detect a flux of 2.0×10^{-13}gamma rays $\mathrm{cm}^{-2}\,\mathrm{s}^{-1}$

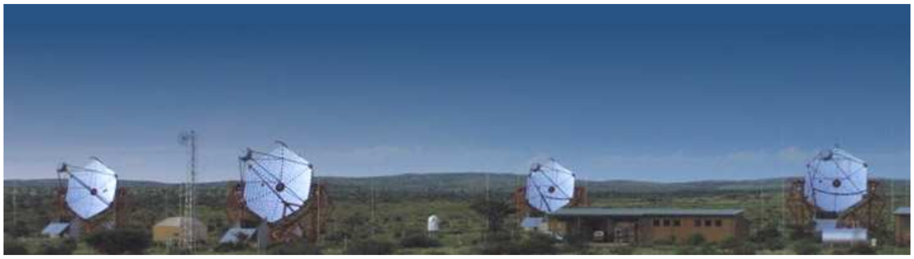

FIGURE 3.2: The four telescopes of the H.E.S.S. telescope array.

within 25 h at a significance of 5 standard deviations. The angular resolution for the reconstruction of the original direction of an individual gamma ray is better than 0.1 deg. The energy resolution is $\sim 15\%$.
The data taking started in Summer 2002 when the first telescope had its first light. The complete system was operational in December 2003. In the next phase of the H.E.S.S. experiment an even larger telescope will be build in the center of the four existing telescopes. The mirror dish will have a diameter of 28 meters and an area of 600 square meters. This will improve the sensitivity in the current energy range and lower the energy threshold to some 10 GeV.
In the following the main parts of the current telescopes are presented.

3.3.1 Mount and Dish

The telescopes are build in an altitude-azimuth mount. The steel structure of each telescope weights 60 t and was designed for high rigidity. Figure 3.3 shows the side view of a H.E.S.S. telescope. The dish hosts 382 mirrors of 60 cm diameter each, which can be aligned separately with high precision. After mirror alignment the point spread function is contained within one pixel over most of the field of view. The mirror tiles consist of ground glass with an aluminized front surface and are arranged in Davis-Cotton design. The mirror dish of each telescope has a diameter of ~ 13 meters and an area of $\sim 107\,\mathrm{m}^2$. The focal length of the mirror is $\sim 15\,\mathrm{m}$. The steering of the whole telescope is done using a computer-controlled system. It takes between one and three minutes to slew from parking position to an object in the sky.

3.3.2 Camera

The cameras of the H.E.S.S. telescopes are equipped with 960 photon detector elements, the pixels, in a hexagonal arrangement. The detectors are 8-stage photomultiplier tubes (PMTs) with borosilicate windows. They are operated at a gain of 2×10^5. The pixels are equipped with Winston cones to reduce the loss of light between the pixels. Each 16 pixels with the associated electronics are combined in a *drawer*. A drawer hosts two acquisition cards, each reading the data from 8 PMTs. Figure 3.4 shows a drawer of the H.E.S.S. cameras. For each pixel three channels are readout, one trigger channel and two acquisition channels with two different gains. The high gain channel covers the range up

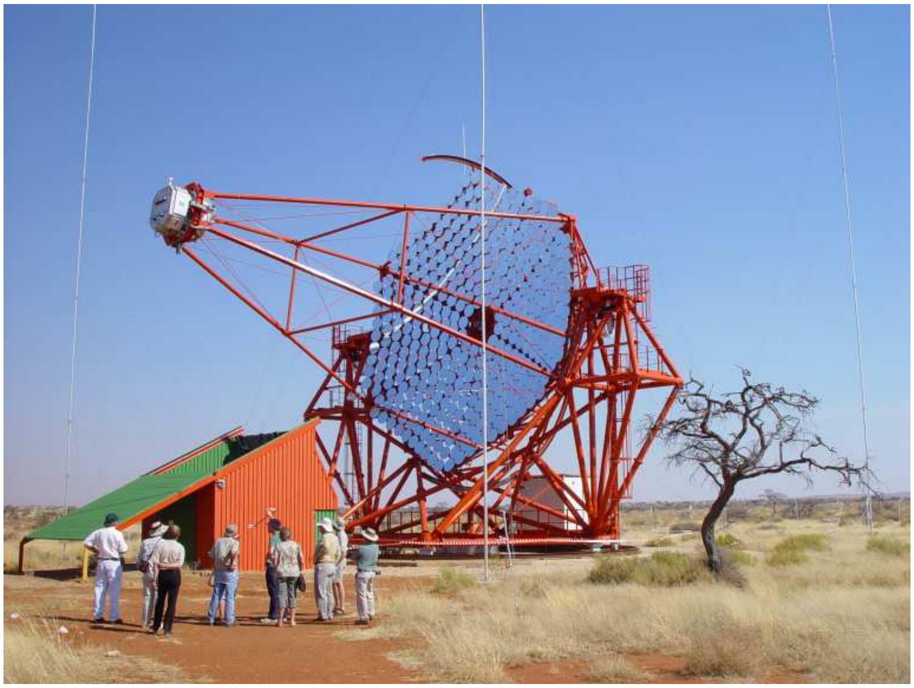

FIGURE 3.3: Side view of a H.E.S.S. telescope. The picture was taken on an open day in September 2004.

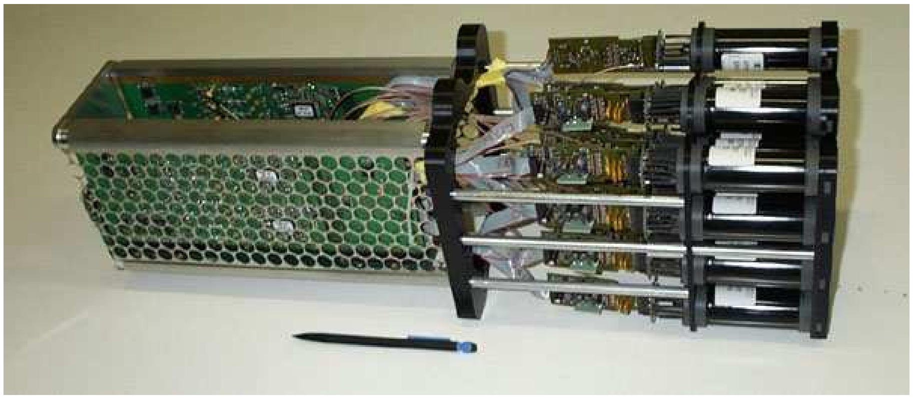

FIGURE 3.4: Drawer of the H.E.S.S. cameras

to 200 photo electrons (p.e.) and the low gain channel covers the range from 15 p.e. to 1600 p.e. The signal measured in the acquisition channels is captured in a 1 GHz Analog Ring Sampler, which samples the signal every nanosecond and stores the recorded signals in a 128 ns buffer. This is needed as the information about the trigger needs $70 - 80$ ns to be computed and distributed to all drawers of the camera.

For the trigger generation overlapping *sectors* of 8×8 pixels are implemented. The camera is triggered when 3 to 5 pixels of a sector detect coincident signals above a set threshold, typically 5 p.e. The time window for coincidences is only about 1.5 ns. This is important for rejecting the triggering on uncorrelated PMT signals due to photons from the night sky background (NSB). This short coincidence window is only possible due to sorting of the PMTs by high voltage within the camera. The camera is connected to the central trigger system to allow for multi-telescope triggers (see next section).

For monitoring purposes the drawers provide information about the PMT currents, trigger rates, supply voltages and the temperature.

An air cooling system is used to remove about 5 kW of heat which is dissipated in the camera during operation.

3.3.3 Central Trigger

To make use of stereoscopy, the H.E.S.S. telescopes are only read out in the case that more than one telescope has sent a trigger signal to the central trigger system.

The trigger signals of the telescopes are recorded on a central trigger system. It is designed to serve up to 8 telescopes arranged into arbitrary sub-arrays. The communication between the central trigger system and the telescopes is done using an optical fiber system. In the case of a telescope coincidence, the central trigger system distributes a trigger signal to all telescopes and the cameras which contributed to the system trigger are read out.

Part II

Analysis of HESS data

Chapter 4

Analysis Technique

In this chapter the standard analysis technique of the H.E.S.S. experiment is presented. The discussion follows Aharonian et al. (2006b).

In Section 4.1 the selection of good data is described. An overview of the calibration of the H.E.S.S. cameras is given in Section 4.2. This is done im more detail to compare it with the calibration of the different camera discussed in Chapters 8 and 9. Section 4.3 describes the image cleaning procedure. Section 4.4 gives an overview of the standard analysis used to analyse H.E.S.S. data.

4.1 Data Selection

All data analysed from H.E.S.S. are selected based on standard quality criteria. Information from hardware and weather monitoring is used to reject runs if the conditions under which the data were taken were not stable. The main quality criteria are the number of active pixels (pixels can be switched off because of malfunctions or bright stars in the field of view), variations in the trigger rate and the number of participating telescopes.

Runs for which the *root mean square* (rms) variation in the trigger rate is above 10% are rejected. Telescopes with more than 10% of the pixels swiched off are not included into the analysis.

4.2 Calibration

The data recorded by the pixels of the H.E.S.S. cameras are provided as ADC counts. To generate physical statements (like gamma-ray excess and energy) the cameras must be calibrated. A detailed description of the calibration can be found in Aharonian et al. (2004a).

The main parameters which have to be calibrated are the flat-field coefficients ensuring a homogeneous efficiency in the camera, the timing of the signal integration, the mean ADC level without any Cherenkov signal (the *pedestal*) and the conversion factors needed to convert the ADC values to photo electrons (p.e.).

The signals measured by the photomultiplier tubes (PMTs) are stored until a trigger decision is made. In the H.E.S.S. cameras this is done using Analogue

Ring Samplers (ARSs) which operate at a rate of 1 GHz and have a storage of 128 capacitor cells. In each cell the signal which arrives at the PMT during one single nanosecond is stored. Every group of 16 pixels is equipped with eight ARSs storing the signals with two different gains of the 16 pixels. Following the arrival of a trigger at the drawers the sampling is stopped and a region of cells $[128 - N_{\mathrm{d}}, 128 - (N_{\mathrm{d}} + N_{\mathrm{L}})]$ in the ARS is read out. This region has a width of N_{L} nanoseconds (for normal observations $N_{\mathrm{L}} = 16\,\mathrm{ns}$) and corresponds to PMT signals which were stored in the ARS $N_{\mathrm{d}}\,\mathrm{ns}$ before the sampling was stopped. Therefore N_{d} is the delay between the time the PMT signal arrives at the pixel electronics and the time the trigger signal arrives at the ARS. It is calibrated using the *sample mode* of the ARS in which the charge of all N_{L} cells of the readout window are digitized and stored. This way the pulse shape can be studied and the timing can be adjusted.

The pedestal of the amplitude measurement is measured using pixels assumed to contain no Cherenkov light. In practice, these are all pixels with amplitudes below the pixel threshold (around $1.5 - 3\,\mathrm{p.e.}$) with all neighbors also having amplitudes below the threshold.

The conversion factor between ADC channels and signal charge is calibrated with the use of single photo electron spectra. These are charge distributions for which in average one photo electron is recorded by every pixel. Therefore the camera is illuminated with a pulsed LED. The same signal which triggers the LED is used to start the camera readout. At least two peaks have to be identified in the distribution: the pedestal peak, corresponding to readouts without any signal in the PMT of the pixel and the single photo electron peak, corresponding to readouts with exactly one photo electron emitted at the cathod of the PMT. To derive the number of ADC channels between those peaks a function describing the expected signal distribution is fitted to the data. An example distribution is shown in Figure 4.1.

4.3 Image Cleaning

To reduce the influence of photons which do not originate from Cherenkov showers (e.g. NSB and starlight), an image cleaning procedure is applied to the camera image of every triggered event. In the standard procedure all pixels containing a signal of more than 10 p.e. with a neighbor containing a signal of more than 5 p.e. are kept. Additionally, all pixels containing more than 5 p.e. with a neighbor with more than 10 p.e. are also kept. The remaining pixels are excluded from the analysis. This procedure increases the accuracy of the determination of the shower image moments (see the following section).

4.4 The Standard Analysis

4.4.1 Hillas Parameters

In the standard H.E.S.S. analysis a Hillas-type parameterization (Hillas, 1985) of the shower image is applied. As the camera is situated in the focal plane of

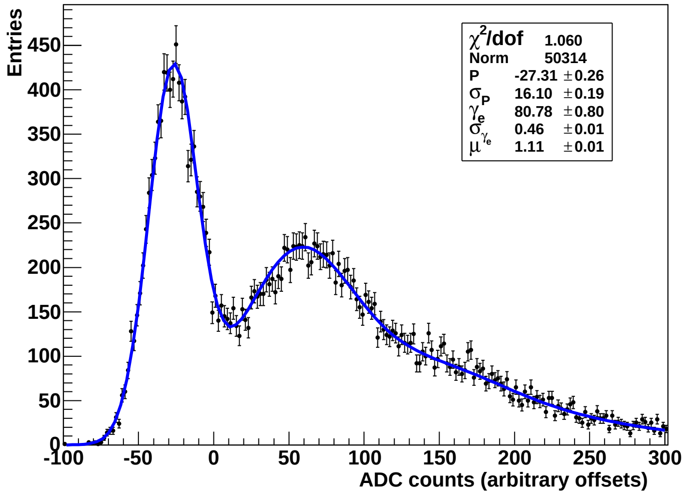

FIGURE 4.1: Example of a single photo electron spectrum. The conversion factor between ADC channels and signal charge in this pixel is 80.78

the mirror dish, the combination of pixel amplitudes and the positions of the pixels provide the image of the shower. The longitudinal spread of the shower in the atmosphere is much bigger than the lateral spread and therefore the image has a roughly elliptical shape. To characterize a shower image, the first and second moments of its intensity distribution are calculated. The first moments are the mathematical equivalent of the center of gravity (COG) of the image. The matrix of the second moments is the representation of an ellipse around the COG. Diagonalisation of the matrix gives the lengths of the main axes and the orientation of the ellipse. The determination of the first and second moments of the image distribution reveals six useful parameters, the *Hillas parameters*: position of the COG, lengths of the main axes (*length* and *width*), orientation of the ellipse and image size (which is the total number of p.e. in the image) (see Figure 4.2).
The Hillas parameters contain crucial information about the Cherenkov shower. The length and width of the ellipse are correlated with the longitudinal and lateral spread of the shower. The orientation of the ellipse and the COG are correlated with the orientation with respect to the pointing direction and the impact point of the shower axis on the ground, respectively. The distance from the telescope to the impact point of the shower axis in the plane of the dish is the *impact parameter* The size of the image is correlated with the number of Cherenkov light-emitting particles in the shower and therefore enables the reconstruction of the energy of the primary photon.

4.4.2 Direction Reconstruction

The image in the camera is the projection of the shower into the camera plane and therefore the major axis of the ellipse is the optical image of the shower axis.

Two images of the same shower from different viewing angles can be used to reconstruct the arrival direction of the primary photon by intersecting their major axes. Figure 4.2 illustrates images of the same shower, as they would appear in the combination of two telescopes images. In the case of more than two images, the shower direction is over-constrained. In Hofmann et al. (1999) several different algorithms for the direction reconstruction are discussed. The standard method used for H.E.S.S. data is a modified version of Algorithm 1. The intersection points of every pair of shower images are combined using a suitable averaging method to obtain the optimum estimate of the shower direction. Therefore, in the direction reconstruction, each intersection point is weighted with the sine of the angle between the image axes, the size of both images and the ratio of width to length from each image.

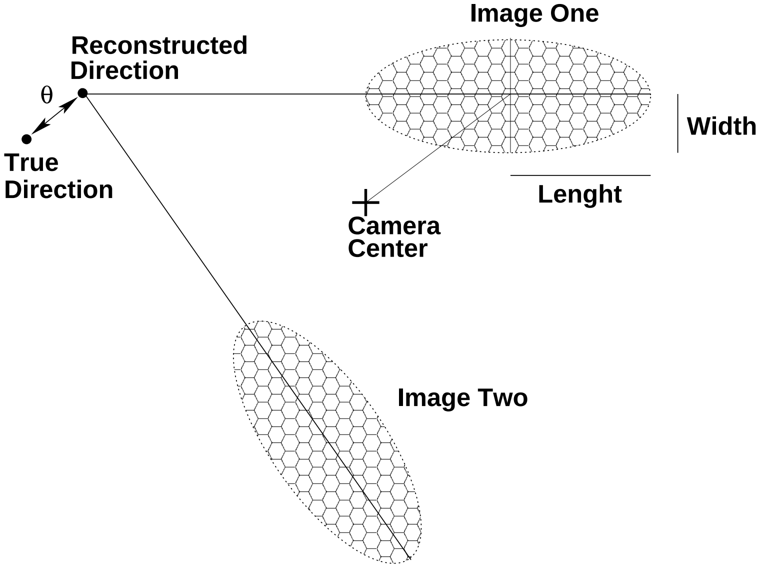

FIGURE 4.2: Scheme for the determination of the Hillas parameters. Shower images of two telescopes are shown combined in a common plane. This picture was inspired by Aharonian et al. (2006b)

For simulations the angular difference between the reconstructed position and the simulated (*true*) position is called θ. In the case of an observation this is the difference between the reconstructed position and the assumed source position.

4.4.3 Image Cuts

Events with to few p.e. (e.g. $< 80\,\text{p.e.}$) are rejected, since the errors of the reconstruction in these cases become very large. Furthermore, events for which the light distribution is to far from the camera center are also rejected as the accepance drops towards the edge of the camera. These pre-selection cuts are called *size cut* and *distance cut*.

Gamma-induced air showers differ from the hadron-induced ones by the spatial distribution of the shower particles (see Chapter 3). The latter are much wider and clumpier. This fact can be used to introduce a cut on image parameters to suppress the numerically dominat hadron-induced images. Based on Monte Carlo simulations, the mean length $\langle l \rangle$ and width $\langle w \rangle$ of a gamma-induced image are calculated as a function of the image size and the impact parameter for a range of zenith angles Z. The measured value (l and w) for a particular event can be compared to the expectations ($\langle l \rangle$ and $\langle w \rangle$) following

$$l_{\text{scaled}} = \frac{l - \langle l \rangle}{\sigma_l} \quad \text{and} \quad w_{\text{scaled}} = \frac{w - \langle w \rangle}{\sigma_w}$$

where σ_i is the standard deviation of the distribution of the value i. A *mean reduced scaled length* (MRSL) and *width* (MRSW) is calculated averaging over all the contributing camera images. The distributions of these parameters differ between gamma- and hadron-induces showers and can therefore be used to suppress the latter. Figure 4.3 shows the distribution of the MRSW for Monte Carlo gamma rays simulations in comparison with Monte Carlo protons simulations and real OFF data at a zenith angle of 50 deg. It can be seen that there is good separation between the OFF data and the Monte Carlo gamma rays. This is used to choose a region for the MRSW (and the MRSL) which covers most of the gamma-ray induced events and rejects as many hadron induced events as possible.

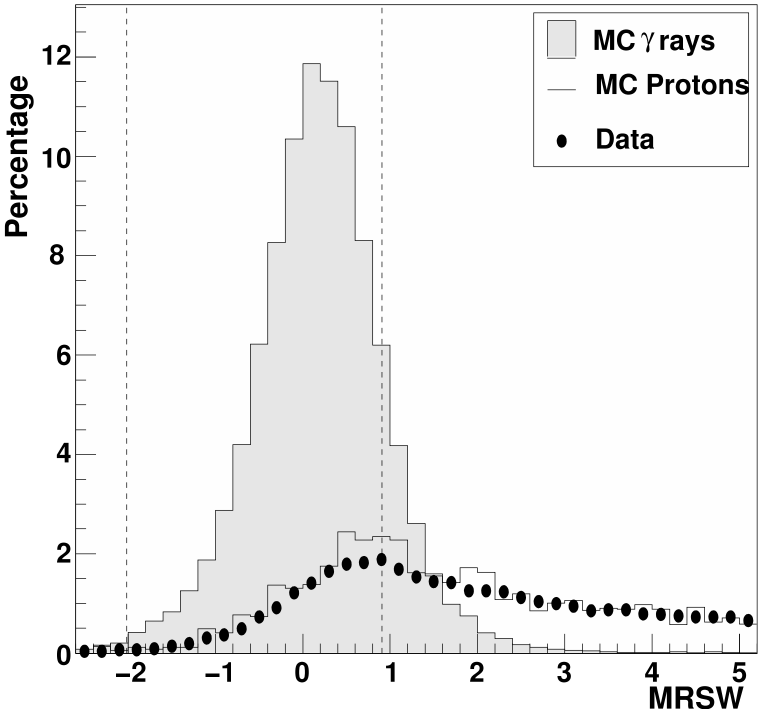

FIGURE 4.3: Distribution of MRSW from Monto Carlo gamma ray simulations in comparison with Monte Carlo proton simulations and real OFF data. The figure is taken from Aharonian et al. (2006b).

To derive the mean value and the standard deviation for length and width, Monte Carlo simulations have been performed for 13 zenith angles between 0 deg and 70 deg. The resulting mean length and width and their standard deviation are filled into 2D lookup tables. As only 13 lookup tables for different zenith angles are available the values for a given zenith angle are linearly interpolated in cosine of zenith angle between the nearest simulated values.

The cuts on the mean reduced scaled parameters, the size of the image and θ^2 (square of the distance between reconstructed and assumed true source direction) are optimized simultaneously using simulated gamma-ray events and real background data. The optimization aims for a maximum detection significance (as defined by Li and Ma (1983)). The optimization depends on the simulated gamma-ray spectrum. Two sets of cuts are primarily used in the standard H.E.S.S. analysis: *standard cuts* (optimized for a source with 10% of the flux from the Crab nebula and a similar spectral index (i.e. $\Gamma = 2.39$)) and *hard cuts* (optimized for a source with 1% of the flux from the Crab nebula and a spectrum with a spectral index of $\Gamma = 2.0$).

The dependence of the angular resolution on the cuts and the observations conditions (zenith angle and pointing offset) was explored in detail by Berge (2006). For a zenith angle of 20 deg and an pointing offset of 1 deg the 68% containment radii for hard and std cuts are 0.07 deg and 0.11 deg, respectively.

4.4.4 Muon Correction

The response of the optical system that contains the mirrors, Winston cones and PMTs, changes over time. The overall effect is a decrease in the thoughput of the system. For an accurate reconstruction of event energy it is necessary to measure this decrease and correct for it. This is done by analyzing images of the Cherenkov light emitted by single muons passing close to the telescope. The light yield of these events can be predicted based on geometrical arguments. The measured number of p.e. is then compared to the predicted light yield and a correction factor is calculated. By multiplying the reconstructed energy with the derived factor the energy is corrected for changes in the optical response. A detailed description of the method can be found in Bolz (2004).

4.4.5 Background Estimation

The discussion in this section follows that of Berge et al. (2007). Some of the hadron-induced showers are not rejected by cutting on the image parameters as their images are similar to images induced by VHE gamma rays. For the estimation of the gamma-ray flux from a particular position in the sky it is necessary to estimate the number of background events expected at that position. The number of source events and number of background events can then be used to calculate the significance with the formula of Li and Ma (1983).

For nearly all methods of the background estimation used in the analysis of H.E.S.S. data the reconstructed events are filled into a *sky map*, which is the two dimensional distribution of the reconstructed directions of all gamma-ray-like events. The number of ON events for a particular position in the sky are

taken from a circle around that position with the radius θ_{cut}.
Most of the methods for the background estimation use informations from sky maps. The methods used in this work are described in the following.

System Acceptance for Cosmic-Rays

The system acceptance at a certain position in the field of view is defined as the probability of accepting, after triggering and image cuts, a background event which is reconstructed at that position with a certain energy. For most background estimates some knowledge of the acceptance is needed. In general, it depends on

- the position in the field of view
- the zenith and the azimuth angle of the observation, due to the influence of the Earth's magnetic field and the atmosphere on the shower development
- the reconstructed energy of the primary particle
- the time of the observation, due to changes in the optical efficiency of the system

In most cases it is a reasonable assumption that the acceptance is radially symmetric. The acceptance is obtained either on a run-by-run basis during the analysis of the data or from observations without significant gamma-ray emission in the field of view.

Reflected Background Method

This method makes use of the approximation that the acceptance of the system is a function of the distance to the pointing position and the zenith angle. It is only usable for runs taken in *wobble mode*, in which the source is observed with an offset with respect to the pointing position. The wobble offset has to be large enough for the pointing direction to be outside of the defined source region. In this case (and if additionally the FoV does not contain a large number of other possible gamma-ray sources), the background can be estimated from regions in the FoV with the same size and offset as the source region. In the left panel of Figure 4.4 an example for the reflected background is illustrated. The number of regions depends on the offset and the size of the source region and the presence of other gamma-ray sources in the FoV, because the OFF regions have to be separated from each other and free of known gamma-ray sources. Additionally, a gap between ON and OFF regions is needed to avoid contamination of the OFF regions by misreconstruced gamma-rays.
The advantage of this method is that the normalization between the ON and OFF counts is given by the ratio of solid angles, only. All other possible dependencies like differences in exposure and acceptance are eliminated as the OFF events are taken at the same time with the same offset to the pointing position. If the acceptance of the camera also depends on the position in the FoV (not only on the distance to the pointing position) the reflected background estimation does not give the exact background level for the ON region. To reduce

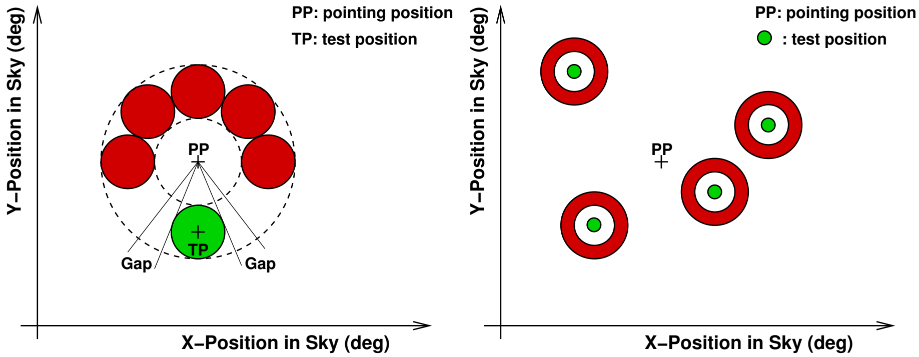
PP: pointing position
TP: test position
PP
TP
Gap
Gap
Y–Position in Sky (deg)
X–Position in Sky (deg)
PP: pointing position
● : test position
PP
Y–Position in Sky (deg)
X–Position in Sky (deg)

FIGURE 4.4: *Left:* Reflected background with five background regions *Right:* Ring background. For clarity only four positions in the FoV with their background estimation are illustrated.

systematic effects because of non-radial acceptance variations, the wobble position is altered around the target position. Figure 4.5 shows the test region and the background regions for four pointings around Kepler's SNR. With this method the influence of possible gradients in the acceptance is compensated. The reflected background method is best suitable for flux and spectrum measurements, as the normalization factor does not depend on the energy.

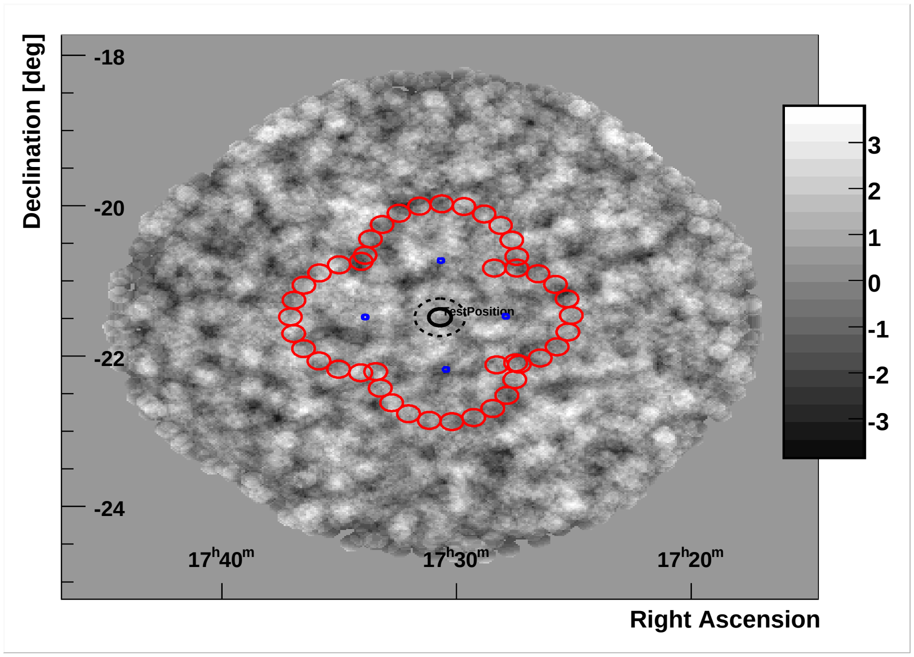

FIGURE 4.5: Example of four wobble positions around Kepler's SNR. The test region is the black circle in the middle of the picture. The red circles are the background regions and the blue dots denote the pointing positions in the four pointings.

Ring Background Method

In this method the background for a given position in the FoV is taken from a ring surrounding this position. In the right panel of Figure 4.4, the ring background estimation for four example regions is displayed. This is done for every position in the FoV. Therefore this method provides the background for the whole FoV. As a consequence the ring background allows the determination of excess and significance sky maps.
The inner and outer ring radii are often chosen such that the ratio of the solid angles of the ring and the ON region are close to 7. This is a compromise between area within the ring and spacing between ring and ON region. Here again the spacing must be large enough to suppress the contamination of the background estimation by misreconstructed gamma-rays. For the same reason regions surrounding known gamma-ray sources are excluded from the ring.
The normalization is given by the ratio of solid angles weighted with a factor taking into account the variation of the acceptance on the ring. The background acceptance may not be constant as a function of energy and therefore the ring background method is less suitable for spectrum measurements.

FoV Background Method

The FoV background method estimates the background from look-up tables. The look-up tables are filled with the radial acceptance in the FoV obtained by observations without any gamma-ray source. The radial acceptance is then rotated to derive a 2D acceptance map. The normalization is done by comparing the acceptance with the excess outside of the source region. A detailed description can be found in Aharonian et al. (2006a). This method can be used to derive excess sky maps. For large zenith angles the FoV background method shows a sight gradient in the direction of increasing zenith angle. In this case the approximation of a rotational symmetric acceptance is not good enough.

ON-OFF Background Method

In the ON-OFF background method the number of background events is estimated from observations without any significant source in the field of view. To account for differences in the acceptance these observations are chosen to match the zenith angle of the ON-observations. Furthermore, the time between the ON-observation and the OFF-observation has to be as short as possible to reduce the influence of changes in the optical efficiency of the system. The normalization between the number of ON and background events is the ratio of the exposure times.

The θ^2-Distribution

The θ^2-distribution shows the distance of all events which passed the image cuts (and are therefore gamma-ray-like) to the test position. The comparison with the background distribution helps to check for an excess of gamma-rays. In the following the generation on the background distribution is described.

The background distribution is obtained by adding up the squared angular distances to several positions in the field of view with the same offset as the test position, in the following called *OFF positions*. To avoid possible correlations it is important that each background event is used only ones. Therefore the angular distance between the OFF positions limits the maximal θ^2 up to which the background distribution can be used. One has to chose a compromise between reduced statistical uncertainties in the background distribution and a maximum range in θ^2. This is shown in Figure 4.6. The five OFF positions on the left hand side result in a small statstical uncertainty in the background distribution. Using three OFF-positions results in a distribution which can be used up to higher θ^2. The choice denpends on the offset with which the observation is performed.

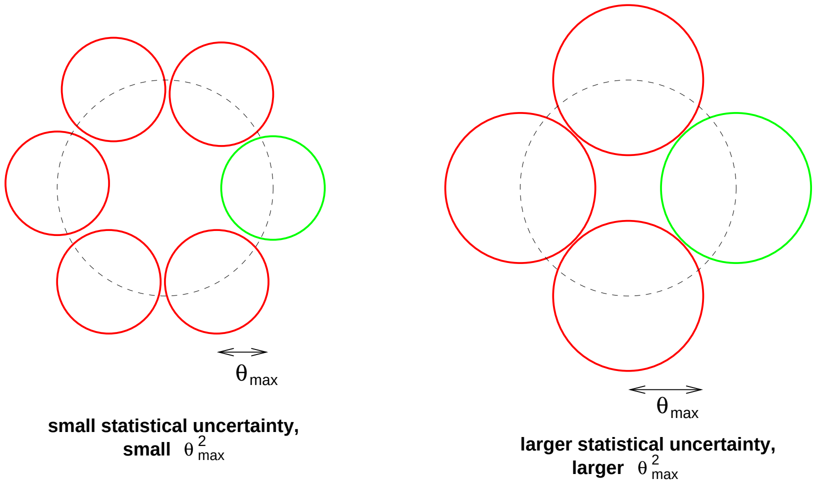
θmax
small statistical uncertainty,
small θ²max
θmax
larger statistical uncertainty,
larger θ²max

FIGURE 4.6: Comparison of five and three OFF positions in the determination of the background for the theta squared distribution.

4.4.6 Energy Reconstruction

For each telescope, the energy of an event is estimated by comparing the image size and the impact parameter to those of simulated gamma-ray shower images. The simulations have been performed at 13 zenith angles between 0 deg and 70 deg. The energy of the incident gamma ray is then calculated by the mean of the enegies obtained for each telescope. Again a linear interpolation in cosine zenith angle is used to derive the energies at zenith angles lying between simulated ones. The energy resolution is defined as the standard deviation of $(E_{\mathrm{reco}} - E_{\mathrm{true}})/E_{\mathrm{true}}$, where E_{reco} and E_{true} are the reconstructed and the simulated energy, respectively. For all energies this value is $\sim 15\%$.

4.4.7 Spectrum Determination

For the generation of the spectrum the data are logarithmically binned in energy. Only bins are used for which the difference between the mean reconstructed energy and the simulated energy is less than 10%, as derived from simulations. This results in an energy threshold, the *safe threshold*.
To estimate the gamma-ray flux in each energy bin the *collection area*, or *effective area*, of the system has to be determined. The effective area depends on energy, offset, zenith angle and image cuts applied to the camera pictures. It is derived from Monte Carlo simulations by counting the fraction of simulated events which trigger the detector and pass the image cuts and filled into lookup tables. The gamma-ray rate is given by a convolution of the flux with the effective area (Berge, 2006)

$$\frac{d}{dE_{\text{reco}}dt}N_\gamma = \int R(E_{\text{true}}, E_{\text{reco}})A_{\text{eff}}(E_{\text{true}})F(E_{\text{true}})dE_{\text{true}}, \tag{4.1}$$

where $R(E_{\text{true}}, E_{\text{reco}})$ is the response function, which is the probability that an event with a energy E_{true} is reconstruced with an energy of E_{reco}. A deconvolution of equation (4.1), which is needed to derive the source flux $F(E)$ from the measurement of the gamma-ray rate, cannot be perfomed analytically. In Berge (2006) three methods are discussed to overcome this problem. The method used in the standard analysis of H.E.S.S. data is to derive the effective area as a function of the reconstructed energy. Then the source flux is given by

$$F(E_{\text{reco}}) = \frac{1}{A_{\text{eff}}(E_{\text{reco}})} \cdot \frac{d}{dE_{\text{reco}}dt}N_\gamma \tag{4.2}$$

The disadvantage to this approach is that the effective area depends on the simulated specturm used in its determination. However, due to the good energy resolution of $\approx$ 15% in the H.E.S.S. analysis, this effect is small and can be disregarded in most cases.
The flux in each bin i is then given by

$$F_i = \frac{1}{(\Delta E)_i \cdot T_i}\left(\sum_{j=0}^{N_{\text{ON}}} \frac{1}{A_j} - \alpha \sum_{k=0}^{N_{\text{OFF}}} \frac{1}{A_k}\right), \tag{4.3}$$

where $(\Delta E)_i$ is the width of the energy bin, T_i is the exposure time and α is the normalization factor. N_{ON} and N_{OFF} are the number on ON-events and OFF-events, respectively.

4.4.8 Upper Limit Determination

In this section the determination of confidence intervals is discussed in detail, as this is needed in the analysis of Kepler's SNR and SN1006.
For observations without a significant gamma-ray excess an upper limit on the flux from this object can be calculated, taking into account the number of ON/OFF events and the conditions (zenith angle and offset) during observations. The number of ON and OFF events above a certain threshold are used

to calculate the maximal excess ex_{max} and minimal excess ex_{min} for a confidence level c. In the case of the minimal excess being zero the value for the maximal excess is an upper limit with the confidence level c. The remaining task is the determination of the confidence interval with the correct coverage, this is the interval $[\mu_1, \mu_2]$ for which $P(\mu \in [\mu_1, \mu_2]) = c$. In the following, first the construction of confidence intervals in general is discussed. Second the method of Feldman and Cousins (1998) is described, as it is used in the analysis of Kepler's SNR and SN1006.

Construction of the Confidence Interval

In the following it is assumed that one measures a quantity x to derive a value μ. The true value of μ is unknown. To derive a confidence interval for the value μ the following steps have to be performed. For every true value μ an interval $[x_1, x_2]$ is chosen for which the probability that the measured value x is within this interval is c, hence

$$P(x \in [x_1, x_2]|\mu) = c. \tag{4.4}$$

In practice this is done for a suitable number of discrete values to limit the processing time. An example is drawn in Figure 4.7. The interval $[x_1, x_2]$ is the acceptance interval for the value μ. Up to here it is not specified in what way the interval boundaries x_1 and x_2 have to be chosen. The most common choice is

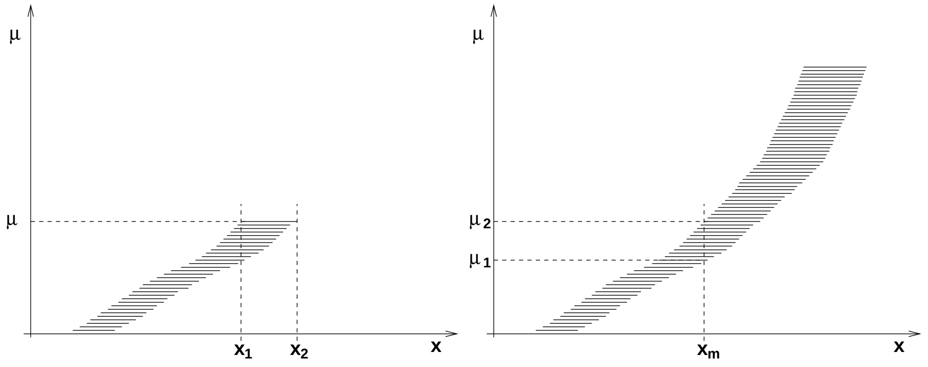

FIGURE 4.7: Construction of confidence intervals: *Left*: For every value of μ an interval $[x_1, x_2]$ is constructed for which $P(x \in [x_1, x_2]|\mu) = c$. This interval is called *acceptance interval.* *Right*: When measuring the quantity $x = x_{\mathrm{m}}$ a vertical line is drawn at this position in the graph. The confidence interval for the quantity μ is then the entirety of all μ-values corresponding to acceptance intervals crossed by the vertical line.

$$P(x < x_1|\mu) = 1 - c$$

for *upper confidence limits* (satisfying $P(\mu > \mu_2) = 1 - c$), and

$$P(x < x_1|\mu) = P(x > x_2|\mu) = (1 - c)/2$$

for *central confidence intervals* (satisfying $P(\mu < \mu_1) = P(\mu > \mu_2) = (1-c)/2$). Feldman and Cousins (1998) have introduced another method to get the acceptance interval for a given value μ. This is based on an sorting principle using a maximum likelihood method. For simplicity the sorting principle is shown in the following for the case where the measured quantity is the quantity of interest, $x = \mu$. In addition, it is assumed that the true value of x is always positive (as it is the case for the measurement of a flux, for example). It is assumed that the probability density function (pdf) is given by

$$P(x|\mu) = \frac{1}{\sqrt{2\pi}} \exp\left(-\frac{1}{2}(x-\mu)^2\right),$$

which is a Gaussian pdf with a variance of $\sigma = 1$. This is no limitation as this is always achievable by using x/σ instead of x.

Feldman & Cousins Construction of the Acceptance Intervals

In the approach by Feldman and Cousins (1998) the *likelihood ratio*

$$R(x) = \frac{P(x|\mu)}{P(x|\hat{\mu})}$$

is calculated for all values of x for a given μ. $\hat{\mu}$ is the value of μ that maximizes $P(x|\mu)$. Then the ratios $R(x)$ are sorted in descending order and the x values are added to the interval, accordingly to the sorting, as long as $\sum P(x|\mu)$ is below the confidence level c. This is done by drawing a horizontal line in the figure of $R(x)$ and calculating $\int_{x_1}^{x_2} P(x|\mu)$, where x_1 and x_2 are the x values where the horizontal line crosses the graph of $R(x)$ (see Figure 4.8). The horizontal line for which $\int_{x_1}^{x_2} P(x|\mu)dx = c$ specifies the acceptance interval for μ. As can be seen for small values of μ the acceptance interval is not symmetric with respect to $\hat{x}$, which maximizes the pdf. In the H.E.S.S. analysis the calculation is performed using discrete values x with a step size dx. In this case the integral becomes a sum $\sum_x P(x|\mu) \cdot dx = c$. The sum runs over the sorted x-values (beginning with the value for which $R(x)$ is maximal) until the confidence level is reached.

Calculating an Upper Limit for the Flux

Using the integrated number (from E_{min} to infinity) of ON and OFF events the confidence interval for the integrated excess is calculated. In the case of the lower end of the confidence interval ex_{min} being zero, the upper end ex_{max} is an upper limit for the excess at a confidence level of c. This upper limit can be used to calculate an upper limit for the integrated flux. Typically a power-law spectrum with a spectral index Γ is assumed and the normalization I_0 of the spectrum is calculated as follows. The differential spectrum can be written as

$$\left(\frac{dN}{dE}\right) = I_0 \left(\frac{E}{E_0}\right)^{-\Gamma}. \tag{4.5}$$

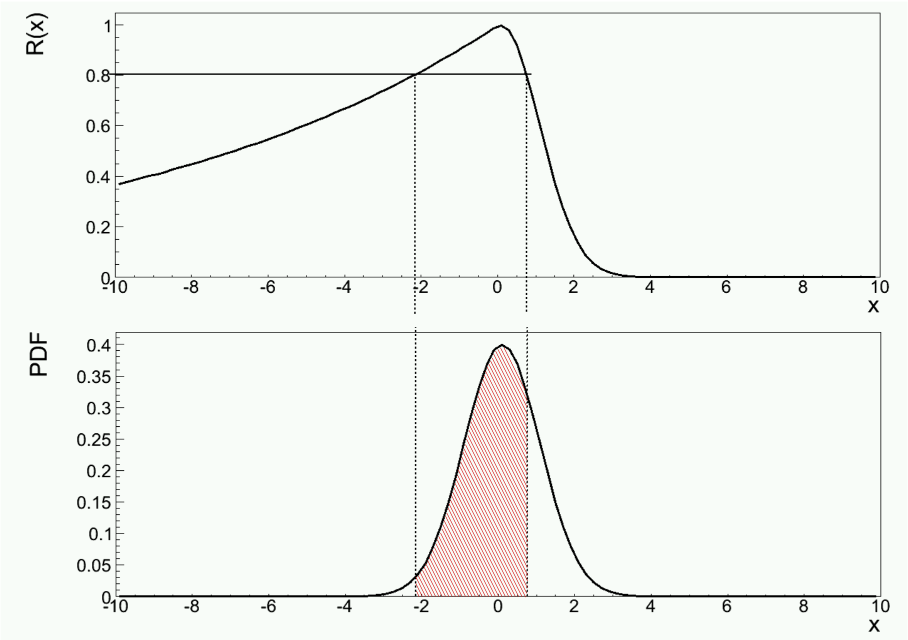

FIGURE 4.8: Feldman & Cousins approach to get acceptance intervals: Calculate $R(x)$, draw a horizontal line, calculate $\int_{x_1}^{x_2} P(x|\mu)dx$, change the position of the line until the integral over the pdf is equal to the confidence level.

The left side of this equation can be written as

$$\left(\frac{dN}{dE}\right) = \frac{N(E, E+dE)}{dE \cdot A(E) \cdot dt}, \tag{4.6}$$

where $N(E, E+dE)$ is the number of events with energies between E and $E+dE$, $A(E)$ is the effective area for that energy and t is the exposure time. Combining these two expressions and integrating over the energy and the time one gets

$$\begin{aligned} I_0 \left(\frac{E}{E_0}\right)^{-\Gamma} \cdot A(E) \cdot &= \frac{N(E, E+dE)}{dE \cdot dt} \\ \Rightarrow I_0 &= \frac{N(E_{\text{min}}, \infty)}{\int_{E_{\text{min}}}^{\infty} \int_{t_{\text{start}}}^{t_{\text{stop}}} \left(\frac{E}{E_0}\right)^{-\Gamma} \cdot A(E)\, dt\, dE}. \end{aligned} \tag{4.7}$$

For $N(E_{\text{min}}, \infty)$ the upper limit in excess is used. The normalization for the spectrum is then used to calculate the flux above a certain energy threshold E_{th}

$$F(> E_{\text{th}}) = \int_{E_{\text{th}}}^{\infty} I_0 \left(\frac{E}{E_0}\right)^{-\Gamma} dE. \tag{4.8}$$

The upper limit on the energy flux in then given by

$$F_E(> E_{\text{th}}) = \int_{E_{\text{th}}}^{\infty} I_0 \cdot E \left(\frac{E}{E_0}\right)^{-\Gamma} dE. \tag{4.9}$$

For an assumed spectral index of $\Gamma \leq 2.0$ the upper integration limit can not be ∞ as in this case the integral is strictly monotonic increasing.

Chapter 5

Kepler's SNR

On October the 9th in 1604 a "new star" was observed. The message about this event reached the famous astronomer Johannes Kepler a few days later in Prague, where he worked in the former laboratory of Tycho Brahe. However, he had to wait until October the 17th 1604 before he could observe the occurrence because of bad weather in Prague. Kepler studied the "stella nova" over the course of a year and published his findings in 1606 (Johannes Kepler: Stella Nova, 1606).

More than 400 years later the remnant of the event observed by Kepler is a well studied object across all wavelengths. At the position of the historic event a shell-type SNR can be found today. Figure 5.1 is a combined image of Kepler's SNR with data from Spitzer ($24\,\mu$m, red), Hubble (Hα, yellow) and Chandra ($0.3 - 1.0\,$keV, green and $2 - 10\,$keV, blue).

From observations at radio wavelengths Dickel et al. (1988) determine an angular diameter of $200''$ and an average expansion follows of $R \propto t^{0.5}$. The expansion rate varies strongly over the remnant. At the southern rim the the expansion law is $R \propto t^{0.65}$ and at the norther rim it is $R \propto t^{0.35}$.

In the X-ray regime strong emission lines from Si, S, Ar, Ca and Fe have been found with EINSTEIN (Becker et al., 1980b), EXOSAT (Smith et al., 1989), GINGA (Hatsukade et al., 1990), ASCA (Kinugasa and Tsunemi, 1999) and XTE (Decourchelle and Petre, 1999). From data obtained with the XMM-Newton satellite, Cassam-Chenaï et al. (2004) discuss the spatial variations over the remnant. The authors claim that the Fe-K emission peaks at a smaller radius than the Fe-L emission and conclude that the temperature increases inwards in the ejecta.

In spite of the numerous observations the distance to Kepler's SNR is still not known. Reynoso and Goss (1999) report on a weak HI absorption feature in VLA data at $21.3\,\mathrm{km\,s^{-1}}$. They use the rotation model of Fich et al. (1989) to calculate a lower limit on the distance of $(4.8 \pm 1.4)\,$kpc. The authors note that the rotation model is not very accurate for such small angular distances to the Galactic center. However, they also give an upper limit of $6.4\,$kpc due to the lack of absorption by a molecular cloud at that distance.

The type of the supernova is still under debate. From the reconstructed light curve Baade (1943) claim it to be a type Ia SN. Doggett and Branch (1985)

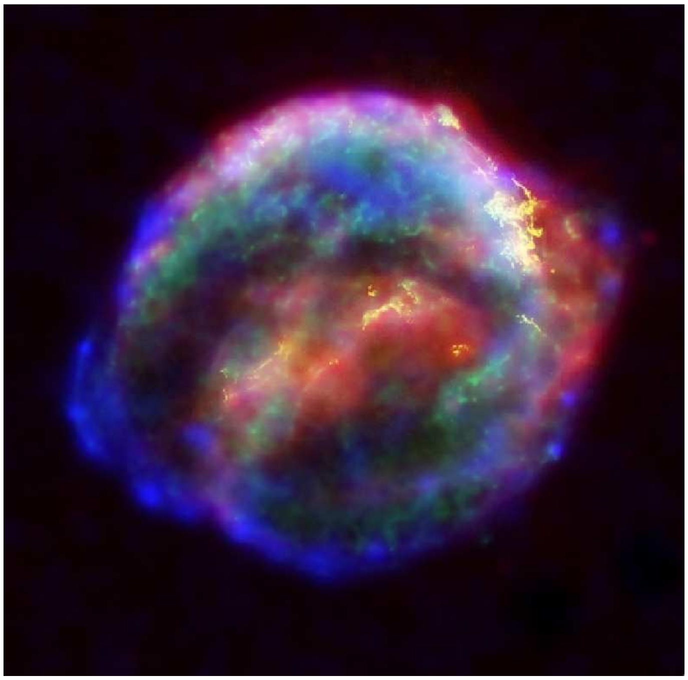

FIGURE 5.1: Color-composite picture of Kepler's SNR in different wavelengths: Spitzer ($24\,\mu$m, red), Hubble (Hα, yellow) and Chandra ($0.3 - 1.0$ keV, green and $2 - 10$ keV blue). The picture is taken from Blair et al. (2007).

argue that the light curve is also consistent with a type II-L. Smith et al. (1989) and Kinugasa and Tsunemi (1999) have observed a relative overabundance of heavy elements that agrees with type Ia nucleosynthesis models, while Decourchelle and Ballet (1994) see more evidence that Kepler's SNR is the remnant of a core-collapse SN. More recently modeling of the thermal line spectrum obtained with XMM (Cassam-Chenaï et al., 2004) led Badenes et al. (2005) to the conclusion that the X-ray spectrum is best fit by a type Ia SN.
In the following the data on Kepler's SNR from H.E.S.S. observations and their analysis are presented.

5.1 H.E.S.S. Observations and Results

Kepler's SNR was observed with the H.E.S.S. array between May 2004 and July 2005 for a total observation time of 14 hrs. The observations were performed in wobble mode around the radio position of Kepler's SNR (RA $17^{\mathrm{h}}30^{\mathrm{m}}42.12^{\mathrm{s}}$ Dec $-21^{\circ}28'59.9''$ J2000). Wobble offsets between 0.48 deg and 0.76 deg in both Right Ascension and Declination were used. The data were taken at zenith angles from 3 deg to 45 deg with a mean zenith angle of 13 deg. After applying the H.E.S.S. standard data selection (see Section 4.1) a total live time of 13 h is available for analysis. The standard analysis chain for H.E.S.S. data is used, as described in Section 4.4.

The mean angular resolution of the analysis is $\sim 400''$. Compared to a diameter in radio of $200''$ Kepler's SNR is expected to be a point source for H.E.S.S. All events reconstructed within $400''$ around its radio and X-ray position, which pass the gamma-ray cuts, are counted as gamma-ray-like events originating from Kepler's SNR. The background is estimated using two different methods. For the investigation of the flux the Reflected Background method is used and the significance sky map is made with the Ring Background method (see 4.4.5).
In the upper panel of Figure 5.2 a significance sky map (showing at each position the significance for an excess at this position) around the position of Kepler's SNR is presented. There is no significant excess visible above the background. In the lower panel of Figure 5.2 the distribution of the significance in the field of view is shown. A Gaussian is fitted to the distribution. The best fit is given for a standard deviation of 1.033 ± 0.003 and a mean at -0.020 ± 0.003 with $\chi^2/\text{d.o.f.} = 76/22$. The bins of both the significance map and the significance distribution are highly correlated, as for the generation of the significance map the raw event map and the corresponding background map are oversampled with a radius of 0.1 deg. Due to that the errors of the Gaussian fit should be higher. It is concluded here that the significance distribution is compatible with fluctuations in the background.
An alternative way to check for a gamma-ray excess is to plot the distribution of the squared angular distance θ^2 of all measured events to the position of Kepler's SNR. This is then compared to the background distribution. In the left panel of Figure 5.3 the θ^2 distribution and the corresponding background distribution is shown. There is no gamma-ray excess above the background at the position of Kepler's SNR. The background distribution was obtained using three OFF-positions as described in Section 4.4.5. The background is uncorrelated up to a squared angular distance of $0.15\,\text{deg}^2$.

5.2 Upper Limit on the Integrated Energy Flux

For the flux determination the Reflected Background method is used as it is most suitable for this purpose (see Section 4.4.5). The number of possible OFF regions depends on the wobble offset. This offset varies with each run. In this analysis the number of OFF regions was set to 11 as this is the maximal number of OFF regions possible for all observations of Kepler's SNR. This was done to reduce systematic effects. Using the standard analysis, 827 ON and 8855 OFF events (with a normalization factor of $\alpha = 0.0911$) are recorded, resulting in an total excess of gamma rays from the direction of Kepler's SNR of 20 ± 30. The total significance is 0.68 standard deviations.
The non-detection results in an upper limit on the gamma-ray flux from Kepler's SNR. The upper limits are obtained using the approach from Feldman and Cousins (1998) (see Section 4.4.8). At a confidence level of 99% an upper limit on the integrated photon flux above 230 GeV of $F(> 230\,\text{GeV}) < 9.3 \times 10^{-13}\,\text{cm}^{-2}\,\text{s}^{-1}$ is derived, assuming a photon index of $\Gamma = 2.0$.
The 99% confidence-level limit on the integrated energy flux $F_E(E_1, E_2) =$

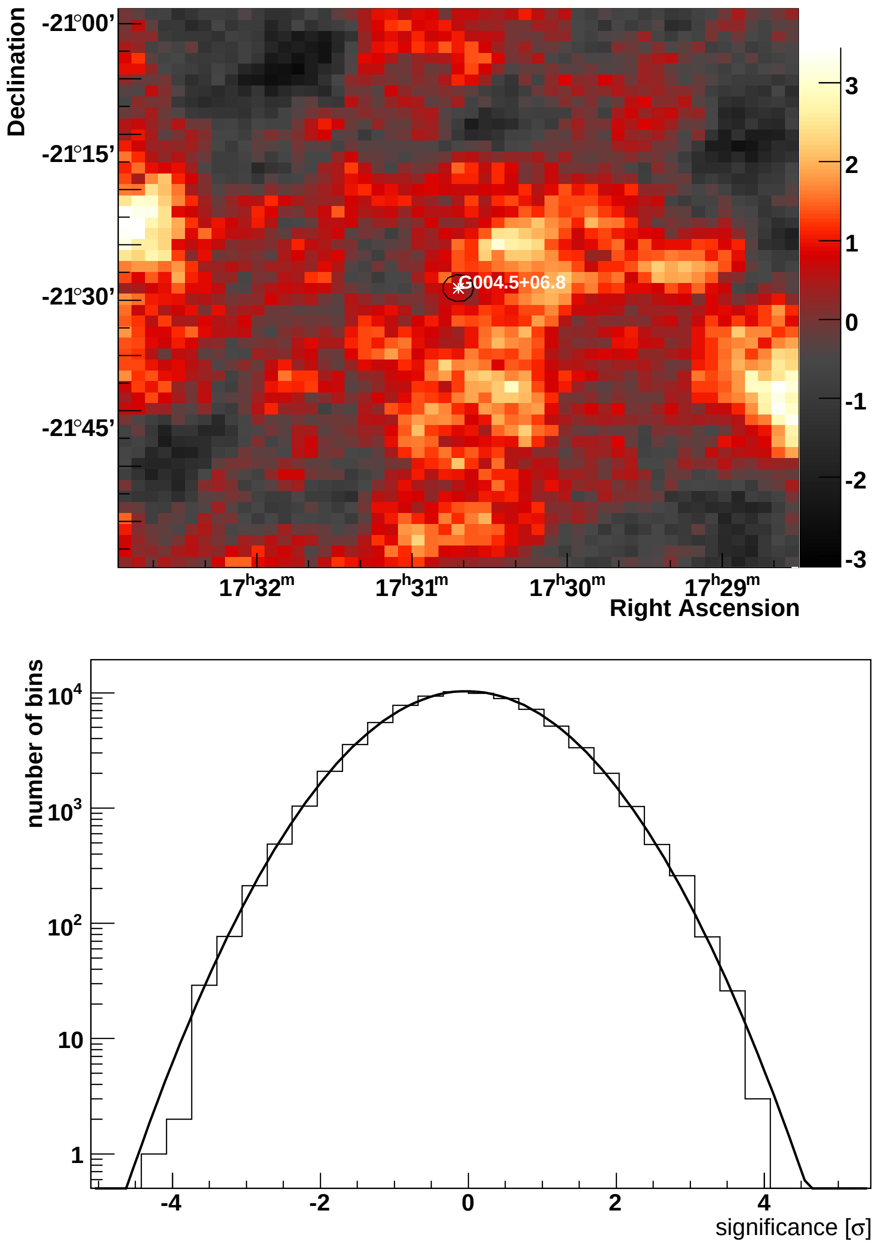

Figure 5.2: *Top:* Significance sky map centered at the radio position of Kepler's SNR. Each bin shows the significance for a gamma-ray excess at this position. *Bottom:* Significance distribution in the field of view. The line is a Gaussian fit to the data.

$\int_{E_1}^{E_2} E{\cdot}dN/dE\ dE$ from Kepler's SNR is $F_E(230\,\mathrm{GeV}, 12.8\,\mathrm{TeV}) < 8.6{\times}10^{-13}\,\mathrm{erg\,cm^{-2}\,s^{-1}}$.

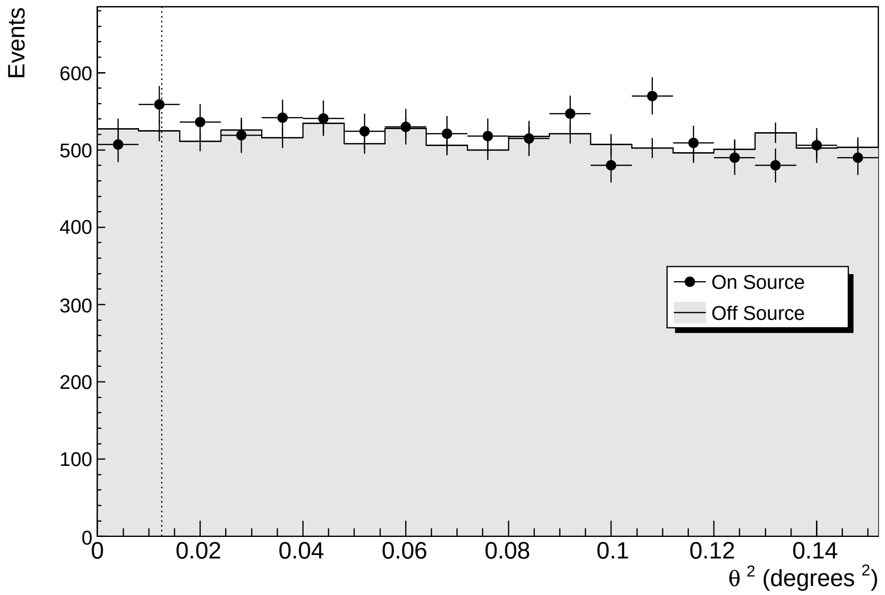

FIGURE 5.3: Distribution of the squared angular distances of all events to the center of Kepler's SNR compared to the background distribution.

To study the influence of the assumption of the photon index the upper limit on the photon flux

$$\begin{aligned} F(>E) &= \int_E^\infty I_{0,\Gamma} \left(\frac{E}{1\,\mathrm{TeV}}\right)^{-\Gamma} dE = \\ &= \frac{I_{0,\Gamma} \cdot 1\,\mathrm{TeV}}{\Gamma - 1} \left(\frac{E}{1\,\mathrm{TeV}}\right)^{-\Gamma+1} \end{aligned} \tag{5.1}$$

is determined for $0.23 < (E/1\,\mathrm{TeV}) < 3.7$ assuming two different photon indices $\Gamma = 2.0$ and $\Gamma = 3.0$. The normalization $I_{0,\Gamma}$ is derived as described in Section 4.4.8.

Figure 5.4 shows the obtained upper limits at 99% confidence level. The figure shows that the limits are only weakly dependent on the assumption of the photon index, at least in the range $\Gamma = 2.0 - 3.0$.

In the following section the upper limits are used to constrain parameters of Kepler's SNR.

5.3 Nature of the Accelerated Particles

Assuming a pure hadronic or a pure leptonic scenario (see Section 2.5), upper limits on parameters of Kepler's SNR can be derived. In a pure hadronic scenario an upper limit on the total energy in accelerated protons can be given. The assumption of a pure leptonic scenario allows to compare the measured upper limit in gamma rays with a theoretical upper limit based on X-ray observations for a given magnetic field strength.

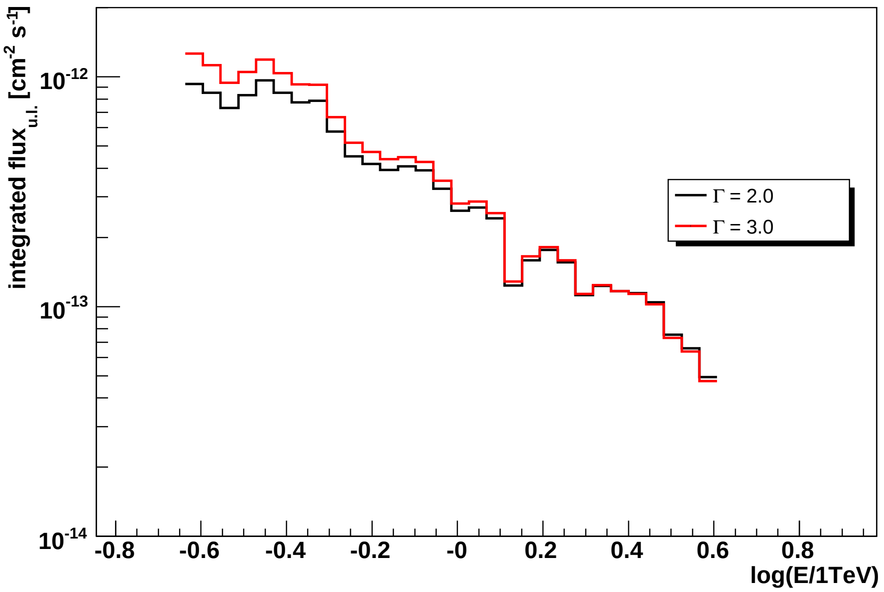

FIGURE 5.4: Upper limits for the integrated flux for energies in the range $0.23 < (E/1\,\mathrm{TeV}) < 3.7$ for two different assumed indices, $\Gamma = 2.0$ (black) and $\Gamma = 3.0$ (red).

5.3.1 Hadronic Scenario

Using the integrated energy flux in gamma rays F_E in the range between 0.23 TeV and 12.8 TeV, the gamma-ray luminosity $L_\gamma(E_1, E_2) = 4\pi d^2 F_E(E_1, E_2)$ can be estimated, where d is the distance of the observer to the remnant. The integrated energy upper limit derived above results in an upper limit of the luminosity $L_\gamma < 1.0 \times 10^{32} \cdot (d/\mathrm{kpc})^2\ \mathrm{erg\,s^{-1}}$. In a pure hadronic scenario the upper limit on the luminosity results in an upper limit on the total energy in accelerated protons $W_\mathrm{p} = L_\gamma \tau_{\mathrm{pp}\to\pi^0}$, where $\tau_{\mathrm{pp}\to\pi^0}$ is the cooling time of the protons through π^0-production in interactions with the ambient medium and subsequent π^0-decay (see Section 2.5.1). For proton energies above $\sim 100\,\mathrm{GeV}$ it can be approximated with $\tau_{\mathrm{pp}\to\pi^0} \sim 5.1 \times 10^{15}\,\mathrm{s}\,\left(n/\mathrm{cm}^{-3}\right)^{-1}$ Therefore the upper limit on the energy in accelerated protons being capable to produce photons measured by H.E.S.S. is $W_\mathrm{p} < 5.1 \times 10^{47}\,\mathrm{erg}\,(d/\mathrm{kpc})^2\left(n/\mathrm{cm}^{-3}\right)^{-1}$. As mentioned before, the distance to the remnant and the density of the material surrounding the remnant are not known. Using an upper limit for the distance of $d \leq 6.4\,\mathrm{kpc}$ and a lower limit for the density of $n \geq 0.1\,\mathrm{cm}^{-3}$ (due to Kepler's position well above the plane) a conservative upper limit for the energy in accelerated protons of $W_\mathrm{p} < 2.1 \times 10^{50}\,\mathrm{erg}$ is derived.

In a single interaction on average $\sim 17\%$ of the proton energy is converted into gamma rays. Therefore the gamma rays measured with H.E.S.S. correspond to protons with energies in the range $\sim (1.4 - 70)\,\mathrm{TeV}$ (Aharonian and Atoyan, 2000). However, the protons, accelerated in an SNR are assumed to cover a much wider range. Assuming a coverage from $\sim$ 1 GeV up to 3 PeV and a particle index of -2.0, the H.E.S.S. range corresponds to

$$\frac{\int_{1.4\,\mathrm{TeV}}^{70\,\mathrm{TeV}} F_E\,dE}{\int_{0.001\,\mathrm{TeV}}^{3000\,\mathrm{TeV}} F_E\,dE} = \frac{\log(70\,\mathrm{TeV}/1.4\,\mathrm{TeV})}{\log(3000\,\mathrm{TeV}/0.001\,\mathrm{TeV})} = 0.26 \tag{5.2}$$

i.e. $\sim 26\%$ of the total energy in protons. Therefore the upper limit of the total energy in accelerated protons is 8.1×10^{50} erg.

If one assumes that Kepler's SNR is the remnant of a type Ia SN the explosion energy can be estimated. The typical kinetic energy of SN Ia explosions is $(1 - 1.5) \times 10^{51}$ erg (Gamezo et al., 2003).

As discussed in Section 2.4 it is estimated that type Ia SN could deposit 10% to 30% of their explosion energy into accelerated particles. For an assumed explosion energy of 10^{51}erg the energy in accelerated protons would then be $(1 - 3) \times 10^{50}$ erg. The conservative upper limit derived by H.E.S.S. is well above the assumed value and therefore does not constrain any parameter of the explosion. In Section 5.4 a more constraining upper limit is derived by using predictions of a theoretical model.

5.3.2 Leptonic Scenario

In a purely leptonic scenario all VHE gamma rays are emitted by accelerated electrons via inverse Compton (IC) scattering. Electrons which are accelerated to very high energies can also emit synchrotron photons in the X-ray domain when they are deflected in magnetic fields in the SNR. Therefore the emission in VHE gamma rays is correlated with the emission in X-rays (see Section 2.5). As mentioned above, for a given magnetic field B the energy flux in IC gamma rays f_{IC} at the energy E_{IC} corresponds to the energy flux from synchrotron emission f_{syn} with an energy

$$(E_{\mathrm{syn}}/1\,\mathrm{keV}) \simeq 0.07 \cdot (E_{\mathrm{IC}}/1\,\mathrm{TeV})\,(B/10\,\mu\mathrm{G})\,. \tag{5.3}$$

The ratio of the energy fluxes in X-rays and gamma rays emitted by the same electrons is then given by

$$\frac{f_{\mathrm{IC}}(E_{\mathrm{IC}})}{f_{\mathrm{syn}}(E_{\mathrm{syn}})} \simeq 0.1(B/10\,\mu\mathrm{G})^{-2}\xi, \tag{5.4}$$

where ξ is a factor taking into account different sizes of the emission regions for X-rays and gamma rays. This relation is used in the following to derive an upper limit on the energy flux in gamma rays assuming a certain value for the magnetic field in the remnant. The value ξ is assumed to be equal to 1.

The total magnetic field of Kepler's SNR was measured by Matsui et al. (1984). By measuring the polarization of the synchrotron emission the authors obtain a total magnetic field of 74 μG. Völk et al. (2005) derived a magnetic field of 215 μG from the width of X-ray filaments in the southeastern part measured by XMM (Cassam-Chenaï et al., 2004). For the following analysis a magnetic field of 74 μG is assumed.

To estimate the upper limit at $E_{\mathrm{IC}} = 1\,\mathrm{TeV}$ the energy flux at $E_{\mathrm{syn}} = 0.5\,\mathrm{keV}$

has to be used (equation (5.3)). Kepler's SNR was observed in X-rays by several experiments. However, for energies below 10 keV it was not possible to disentangle the non-thermal part of the spectrum from the thermal one for the whole remnant. Therefore, to derive an upper limit for the gamma rays, RXTE data with energies between 10 keV and 20 keV are used (Allen, 1999). The disadvantage of PCA, which is the X-ray instrument on board of RXTE, is that it has no imaging capabilities. This means that the flux observed by this instrument is the integrated flux from the whole FoV of 1 deg. It is expected that most of the measured flux comes indeed from Kepler's SNR because of its position well above the Galactic plane. Nevertheless, for the estimation of the upper limit for the gamma-ray flux the X-ray flux has to be treated as an upper limit.
The X-ray flux measured by PCA at an energy of 10 keV is $6.2 \times 10^{-5}\,\mathrm{cm}^{-2}\,\mathrm{s}^{-1}\,\mathrm{keV}^{-1}$ and the spectral index is $\Gamma = 3$. To compare the measured spectrum from PCA with the upper limit obtained by H.E.S.S. at 1 TeV, the X-ray flux has to be extrapolated down to 0.5 keV. This is done using a formula derived by Zirakashvili and Aharonian (2007) (equation (37)). As the exact spectral points from the PCA measurement are not available 13 spectral points are taken from Figure 2 of Allen (1999). The error is assumed to be 10% for the whole range. From the extracted data points the energy flux $E^2F(E)$ is calculated and fitted by the formula mentioned above. The extracted data points and the extrapolation are shown in Figure 5.5. The spectrum derived by the fit is

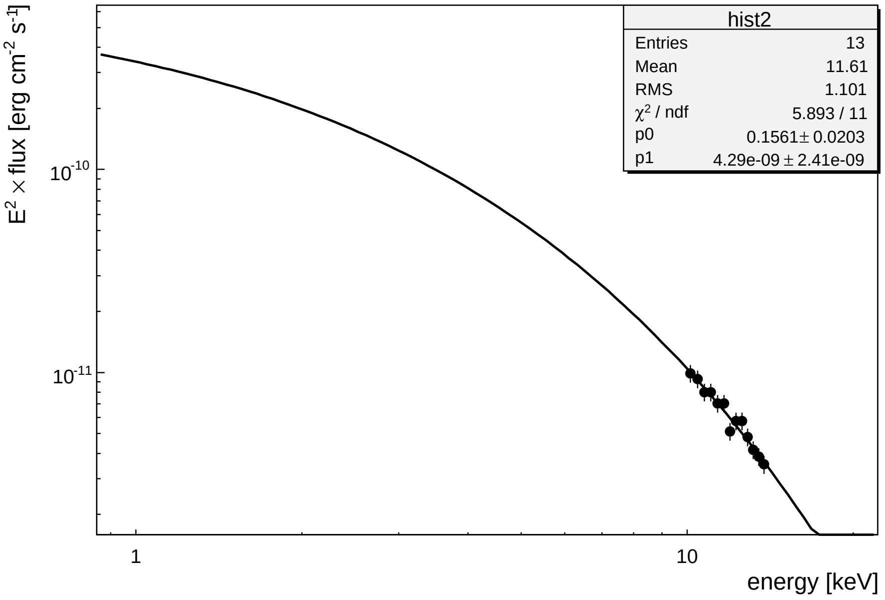

FIGURE 5.5: Fit of a formula derived by Zirakashvili and Aharonian (2007) to the X-ray data on Kepler's SNR form RXTE.

$$\begin{aligned} E^2F(E) = (4.3 \pm 2.4) \quad & \times \quad 10^{-9}\left(1 + 0.38 \cdot \sqrt{\frac{E}{(0.16 \pm 0.02)\,\mathrm{keV}}}\right)^{11/4} \\ & \times \quad \exp\left(-\sqrt{\frac{E}{(0.16 \pm 0.02)\,\mathrm{keV}}}\right) \mathrm{erg\,cm^{-2}\,s}. \end{aligned} \tag{5.5}$$

Therefore the extrapolation down to 0.5 keV reveals $f_{\mathrm{syn}}(0.5\,\mathrm{keV}) = 4.6 \times 10^{-10}\,\mathrm{erg\,cm^{-2}\,s^{-1}}$.

Using equation (5.4) with an assumed magnetic field of $74\,\mu\mathrm{G}$ an upper limit on the flux in gamma-rays can be estimated. The upper limit on the energy flux in gamma-rays is

$$f_{\mathrm{IC}} = 8.4 \times 10^{-13}\,\mathrm{erg\,cm^{-2}\,s^{-1}} \tag{5.6}$$

This value is the energy flux upper limit defined by $E^2F(E)$. The upper limit which is derived by H.E.S.S. is, for $\Gamma \neq 2$, given by

$$\begin{aligned} \int_E^{\infty} E' \cdot F(E')dE' &= \int_E^{\infty} I_0 E' \left(\frac{E'}{1\,\mathrm{TeV}}\right)^{-\Gamma} dE' = \\ &= \frac{I_0(1\,\mathrm{TeV})^2}{\Gamma - 2}\left(\frac{E}{1\,\mathrm{TeV}}\right)^{-\Gamma+2} = \\ &= \frac{E^2F(E)}{\Gamma - 2}. \end{aligned} \tag{5.7}$$

Therefore the estimated upper limit (5.6) has to be divided by $\Gamma - 2$ to be comparable with the H.E.S.S. upper limit. As mentioned above this is only true (and can only be done) for $\Gamma \neq 2$. Here the upper limit which is derived with an assumed index of $\Gamma = 3.0$ is used and therefore the upper limits can by compared directly. The H.E.S.S. upper limit is $4.3 \times 10^{-13}\,\mathrm{erg\,cm^{-2}\,s^{-1}}$. The two upper limits are comparable to each other. Therefore, with the assumed magnetic field, the H.E.S.S. upper limit does not constrain the leptonic model.

5.4 Comparison with Theory

Berezhko et al. (2006) (BKV) estimate the expected flux in VHE gamma rays from Kepler's SNR assuming the SN to be of type Ia. Their non-linear kinetic theory of cosmic-ray acceleration is based on a fully time-dependent, spherical-symmetric solution of the cosmic-ray transport equation. They also take into account the non-linear coupling to the dynamic equations for the thermal gas component. To account for the uncertainty in the distance BKV calculate the flux for assumed distances in the range of $(3.4 - 7)$ kpc. The density of the surrounding ambient medium is derived using the size and the expansion velocity of Kepler's SNR. They give the theoretical curve for the quantity $\epsilon \cdot f_\epsilon$, where ϵ is the energy and f_ϵ is the integrated photon flux above ϵ.

To compare the H.E.S.S. upper limit with the prediction from BKV the value $\tilde{F}(> E) = E \cdot F(> E)$ is calculated, where $F(> E)$ is the upper limit on the photon flux above E. For $E = 230\,\mathrm{GeV}$ one gets $\tilde{F}(> 230\,\mathrm{GeV}) < 3.4 \times$

$10^{-13}\,\mathrm{erg\,cm^{-2}s^{-1}}$. This quantity is calculated for several energies in the H.E.S.S. range to compare it with the theoretical curves. The results are plotted in Figure 5.6 together with the prediction from BKV for different assumed distances and an assumed explosion energy of $E_{\mathrm{SN}} = 10^{51}$ erg. In the framework of the BKV modeling the H.E.S.S. upper limit results in a lower limit on the distance of 6.4 kpc for explosion energies $E_{\mathrm{SN}} \geq 10^{51}$ erg. The corresponding lower limit on the density of the ambient medium is $0.7\,\mathrm{cm^{-3}}$.

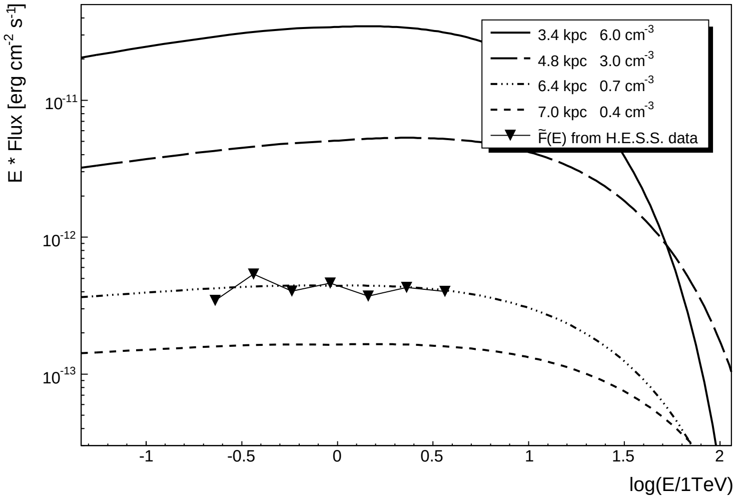

FIGURE 5.6: The predictions of BKV for different assumed distances are plotted together with the corresponding upper limits obtained by H.E.S.S. The densities are derived using the size of Kepler's SNR and its expansion velocity.

The conservative upper limit for the total energy in accelerated protons as derived in Section 5.3.1 can now be recalculated using the values derived by the comparison of the H.E.S.S. upper limit and the predictions from BKV. The distance is again estimated to be 6.4 kpc and the density is obtained using the size and the expansion speed (from BKV). The upper limit for the total energy in accelerated protons in the range 1 GeV − 3 PeV is then 1×10^{50} erg, which is 10% of the assumed explosion energy for a type Ia SN. This value constrains the portion of the energy which is deposited in accelerated protons to < 10%.
BKV derive a magnetic field of $480\,\mu$G by a fit to the overall synchrotron spectrum. This value corresponds to the interior of the remnant. From the smallest filaments in X-rays observed by Chandra (Bamba et al., 2005) they get a magnetic field of $340\,\mu$G. This value corresponds to a small region behind the shock. Using this value the upper limit on the energy flux in gamma rays is again calculated. With a magnetic field of $340\,\mu$G the gamma-ray emission at 1 TeV has to be compared to the synchrotron emission at 2.4 keV. Using again the fit to the 13 points from the RXTE spectrum the energy flux in X-rays is $f_{\mathrm{syn}} = 1.6 \times 10^{-10}\,\mathrm{erg\,cm^{-2}\,s^{-1}}$. The upper limit on the energy flux in gamma rays is then given by

$$f_{\mathrm{IC}} < 1.4 \times 10^{-14} \mathrm{erg\,cm^{-2}\,s^{-1}}. \tag{5.8}$$

This upper limit is more than an order of magnitude below the H.E.S.S. upper limit. This means that in the case of such a high magnetic field any detection of VHE gamma rays from Kepler's SNR by a H.E.S.S.-like experiment would originate from accelerated protons.

5.5 Distance

As mentioned above, Reynoso and Goss (1999) derived an upper limit on the distance of 6.4 kpc. In the framework of the model of BKV the H.E.S.S. upper limit on the energy flux results in a lower limit of 6.4 kpc. The latter limit is derived under the assumption that the explosion energy is $\geq 10^{51}$ erg and that the supernova was of type Ia. On the basis of qualitative arguments BKV (equation (3)) give for dependence of the π^0-decay gamma-ray flux on the explosion energy E and the distance d

$$F_\gamma \propto E^2/d^7. \tag{5.9}$$

This is in rough agreement of the numerical results derived in the model of BKV and used in the following for the discussion of the energy dependence lower limit on the distance.

Assuming an explosion energy of 0.8×10^{51} erg (which is a lower limit for the explosion energy derived by most models (see e.g. BKV)) the constraint on the distance is weakened to

$$d > 6.4\,\mathrm{kpc} \cdot \left(\frac{E}{10^{51}\,\mathrm{erg}}\right)^{\frac{2}{7}} = 6.0\,\mathrm{kpc}. \tag{5.10}$$

Therefore the more conservative lower limit derived with H.E.S.S. (and using the model of BKV) is 6.0 kpc. The range for the distance to Kepler's SNR is then reduced to $6.0 < (d/1\,\mathrm{kpc}) < 6.4$.

Chapter 6

RX J0852.0-4622 (Vela Junior)

In this chapter the analysis of H.E.S.S. data on the supernova remnant RX J0852.0-4622 is presented.
The shell-type SNR RX J0852.0-4622 is located in the southeastern part of the Vela SNR, what led to the name *Vela Junior*. It was discovered within the ROSAT All Sky Survey above 1.3 keV (Aschenbach, 1998). Below this energy the emission is dominated by thermal emission from the Vela SNR. In X-rays this remnant is roughly circular with a diameter of 2 deg and it brightens towards the north-western, western and southern part of the shell and to the center. Observations with ASCA demonstrated the non-thermal origin of the X-ray emission (Tsunemi et al. (2000), Slane et al. (2001)). Based on observations with the COMPTEL satellite Iyudin et al. (1998) reported the detection of the 1.156 MeV ^{44}Ca line from the ^{44}Ti radioactive decay from namely GRO J0852-4642 which is associated with Vela Junior. Because of the short lifetime of ^{44}Ti ($\tau \approx 90\,\mathrm{yr}$) this association favors a very young SNR. In this case, the large angular size requires a small distance to the remnant. Based on the ^{44}Ti gamma-ray flux and the X-ray diameter Aschenbach et al. (1999) calculate an age of $\sim 680\,\mathrm{yr}$ and a distance of $\sim 200\,\mathrm{pc}$. Therefore Vela Junior would be very close to the Vela SNR which is supposed to be at $\sim 200\,\mathrm{pc}$.
It has been suggested that some spikes in nitrate concentration in some Antarctic ice cores are associated with close-by SNRs. One could be associated to the progenitor of Vela Junior (Burgess and Zuber, 2000), resulting in an age of $\sim 680\,\mathrm{yr}$. However, reanalysis of the COMPTEL data finds ^{44}Ti emission at a significance of only $2-4$ standard deviations (Schönfelder et al., 2000). Therefore the association with GRO J0852-4642 has to be questioned.
The best fit of a power-law to ASCA data revealed a much larger value for the interstellar absorbing column density than that of Vela SNR (Slane et al., 2001). This indicates a larger distance for Vela Junior. Based on CO data Slane et al. (2001) also give an upper limit for the distance due to the lack of absorption over the size of Vela Junior by the Vela Molecular Ridge, which is at a distance of $(1-2)\,\mathrm{kpc}$.
In deep X-ray observations a central object was detected (Aschenbach (1998),

Mereghetti (2001): SAX J0852.0-4615, Pavlov et al. (2001): XOU J085201.4-461753). Due to its spectrum it is suggested that the emitter is a neutron star (Kargaltsev et al., 2002). If the neutron star is associated with the remnant Vela Junior, the supernova have been a core collapse SN. However, the comparison of the high velocity of the Ti ejecta measured in X-rays with explosion models lead Iyudin et al. (2005) to the suggestion that the explosion was a sub-Chandrasekhar type Ia SN. In this case no central object remains from the explosion. Furthermore, Reynoso et al. (2006) report on the detection of an low emission elongated structure in the center of Vela Junior which could be explained by a planetary nebula. In this case the SN is more likely of type Ia.
In Section 6.1 the observation and the analysis are presented. Then the morphology in VHE gamma rays of the remnant is studied. Section 6.3 shows the results of a spectral analysis and in Section 6.4 the emission in VHE gamma rays is compared with the emission in X-rays.

6.1 H.E.S.S. Observations and Analysis

Vela Junior was observed between December 2004 and January 2007 for a total observation time of 39 hrs with the entire H.E.S.S. array. The data was taken in wobble mode with wobble offsets in both Right Ascension and Declination between 0.5 deg and 1.8 deg. The zenith angles of the observation ranged from 22 deg to 50 deg with a mean of 31 deg. After applying standard H.E.S.S. quality criteria a total of 34 hrs data is available for the analysis. The energy threshold of the data is 545 GeV. The data are calibrated as described in Section 4.2. The standard image cleaning procedure is applied.
Some of the observations (14 out of 84) were performed with a pointing within the SNR (diameter $\sim$ 2 deg). Therefore the Reflected Background method cannot be used for the analysis of the whole data set. For the spectral analysis of the whole data set the background is estimated from observations with the same zenith angle. The background is derived from a region in the FoV with the same size and offset as the source region in the observation. The excess and significance maps are derived with the FoV Background. To check the consistency of the results a subset of the data is analyzed with the Reflected Background method and compared to the results from the ON-OFF Background method.

6.2 Morphology

In the analysis of the morphology of extended sources like Vela Junior the angular resolution is an important parameter. To increase the angular resolution of the H.E.S.S. array the analysis is restricted to events with at least 200 p.e. in each participating camera. Showers which have been recorded by more than two telescopes allow a better direction reconstruction, also which further increase the angular resolution. This results in an angular resolution of $\sim$ 0.06 deg.

6.2.1 General Morphology of the Remnant

The morphology of the remnant is derived by the generation of a gamma-ray excess sky map. The sky maps shown here are generated using the FoV background method (see Section 4.4.5). The morphology of Vela Junior is shown in Figure 6.1. The figure is a 4 deg × 4 deg cut-out of the excess in gamma rays around Vela Junior. The sky map is smoothed with a Gaussian with a standard deviation of 0.06 deg to account for the angular resolution of the H.E.S.S. array with the used image cuts. Remarkable in this figure is the clear thin shell of the remnant with a radius of 1 deg and a width of ~ 0.2 deg. It is visible over the whole remnant but most prominent in the north-western part.

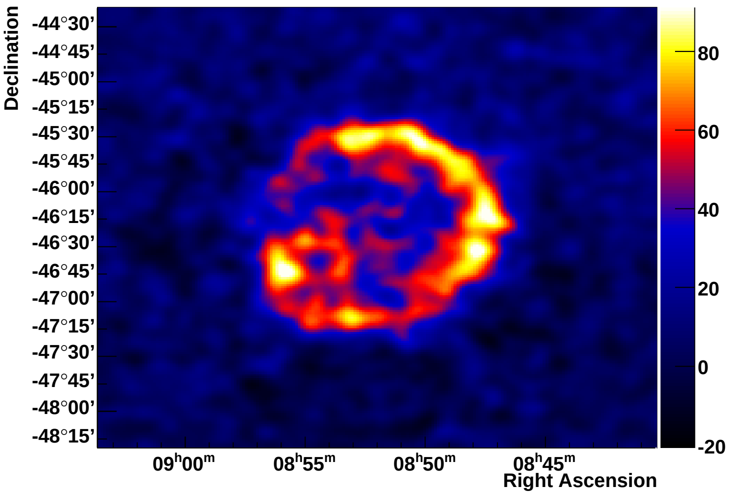

Figure 6.1: Excess sky map of Vela Junior

To check the background estimate used for the morphology the radial profile of the sky map showing all reconstructed events is compared to the background profile. This is shown in Figure 6.2. The regions which have been used are shown in Figure 6.7. As can be seen in the figure, outside of Vela Junior the FoV background is a good estimate of the background. For radial distances smaller than the radius of Vela Junior a clear excess over the background is visible. Even in this representation the thin shell can be seen.

The number of events being reconstructed within a circle with radius 1 deg around the source position (RA $8^{\mathrm{h}}52.0^{\mathrm{s}}$ Dec $-46°22'$) is 19697. The number of background events is derived with the ON-OFF Background method. In is 14259. The normalization factor between the source and background counts is 0.987017. This factor takes into account different exposure times for the source and background observations. From these values the excess and its significance are calculated. The excess is 5623 with a significance of 30.8 standard deviations.

To check the result for systematic uncertainties the analysis is performed with standard cuts. The number of source and background events is then 129054

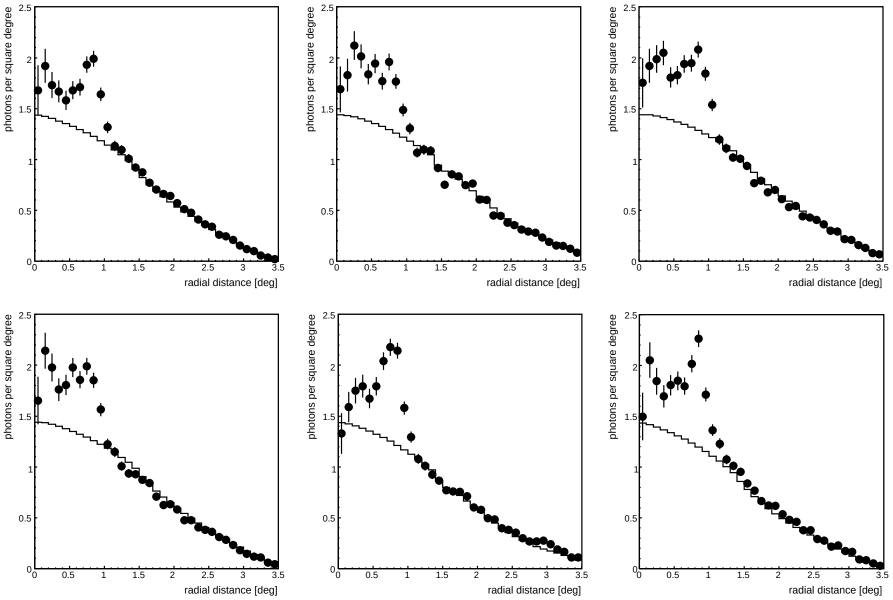

Figure 6.2: Comparison of the radial profile of the event map (circles) with the radial profile of the background map (histogram). The different figures correspond to radial profiles in the regions shown in Figure 6.7.

and 120308, respectively, with a normalization of 0.982403. The excess is therefore 10863 with a statistical significance of 21.9. The lower significance for the gamma-ray excess can be explained by the poorer gamma-ray/hadron separation for a lower size cut.
The results derived with the Reflected Background method using only the runs for which the pointing was outside of Vela Junior are comparable with the results above.

6.2.2 Width of the shell

To get an estimate of the geometry of the shell a simple toy model is fitted to the radial profile. In the toy model it is assumed that all emission is coming from a shell with a width w. Therefore the emission from a certain direction is proportional to the length of the part of the line of sight in the shell. In the left panel of Figure 6.3 the toy model is shown. To calculate the radial profile of the toy model the length of the shell in the line of sight is calculated. The length of the line of sight in a sphere can be expressed as $x = r_i \cdot \sin(\alpha_i)$, where r_i is the radius of the sphere and α_i is the angle shown in the right panel of Figure 6.3. The length of a shell in the line of sight is then

$$x = r_{\text{out}} \cdot \sin(\alpha_{\text{out}}) - r_{\text{in}} \cdot \sin(\alpha_{\text{in}}), \tag{6.1}$$

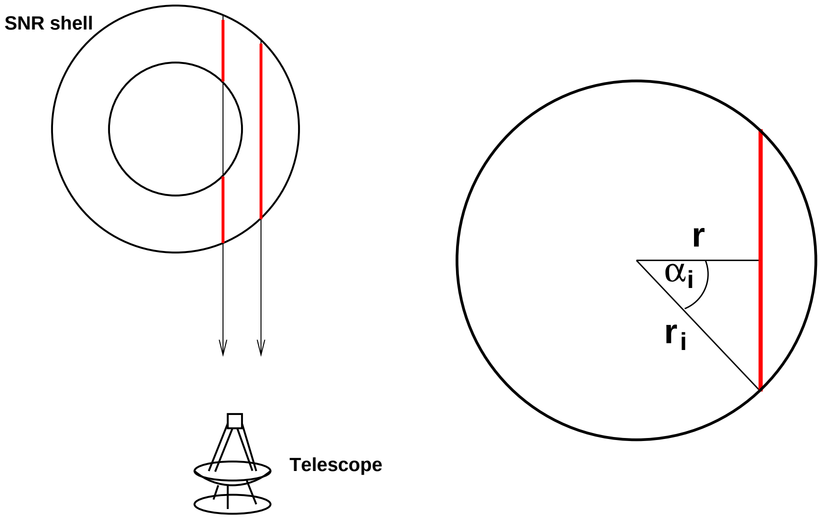

FIGURE 6.3: *Left*: Toy model of an emitting shell. *Right*: Parameters to express the length of the line of sight within the shell

where r_{out} and r_{in} are the outer and the inner radius of the shell and α_i is the corresponding angle. This can be expressed in terms of the radial distance to the center, the radius r_{out} and the width w of the shell

$$x = r_{\text{out}} \cdot \sin\left(\arccos\left(\frac{r}{r_{\text{out}}}\right)\right) - (r_{\text{out}} - w) \cdot \sin\left(\arccos\left(\frac{r}{r_{\text{out}} - w}\right)\right) \tag{6.2}$$

The parameter r is the radial distance of the line of sight to the center of the sphere. To account for the the binning of the radial profile this function is multiplied at every point with a Gaussian with a standard deviation of 0.1 deg. The toy model is fitted to the radial profile of the remnant. The result can be seen in Figure 6.4. The values obtained by the fit are $r_{\text{out}} = (0.991 \pm 0.005)$ deg and $w = (0.180 \pm 0.001)$ deg. Therefore the shell observed by H.E.S.S. is very thin. It is only 18.2% of the radius also obtained by the fit. In an other shell-type SNR resolved by H.E.S.S., Vela Junior, the width is $\sim$ 45% of the shell radius.

6.3 Spectral Analysis

In the analysis of a point source the gamma-ray/hadron separation is improved by restricting the events to be analyzed to a small region around the source. This size of the region is chosen to be the same as that of the point spread function of the system. For extended sources this selection can not be done.

In addition extended sources are often observed with greater wobble offsets to make use of the Reflected Background method, for which the pointing of the observation has to be outside of the source. For these two characteristics (worse gamma-ray/hadron separation and large offset) the energy resolution is slightly worse, $\Delta E/E \sim 25\%$.

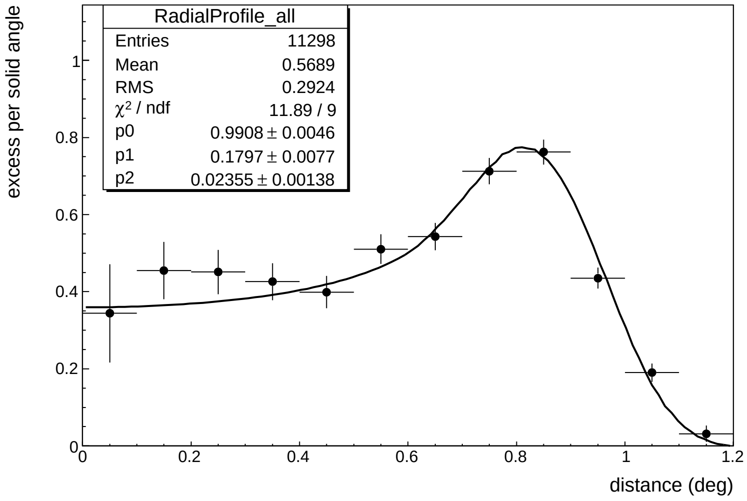

FIGURE 6.4: Radial profile of Vela Junior with a fit obtained by a toy model.

The spectral analysis is done using hard cuts as they provide a better gamma-ray/hadron separation. For comparison the spectra are also derived with standard cuts.

All events reconstructed within 1 deg around Vela Junior are taken as source events, in the following called ON events. The background estimation is done using the ON-OFF Background method.

The derived differential energy spectrum is shown in Figure 6.5. The spectrum is fitted with a power law. The spectral index derived by the fit is $\Gamma = -2.40 \pm 0.03_{\text{stat}} \pm 0.09_{\text{sys}}$. The normalization is $I_0 = (3.3 \pm 0.1_{\text{stat}} \pm 0.7_{\text{sys}}) \times$

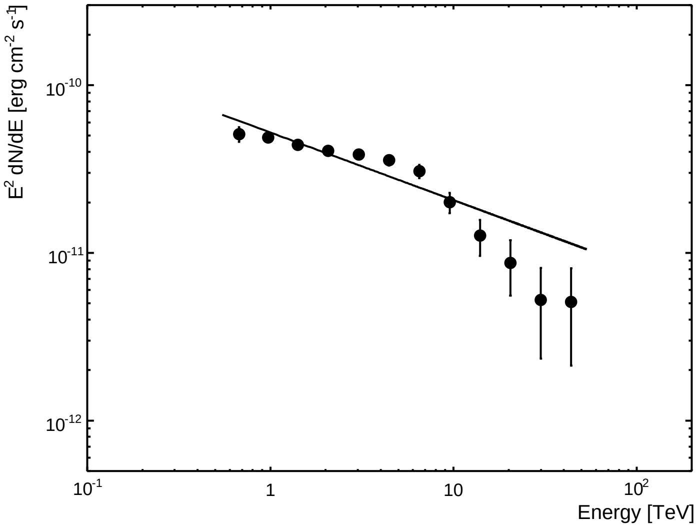

FIGURE 6.5: Differential spectrum of Vela Junior fitted with a power-law.

$10^{-11}\,\mathrm{cm}^{-2}\,\mathrm{s}^{-1}\,\mathrm{TeV}^{-1}$. The χ^2 test gives $\chi^2/\mathrm{d.o.f.} = 44.3/10$. The measured spectrum deviates from the fitted power law at energies above 20 TeV.

To account for the deviation at higher energies a power law with an exponential cutoff

$$dN/dE = I_0 \left(\frac{E}{E_0}\right)^{-\Gamma} \exp\left(\frac{E}{E_{\mathrm{cut}}}\right) \tag{6.3}$$

is fitted to the data. The result is shown in Figure 6.6. The power-law with an

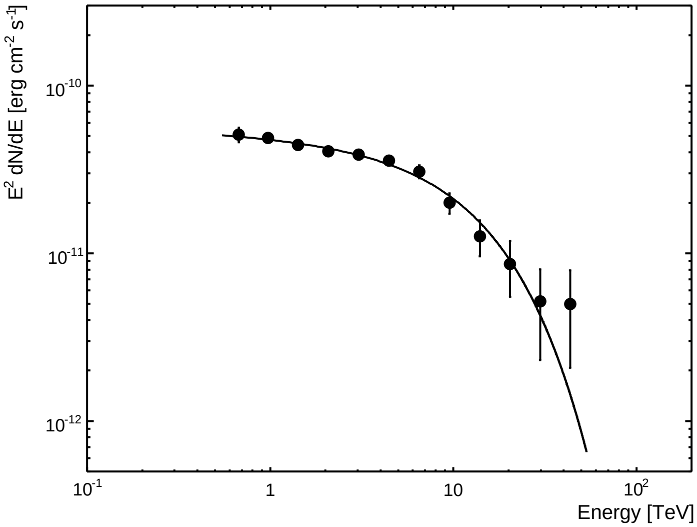

FIGURE 6.6: Differential spectrum of Vela Junior fitted with a power-law with an exponential cutoff.

exponential cutoff is a good fit to the data. The fitted function has an index of $\Gamma = 2.05 \pm 0.07_{\mathrm{stat}} \pm 0.09_{\mathrm{sys}}$ and a normalization at 1 TeV of $I_0 = (3.2 \pm 0.1_{\mathrm{stat}} \pm 0.6_{\mathrm{sys}}) \times 10^{-11}\,\mathrm{cm}^{-2}\mathrm{s}^{-1}\mathrm{TeV}^{-1}$. The cutoff is at $(12.8 \pm 3.1_{\mathrm{stat}} \pm 3.2_{\mathrm{sys}})$ TeV.

In Table 6.1 the results of the different fits to the spectra, derived with standard and hard cuts are summarized. If one takes into account the systematic errors of

Fit	Cuts	$I_0(\mathrm{cm}^{-2}\mathrm{s}^{-1}\mathrm{TeV}^{-1})$	Γ	E_{cut}(TeV)	χ^2/d.o.f.
power	hard	$(3.3 \pm 0.1) \times 10^{-11}$	2.40 ± 0.03		44/10
cutoff	hard	$(3.2 \pm 0.1) \times 10^{-11}$	2.05 ± 0.07	12.8 ± 3.1	5/9
power	std	$(3.6 \pm 0.1) \times 10^{-11}$	2.40 ± 0.02		30/11
cutoff	std	$(3.8 \pm 0.1) \times 10^{-11}$	2.30 ± 0.04	34.2 ± 14.1	21/10

TABLE 6.1: Spectral parameters derived with fits of a power-law ("power") and a power-law with exponential cutoff ("cutoff") and different image cuts

$\sim 20\%$ on the flux and 0.09 on the index, the results derived with standard cuts are comparable with those with hard cuts. The power-law with an exponential cutoff fits the data better than a pure power-law.

6.4 Comparison with X-rays

The morphology of Vela Junior obtained with H.E.S.S. is compared to measurements in X-rays performed with the ASCA satellite. ASCA observed Vela Junior with seven distinct pointing (Tsunemi et al., 2000). The observations covered most of the remnant except for the bright region in the south seen in the ROSAT All Sky Survey data. In Figure 6.7 the excess sky map measured by ASCA is shown with contours of the H.E.S.S. excess overlayed. The brightest regions in the excess from gamma rays coincide roughly with the brightest regions in the X-ray wavelength. To compare the emission in gamma rays with that in X-rays radial profiles from the center of the remnant to a radial distance of 1.2 deg are generated in 6 regions. The regions are indicated in Figure 6.7. The binning of the radius is chosen to be 0.1 deg. This value is larger that the angular resolution of both H.E.S.S. and ASCA. Therefore in the resulting radial profiles effects due to the angular resolution are negligible. The radial profiles are plotted in Figure 6.8. The ASCA observations do not cover the whole remnant. Therefore the profiles derived from the regions 2,3 and 4 can only be compared up to ~ 0.7 deg. The radial profiles of both experiments are in good agreement. In the regions 1, 2 and 3 enhanced X-ray emission closed to the center is found. In region 5 an indication of a slight shift between the gamma-ray emitting shell and the X-ray emitting shell can be seen. Unfortunately, because of the incomplete coverage of the ASCA measurement a more quantitative comparison cannot be done.

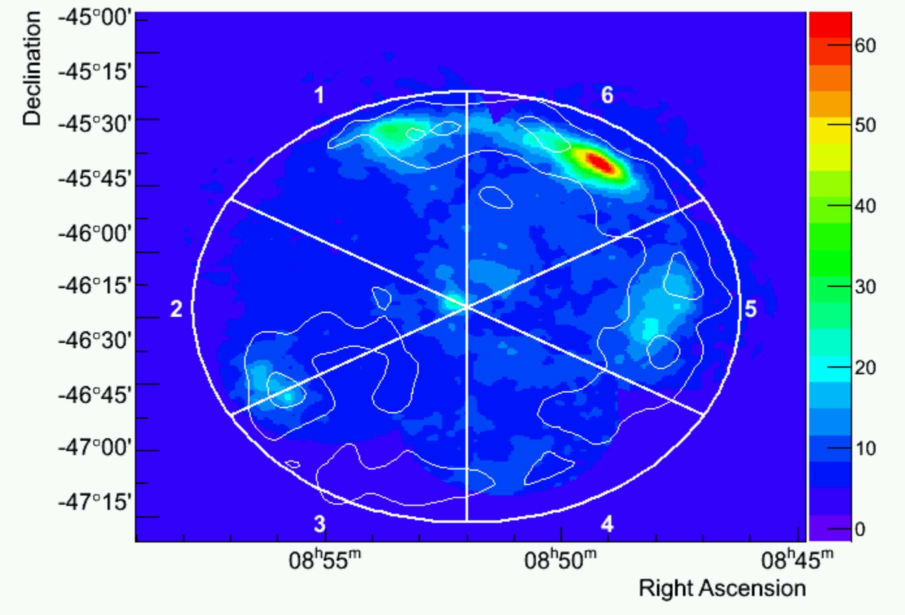

FIGURE 6.7: X-ray excess counts from the region of Vela Junior with gamma-ray contours from H.E.S.S. overlayed. The drawn regions are the regions in which the radial profiles of the gamma rays are compared to that of the X-rays.

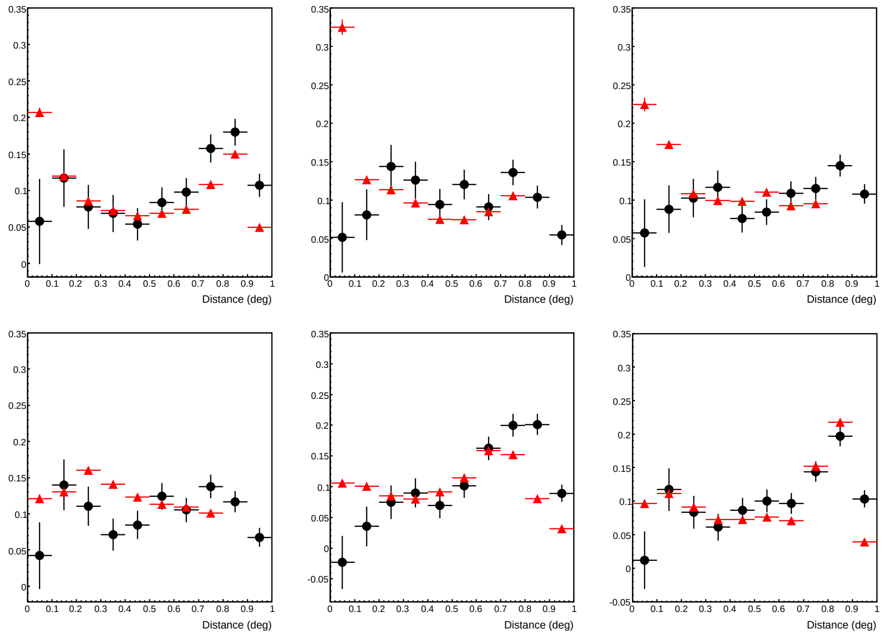

FIGURE 6.8: Comparison of the radial profiles in gamma rays and X-rays.

6.5 Energy in Accelerated Protons

In this section the energy in accelerated protons in a pure hadronic scenario is derived. The discussion here follows the same arguments presented in Section 5.3.1. Assuming that all gamma-ray emission is originated in protons interacting with the ambient matter the total energy in accelerated protons can be calculated from the energy flux in VHE gamma rays. The energy flux in the range covered by H.E.S.S. is calculated using the fitted power law with an exponential cutoff. The spectrum is described by

$$\begin{aligned} F(E) = (3.8 \pm 0.1_{\mathrm{stat}} \pm 0.9_{\mathrm{sys}}) \quad & \times \quad 10^{-11}\,\mathrm{cm}^{-2}\,\mathrm{s}^{-1}\,\mathrm{TeV}^{-1} \\ & \times \quad \left(\frac{E}{1\,\mathrm{TeV}}\right)^{-2.3\pm0.04_{\mathrm{stat}}\pm0.2_{\mathrm{sys}}} \\ & \times \quad \exp\left(\frac{E}{(34.2 \pm 14.13)\,\mathrm{TeV}}\right) \end{aligned} \tag{6.4}$$

Therefore the energy flux in the range $(0.5 - 20)$ TeV is

$$F_E = \int_{0.5\,\mathrm{TeV}}^{20\,\mathrm{TeV}} E\,F(E)\,dE = (9.4^{+0.8}_{-1.0}) \times 10^{-11}\,\mathrm{erg}\,\mathrm{cm}^{-2}\,\mathrm{s}^{-1}. \tag{6.5}$$

For a distance d to the source the gamma-ray luminosity becomes $L_\gamma = (1.1 \pm 0.1) \times 10^{34}\,\mathrm{erg}\,\mathrm{s}^{-1}\,(d/1\,\mathrm{kpc})^2$. The total energy in accelerated protons with energies corresponding to gamma-ray energies measured by H.E.S.S. is then given by $W_\mathrm{p} = L_\gamma \tau_{\mathrm{pp}\to\pi^0}$, where $\tau_{\mathrm{pp}\to\pi^0}$ is the average cooling time of protons through the π^0-production channel (see Section 2.5.1). With the obtained luminosity the total energy in protons becomes $W_\mathrm{p} \sim (5.7 \pm 0.6) \times$

$10^{49}\,\mathrm{erg}\,(d/1\,\mathrm{kpc})^2\,(n/1\,\mathrm{cm}^{-3})^{-1}$.

The energy range covered by H.E.S.S. corresponds to an energy range of the accelerated protons of $(2.9 - 118)\,\mathrm{TeV}$. Assuming a total energy range for the accelerated protons of $1\,\mathrm{GeV} - 3\,\mathrm{PeV}$ and an index for the proton spectrum of -2.3 (like the spectral index of the gamma rays) the energy flux measured by H.E.S.S. corresponds to 8% of the total expected energy flux in accelerated protons. Therefore the total energy in accelerated protons of Vela Junior is

$$W_p \sim (7.1 \pm 0.8) \times 10^{50}\,\mathrm{erg}\,(d/1\mathrm{kpc})^2\,(n/1\mathrm{cm}^{-3})^{-1}. \tag{6.6}$$

For a distance of $d = 200\,\mathrm{pc}$ and a density comparable to the average density of the interstellar medium, $n = 1\,\mathrm{cm}^{-3}$, the total energy in accelerated protons becomes

$$W_p \sim 2.9 \times 10^{49}\,\mathrm{erg}. \tag{6.7}$$

In the case of a type Ia SN the explosion energy is supposed to be about 10^{51} erg. Therefore, if Vela Junior was the remnant of a nearby type Ia SN, the energy in accelerated protons would be on the order of $\sim 3\%$, a value which is in the range of what is expected from SNe.

However, Slane et al. (2001) give an upper limit on the density of the ambient medium of $n < 2.9 \times 10^{-2}(d/1\,\mathrm{kpc})^{-1/2} f^{-1/2}\,\mathrm{cm}^{-3}$, using the assumption of thermal equilibrium. The quantity f is the filling factor of a sphere taken as the emitting volume in the region chosen. The combination of this density upper limit with 6.6 results in a lower limit for total energy in accelerated protons of

$$W_p > 4.5 \times 10^{50}\,\mathrm{erg}, \tag{6.8}$$

assuming a filling factor of $f = 1$ and a distance of $200\,\mathrm{pc}$.

In both types, either thermonuclear or core collapse SN, the energy which is in principle available for the acceleration of particles is $\sim 10^{51}$ erg. In the core collapse SN 99% of the $\sim 10^{53}$ erg explosion energy is deposited in neutrinos. Therefore the total energy in accelerated protons derived by assuming a pure hadronic scenario for the flux measured by H.E.S.S. is $\sim 45\%$ of the available kinetic energy of the explosion. Dorfi (2000) claimed a maximum of 24% for a density $n = 10\,\mathrm{cm}^{-3}$. Densities below this value would result in a smaller fraction in accelerated protons.

The H.E.S.S. lower limit for the total energy in accelerated protons in Vela Junior is twice the maximum estimated from theory and half the total kinetic energy of the explosion. Therefore, the pure hadronic scenario is very unlikely even for a distance of $d = 200\,\mathrm{pc}$.

Chapter 7

SN1006

The “new star” of 1006 was the first potential SN to be recorded in Europe and the Arab dominions (Stephenson and Green, 2002). The records, also coming from Japan and China, indicate that it has been extremely bright and has been visible for several years.

Based on a historical Arabic text Goldstein (1965) was the first who suggested that this new star could have been a SN. Gardner and Milne (1965) searched for if in radio catalogues in a region where Marsden (1965) suggested it could be found. In the search Gardner and Milne (1965) found a radio source at the coordinates RA $14^{\mathrm{h}}59.6^{\mathrm{m}}$, Dec $-41°42'$ (J1950.0). The authors performed a survey at a wavelength of 11 cm with a 210-ft telescope of the region around the source and found a structure which “closely resemble the typical structure of many known supernova remnants.

Later, SN1006 was the first SNR for which evidence for non-thermal X-ray emission was reported (Becker et al., 1980a). Reynolds and Chevalier (1981) explained the spectrum as the extension of the radio synchrotron emission, steepened by synchrotron losses. Observations by ASCA (Koyama et al., 1995) with a pointing each on the center and on the north-eastern part of the rim showed that the spectrum in the rim to be featureless and well described by a power-law, whereas in the center it is dominated by line emission. The authors infer from the highest energies in the non-thermal spectrum that electrons with energies ≥ 200 TeV are accelerated in SN1006. Electrons with such energies can produce TeV gamma rays by inverse Compton scattering of CMB photons. This makes SN1006 a potential emitter of VHE gamma rays. A detection of TeV gamma rays was reported by the CANGAROO collaboration (Tanimori et al., 1998) and confirmed by observations with the CANGAROO-II detector. However, the more sensitive H.E.S.S. telescope array did not detect any VHE gamma-ray emission from SN1006 in observations in 2003 and 2004 (Aharonian et al., 2005), the upper limit on the flux being a factor 10 below the flux measured by CANGAROO. Observations with the CANGAROO-III array consisting of four 10 m atmospheric Cherenkov telescopes showed no excess in VHE gamma rays from SN1006 (Tanimori and et al., 2005).

In 2006 and 2007 H.E.S.S. took another 48 hrs observation on SN1006. In this chapter the analysis of the data from 2003 and 2004 together with 30 hrs from the new data is presented. It is shown that with this data set H.E.S.S. find a significant excess of VHE gamma-ray emission.

7.1 H.E.S.S. Observations and Analysis

The data on the SNR SN1006 were taken in 2003 with two telescopes and between May 2004 and May 2007 with four telescopes for a total observation time of 66 hrs. The data set which is analyzed here has 30 hrs more observation time than that presented in Aharonian et al. (2005). The observation was performed in wobble mode with offsets between 0.17 deg and 0.75 deg in Right Ascension and Declination, respectively, around the center of SN1006 (RA $15^h02^m48.4^s$ Dec $-41°54'42''$ J2000). During observation the zenith angle ranged from 18 deg to 46 deg with a mean of 24 deg. After applying the H.E.S.S. standard quality selection (see Section 4.1) a total live time of 56 hrs of data were available for analysis. The data were calibrated as described in Section 4.2. The images were cleaned with the standard image cleaning procedure.

The analysis is performed using hard cuts. For the flux determination, all events reconstructed within 0.25 deg around the center of SN1006 are assumed to be gamma rays originating in SN1006 or background gamma-ray-like particles. The sky maps are produced with the Ring Background method. The spectral analysis is performed with the Reflected Background method.

7.2 Results

7.2.1 The whole Remnant

Figure 7.1 shows the excess map around the position of SN1006 with overlayed contours from ASCA measurements (Dyer et al., 2004). The gamma-ray excess measured by H.E.S.S. coincides with the X-ray emission measured by ASCA. However the extent of the gamma-ray emission is larger.

The total number of gamma-ray events from the test region (0.25 deg around the center of SN1006) is 1330 while 7116 gamma-ray-like events are recorded in the background regions. The normalization is 0.173469. This results in an gamma-ray excess from SN1006 of 96 ± 35 with a significance of 2.5 standard deviations.

The top panel of Figure 7.2 shows the significance sky map for gamma rays above the estimated background obtained with the Ring Background method. A spot of enhanced significance can be seen at the edge of the north-eastern part of the remnant. The maximal significance in this spot reaches more than 5.7 standard deviations. For the generation of the map an oversampling radius of 0.1 deg is used.

The bottom panel of Figure 7.2 shows the the development of the significance with time for a gamma-ray excess from the whole remnant. The significance is calculated using the formula from Li and Ma (1983). From the formula it is expected that the significance rises with time like $\sqrt{t}$. At the beginning of the observation the significance stays well below zero. Compared to the expected

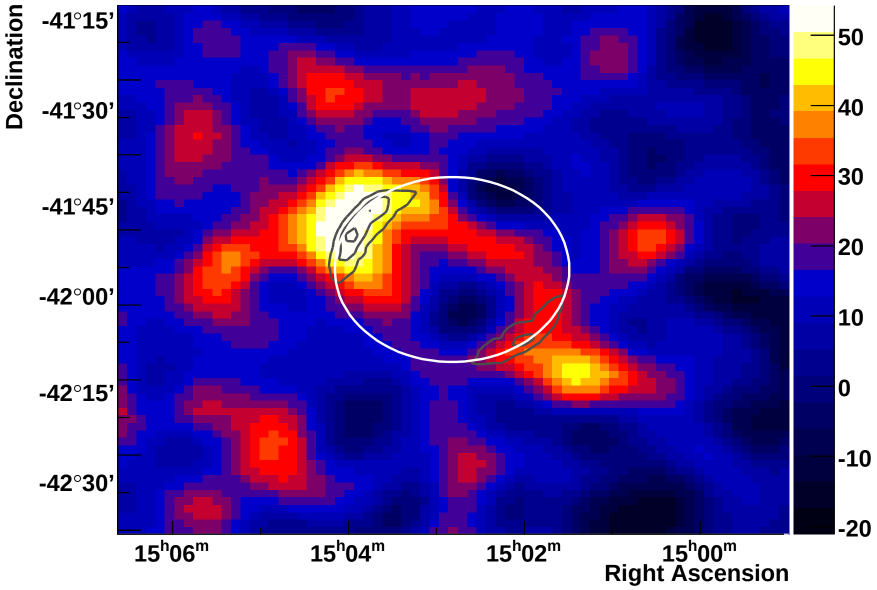

FIGURE 7.1: Excess sky map around SN1006 with ASCA contours overlayed (Dyer et al., 2004). The H.E.S.S. excess sky map is smoothed with a Gaussian with a standard deviation of 0.06 deg to account for the resolution of the H.E.S.S. measurements. The white circle denotes the position and the size of SN1006.

behavior, $f(t) = p_0\sqrt{t}$, it seems to be shifted to lower values over the whole time range. A fit of a function $f(t) = p_0\sqrt{t} + p_1$ gives a shift of $p_1 = -2.9$ standard deviations. This can be explained by contamination of the background by a gamma-ray source.

7.2.2 Analysis on the north-eastern Spot

In the significance sky maps a significant excess from a small region in the north-eastern part of the remnant can be seen. Figure 7.3 shows a slice through the north-eastern spot and the center of SN1006. The enhanced excess can be clearly seen in the right panel on the figure between −0.4 deg and −0.2 deg from the center of SN1006. Therefore the analysis is repeated on the north-eastern spot in a region centered on RA $15^{\mathrm{h}}03^{\mathrm{m}}5.28^{\mathrm{s}}$ Dec $-41°47.4'$ with a radius of 0.14 deg. The region which is used in the analysis is shown as a dashed black circle in Figure 7.4.

In Figure 7.5 the significance distribution outside of the spot region (red) is compared to the significance distribution in the whole field of view (black). The background distribution is best fitted by a Gaussian with a standard deviation of 1.084 ± 0.003 and a mean of -0.006 ± 0.004. Due to oversampling of the significance map (with an oversampling radius of 0.1 deg) the bins in the significance map are highly correlated. The errors on the fit parameters should be higher. It is concluded here that the significance distribution outside of the

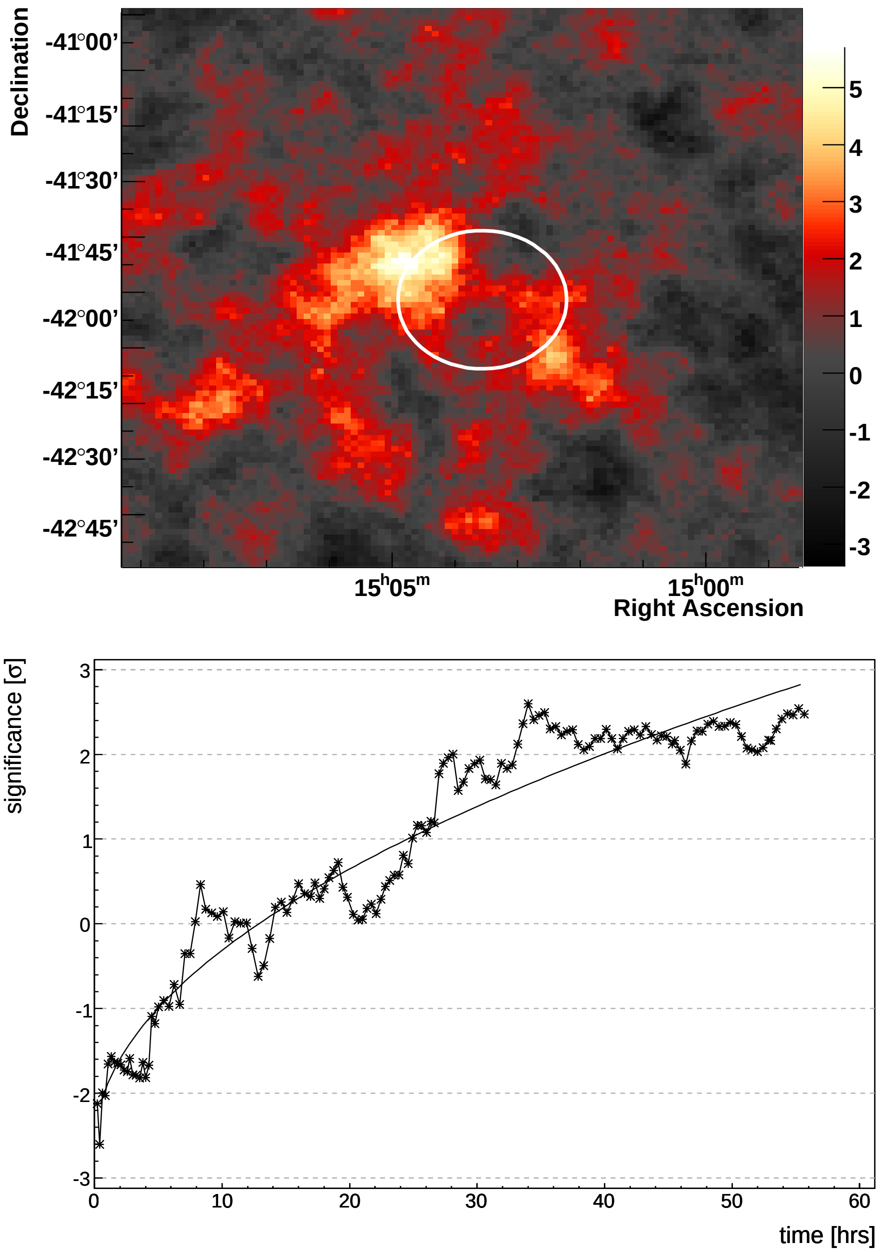

FIGURE 7.2: *Top:* Significance sky map showing in each bin the significance for an excess in this bin. An oversampling radius of 0.1 deg is used for the generation of the map. The white circle denotes the position and size of SN1006 in X-rays. *Bottom:* Significance for gamma-rays from the whole remnant versus time. The line is a fit of $f(t) = p_0\sqrt{t} + p_1$ to the data points.

test region is compatible with statistical fluctuations. Furthermore, from the excess of the black curve it can be seen that almost the whole gamma-ray excess comes from the test region.

Figure 7.6 shows the development of the significance in the spot region as a func-

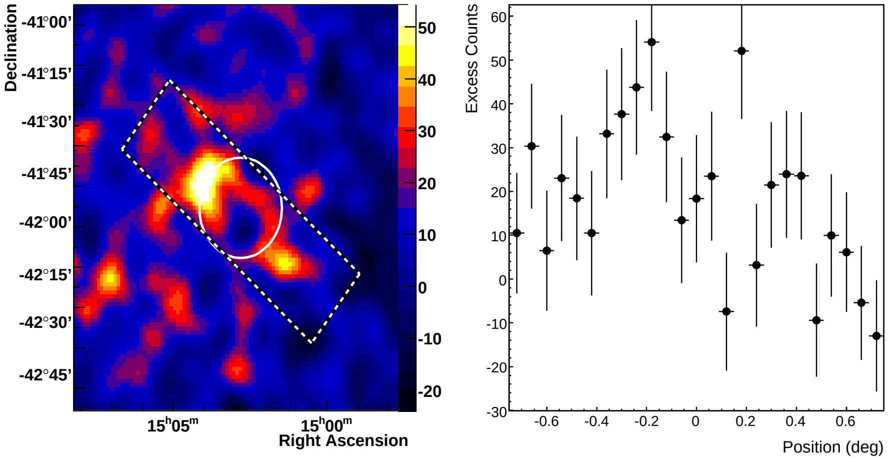

FIGURE 7.3: Excess in a slice through the north-eastern spot and the center of SN1006

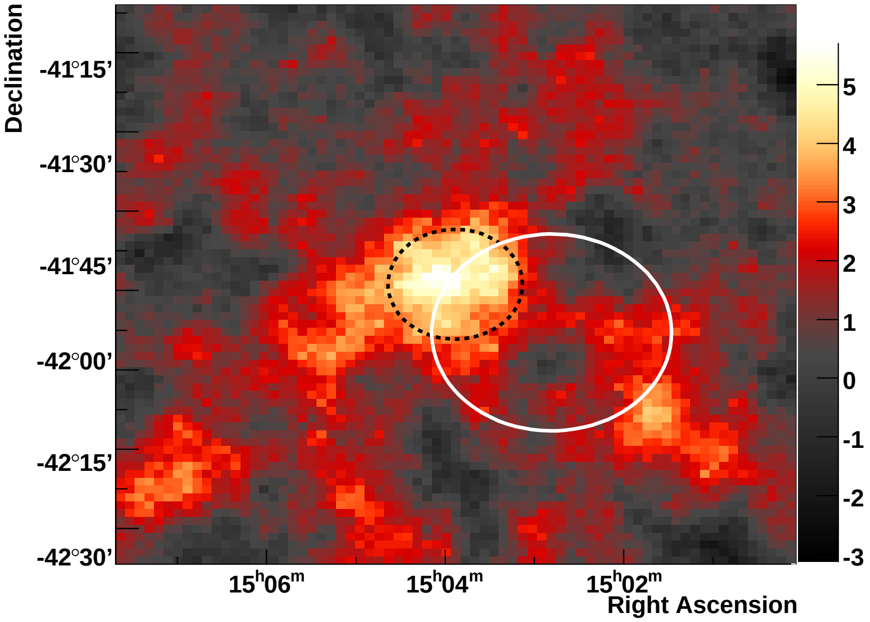

FIGURE 7.4: Significance map with the region used for the analysis of the emission spot.

tion of the live time. The significance scales roughly with the square root of time. A fit of the function $f(t) = p_0\sqrt{t}$ to the data reveals $p_0 = 0.47\,\mathrm{h}^{-1/2}$. 479 ON and 3256 background events are counted with a normalization of 0.11418. This results in an excess of 107 ± 23 and a significance of 5.0.

There are 45 more runs (a run is an observation period of approximately 28 min)

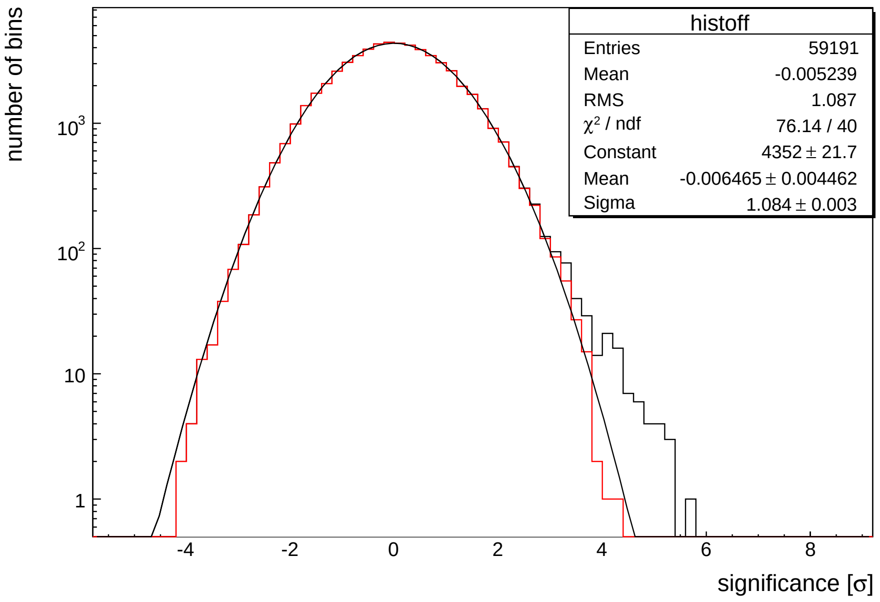

FIGURE 7.5: Significance distribution outside of the test region (red) compared to the distribution in the whole field of view. A fit of a Gaussian to the red histogram is also shown.

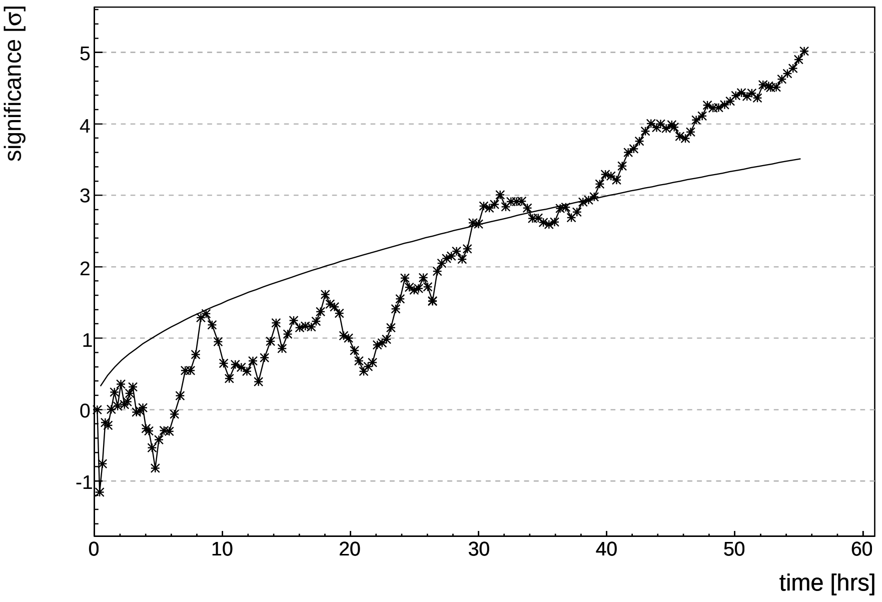

FIGURE 7.6: Significance versus time for the spot region. The line is a fit of $f(t) = p_0\sqrt{t}$.

taken of SN1006 which could not be included into this analysis as the calibration of the data is not finished at the time of writing of this work. From the results presented here the analysis of the whole data set is expected to definitely reveal SN1006 as a source of VHE gamma rays.

7.2.3 Spectral Analysis

On the north-eastern spot a spectral analysis is performed. The background is estimated using the Reflected Background method. The obtained spectrum is shown in Figure 7.7. The spectrum is well fitted by a power-law $dN/dE = I_0(E/1\,\mathrm{TeV})^{-\Gamma}$ with an index of $\Gamma = 1.98 \pm 0.17_{\mathrm{stat}} \pm 0.2_{\mathrm{sys}}$ and a normalization of $I_0 = (1.8 \pm 0.5_{\mathrm{stat}} \pm 0.3_{\mathrm{sys}}) \times 10^{-13}\,\mathrm{cm}^{-2}\,\mathrm{s}^{-1}\,\mathrm{TeV}^{-1}$. The χ^2-test gives $\chi^2/\mathrm{d.o.f.} = 1.4/2$. The integrated flux above 1 TeV is $(1.9 \pm 0.6_{\mathrm{stat}} \pm 0.3) \times 10^{-13}\,\mathrm{cm}^{-2}\,\mathrm{s}^{-1}$.

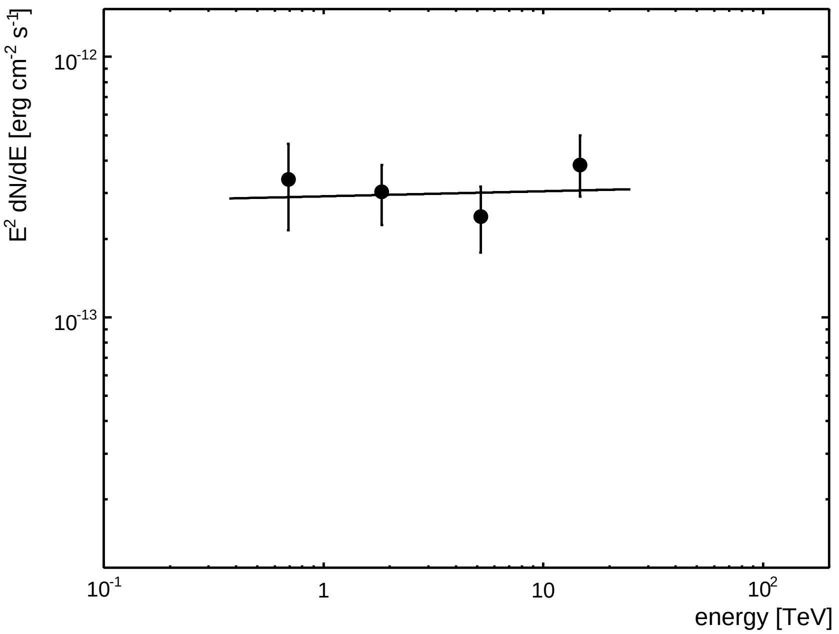

FIGURE 7.7: Spectrum from the north-eastern spot of SN1006 with the fit of a power-law.

7.2.4 Comparison with the CANGAROO result

From the fit the integrated spectrum $F(>E) = \frac{I_0 \cdot 1\,\mathrm{TeV}}{\Gamma - 1} E^{-\Gamma+1}$ is calculated to compare it with the integrated flux reported by CANGAROO. The comparison is shown in the Figure 7.8. In addition the upper limits derived by H.E.S.S. from the data taken in 2003 and 2004 are drawn at the energies of the CANGAROO measurements. The integrated photon flux from the analysis of the whole data set is compatible with the H.E.S.S. upper limit derived in 2004. However, it is more that 50 times below the integrated photons flux reported by CANGAROO from 1998.

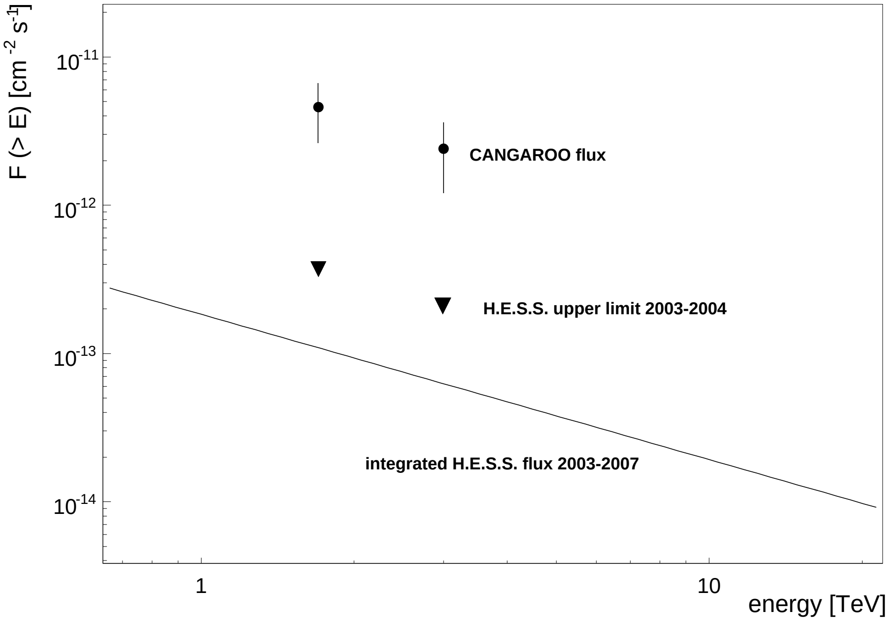

Figure 7.8: Comparison of the integrated energy flux derived from the fit (line) with the integrated flux reported by CANGAROO and the upper limits derived by H.E.S.S. in 2003 and 2004.

Part III

Smart Pixel Camera

Chapter 8

Components of the Smart Pixel Camera

The success the current generation IACTs experiments and mainly of H.E.S.S. was a breakthrough for ground-based gamma-ray astronomy. For the next generation of instruments, the technical aims are to improve the sensitivity in the current energy range by about an order of magnitude, and to increase the accessible energy range into the some 10 GeV range and to about 100 TeV. At the same time the field of view should be enlarged to $6-8\,\mathrm{deg}$. These aims, might be achieved with a mixture of telescopes, a few large telescopes with $O(500\,\mathrm{m}^2)$ mirror area and many (some 10) small and medium size telescopes. Due to the large number of telescopes with large field of view and due to the expected trigger rates, cameras will be needed that not only fulfill the technical and physics requirements, but that are also cost effective in production and operation.

The design of such a camera has been developed at the Max-Planck-Institute or nuclear physics (MPI-K), the so-called Smart Pixel Camera (SPC). A schematic overview of the SPC is shown in Figure 8.1. The main building block of such a camera are the Smart Pixels, which contain besides the photon detector and its supply, all analog electronics for signal integration, triggering, timing and monitoring, The signals from the pixels are provided as analog voltage levels. The pixels are plugged into a common backplane, via which the pixels are controlled and readout. The digitization of the pixel signals is done in a multiplexed mode using FADCs. The synchronization, control and readout of the whole camera electronics is performed by a single VME module, the *camera controller*. All core components of the SPC, like the pixel electronics, backplane, controllers have been developed at the MPI-K. Where possible, commercially available components have been used, like the FADCs, VME CPUs. In this chapter, the individual components and their characteristics are described. In the following chapter results about the performance of a camera prototype after system integration will be presented.

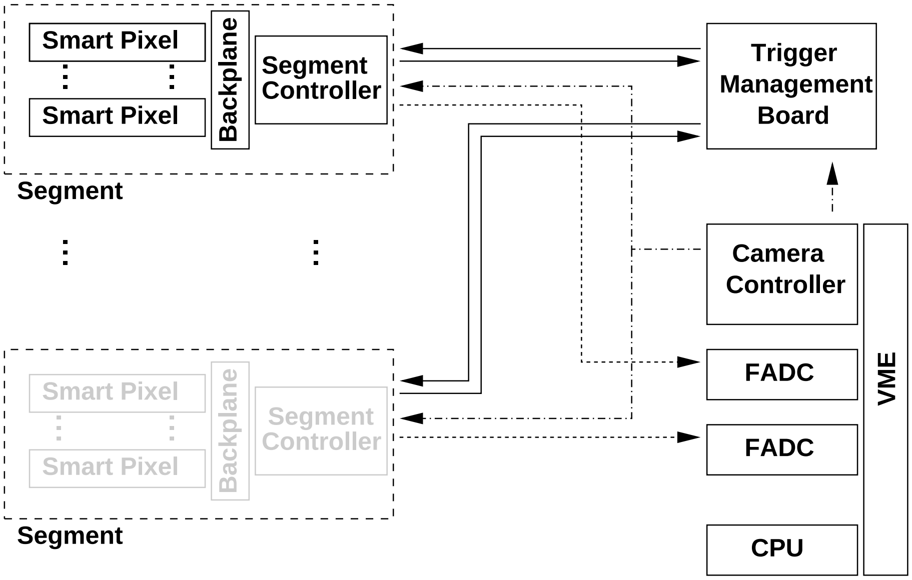
Smart Pixel
Smart Pixel
Backplane
Segment Controller
Segment
Trigger Management Board
Camera Controller
FADC
FADC
CPU
VME
Smart Pixel
Smart Pixel
Backplane
Segment Controller
Segment

FIGURE 8.1: Block diagram of the Smart Pixel camera

8.1 Smart Pixel

The main part of a SPC is the *Smart Pixel* (see Figure 8.2). It consists of a photomultiplier with its dedicated high voltage supply and the Smart Pixel electronics (SPE). These components are situated in a cylinder with 560 mm length and 36 mm diameter. The SPE is independ on the type of the photon detector. However, at the moment only photomultiplier tubes (PMTs) fulfill the main requirement of the atmospheric Cherenkov astronomy, which is the capability to process fast and faint signals (consisting of only few photons) at a good performance. Figure 8.3 shows a block diagram of the SPE. The SPE comprises the main functions of the Smart Pixel Camera, like the first two levels of the trigger logics, signal integration, time measurement, rate measurement and monitoring. In the following the main components of the SPE are described.

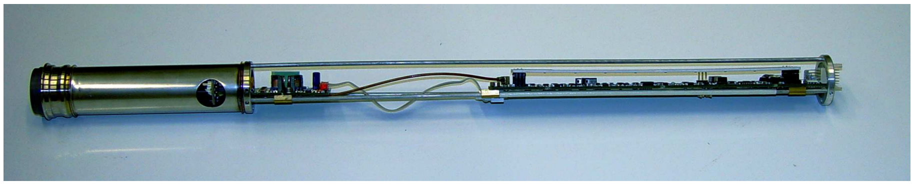

FIGURE 8.2: Smart Pixel, consisting of PMT, high voltage supply and Smart Pixel electronics

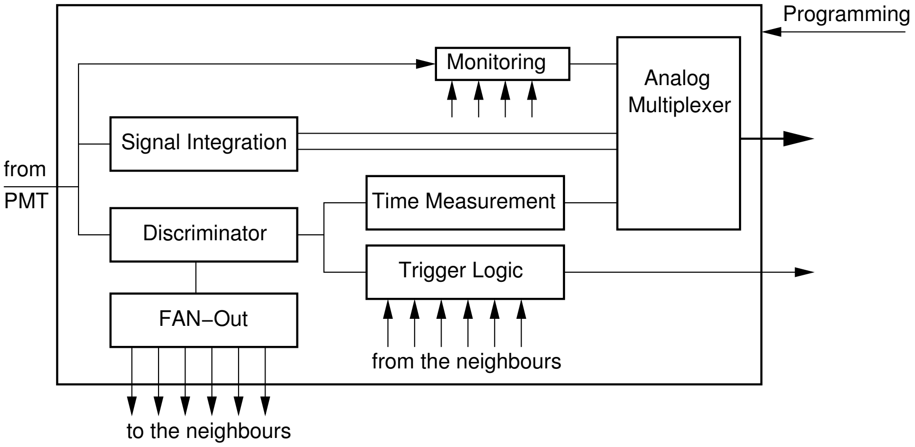

FIGURE 8.3: Block diagram of the main building blocks of the Smart Pixel electronics.

8.1.1 Trigger Logic

The main purpose of the trigger logics is to select gamma-ray events already on the hardware level while suppressing as many background events as possible. There are three main sources contributing to the background for Cherenkov telescopes on the trigger level. The first contribution is the NSB light, which is mainly light from photochemical processes of ions in the upper atmosphere, starlight and artificial light scattered in the atmosphere (Preuß et al., 2002). The second part is Cherenkov light from hadron-induced showers. The third source are muons, produced in air showers emitting Cherenkov light while passing near the telescope. The processing of NSB events is suppressed by triggering on compact images in the camera. As the photons from NSB arrive statistically distributed in time and space they can be distinguished from the short and spatially correlated images produced by Cherenkov light coming from air showers. This is used to implement the trigger for the telescope (see below). Hadron-induced and muon-induced events can not be suppressed by this procedure as their images in the camera are also short and spatial correlated. They have to be rejected in the analysis (see Section 4.4.3).

In the Smart Pixel Camera the trigger decision is made on the pixel. The signal coming from the PMT is split into three paths (see Figure 8.3). One (path) for the trigger generation, one for the determination of the signal amplitude and one for monitoring purposes. The signal in the trigger path is compared to a programmable threshold by a discriminator. The threshold can be set to values between ~ 0 photo electrons (p.e.) and $\sim 15\,$p.e. A photo electron is the resulting signal of an electron released at the cathode and amplified in the PMT.

If the amplitude of the signal exceeds the threshold a *discriminator signal* (a logic pulse of $4-6\,$ns duration) is generated and sent to a programmable logic device (PLD) on the pixel electronics and via the backplane (see Section 8.2) to all the direct neighbors of the pixel. The discriminator signal can be delayed up

to 5 ns in steps of 1 ns to correct for different signal propagation times through the PMT, depending on the high voltage applied. In the case that a required number (between 0 and 6) of external discriminator signals arrive at the PLD at the same time as the internal signal, a trigger signal is generated and sent to the trigger management board. The trigger implementation is a *Next Neighbor trigger* as the trigger decision is generated on every pixel using informations from the direct neighbors. The trigger management board distributes the trigger signal to all pixels in the camera. The maximal delay between two signals arriving at the PLD that they are still registered as being coincident is $4-6$ ns. The total time which is needed to generate and distribute the trigger signal is approximately 90 ns.
This implementation minimizes the number of combinatoric factors in comparison to a simple majority trigger, where N pixels out of M are required. It selects already on first level compact images which are expected from gamma-ray showers. Therefore the trigger decision is very fast ($\sim$ 20 ns). Another $\sim$ 70 ns are needed to distribute the trigger to the rest of the camera.

8.1.2 Signal Integration

The Cherenkov photons from a gamma-ray induced shower reach the camera within a short time window of the order of 10 ns. The PMT signal is amplified and integrated over typically $10-20$ ns to reduce the influence of background photons. The resulting value reveals the intensity in the pixel for a given event. In the following this value is called *amplitude*. In the analysis of the data the amplitude distribution in the camera is used to reject hadron-induced events, estimate the energy of the shower and reconstruct the direction where the VHE gamma-ray came from (in Chapter 4 an example of such an analysis is given).
As mentioned before, the signal from the camera trigger arrives at all pixels about 90 ns after the discriminator signals from the triggering pixels were generated. To buffer the signals until the trigger is distributed a delay line is implemented as a 12-layer printed circuit board (PCB). The PCB consists of a meandering electric line with ground lines and ground layers. The design aimed for a quasi-coaxial structure. The signal is then fed into a *gated integrator* to measure the charge content of the PMT pulse (see Figure 8.4). The camera trigger starts the gate for the integration. Its duration is programmable individually on each pixel from $10-25$ ns in steps of 3 ns. The *gate switch* is open for this duration. During that time the capacitor is loaded with a charge proportional to the charge content of the PMT pulse. This charge is stored on the capacitor until the *hold switch* is open and distributed as an analog voltage level via a *buffer amplifier* to the output of the gated integrator. The buffer amplifier has a high impedance to ensure that the capacitor is not discharged before the readout of the integrator. The start of the gate can be individually delayed on each pixel by up to 5 ns in single nanosecond-steps to fit the PMT pulse optimal into the gate. Displacements of the PMT signal with respect to the gate, due to jitter or a gradient in the arrival times of the signals result in a *phase error*. Figure 8.5 shows the influence of the phase error on the relative amplitude as measured for a gate width of 13 ns. For a displacement up to

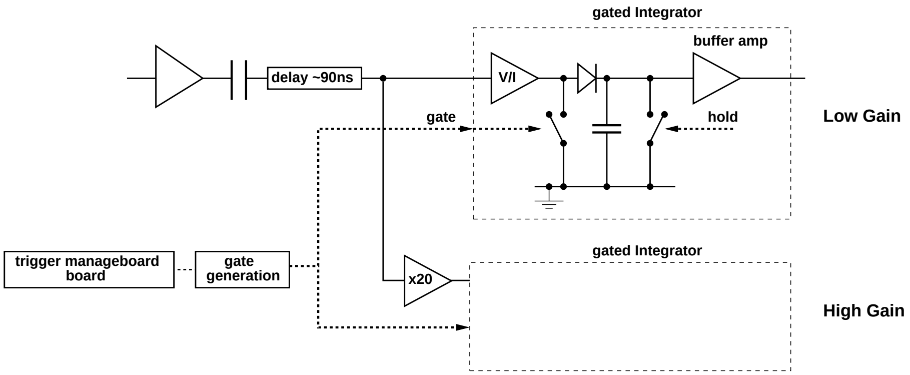
gated Integrator
buffer amp
delay ~90ns
V/I
gate
hold
Low Gain
trigger manageboard board
gate generation
x20
gated Integrator
High Gain

FIGURE 8.4: Diagram of the gated integrator; the high gain channel has a 20 times higher gain than the low gain channel.

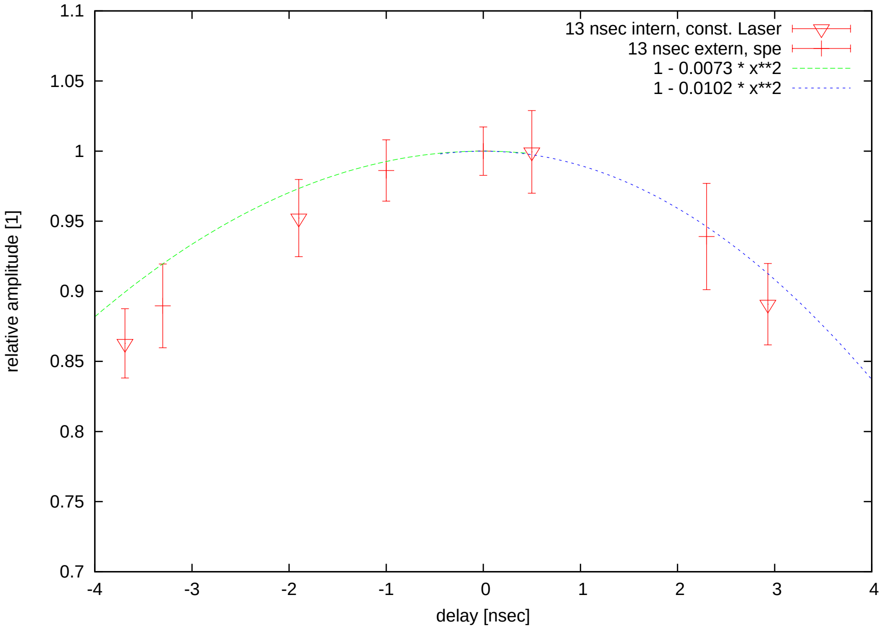

FIGURE 8.5: Influence of the phase error on the signal integration as a function of the relative delay between the PMT pulse and the gate. The curves are parameterizations of the data points.

2 ns the phase error is less than 4% of the amplitude. Therefore, even for a small gate width of 13 ns the phase error contributes only little to the error of the amplitude. The gate and the hold switch are implemented as open drain inverters. Some of the charge on the capacitor gets lost until it is read out. This *droop* is investigated in Hauser (2004). The droop is less than 1% after 10 μs for signals with amplitudes grater than 10 p.e. and has no influence on the signal determination as it also appears in the calibration. Before the voltage level at the output of the integrator can be digitized by an analog digital converter

(ADC) one has to wait at least $1\,\mu$s until the buffer amplifier has loaded (this can also be found in Hauser (2004)). Approximately the same time is needed to discharge the capacitor via the hold switch. In Section 9.5.4 is described how this contributes to the dead time for the read out.

Each pixel is equipped with two gated integrators. The corresponding channels in the readout are called *high gain* and *low gain*. The signal fed to the high gain channel is amplified by a factor of about 20 before it is integrated (see Figure 8.4) resulting in a increased resolution at lower amplitudes and, at the same time, a wide dynamic range. The dynamic ranges of the high and low gain are $\sim (0.2 - 150)$ p.e. and $\sim (4 - 3000)$ p.e., respectively.

8.1.3 Timing Information

Leptonic and hadronic showers show slight differences in their time profile (HEGRA Collaboration, 1999). Therefore the measurement of the arrival time of the Cherenkov photons in every pixel might help to improve the separation of gamma-ray and hadron-induced showers.

The timing information can also help to determine the signals which belong to the image of the Cherenkov shower and which are originated in NSB. This procedure is called image cleaning and in H.E.S.S. it is performed only with the use of amplitude information (Section 4.3).

In addition for large impact parameters a gradient in the arrival time is expected. Because of this gradient the gate for the integration of the PMT pulse is shifted with respect to its optimal position in some of the pixels, since there is one fixed trigger time for the whole camera. The arrival time of the pulse can be used to correct for a non-optimal position of the pulse in the integration gate. The gradient could also help to improve the angular resolution as it reveals additional information for the shower reconstruction about the shower development in the atmosphere.

The measurement of the arrival time is done using a time to amplitude converter (TAC), which is a capacitor with a constant current source (Figure 8.6). The loading of the capacitor is started with the camera trigger. The delayed (by 100 ns) discriminator signal stops the loading. Therefore the charge on the capacitor in proportional to the duration between the discriminator signal and the camera trigger. As the camera trigger arrives at every pixel at the same time this implementation allows to measure the time profile of a shower.

An advantage of this implementation is that it provides automatically the information whether a pixel had a signal above its discriminator threshold or not. Later it will be shown how this can be used to measure the value and shape of the threshold of every single pixel in normal operation mode (Section 9.5.1).

8.1.4 Anode Current Information

The NSB and the starlight are sources for noise in the images. The current at the anode of the PMT, called *PMI*, provides information about the intensity of this continuous background light. The PMI is proportional to the number of photons arriving at the PMT cathode per time. In addition the PMI reveals

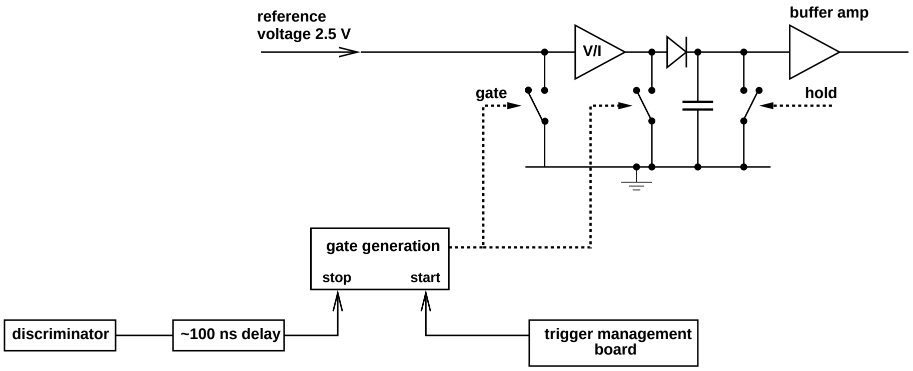

FIGURE 8.6: Circuit diagram of the TAC. The charge on the capacitor is proportional to the time between the camera trigger and the discriminator signal.

information of the position of faint[1] stars in the field of view. These positions can be used to correct for deviations in the pointing.
The PMI is measured by integrating the anode signal by an integrator with a time constant of $\sim 700\,\mu$s. The dynamic range is $0 - 16\,\mu$A.

8.1.5 Rate Measurement

The rate at which trigger signals are generated by a pixel is an important information about its performance. Pixels with much higher or much lower rates compared to the rest of the camera should be exchanged to ensure a homogeneous trigger efficiency.
Furthermore, as the NSB can produce camera triggers due to chance coincidences in neighboring pixels, the measurement of the rate at which the discriminator generates trigger signals helps to estimate the rate of these coincidences. Therefore a rate measurement is implemented on the Smart Pixel. For the input of the rate determination either the discriminator signal or the trigger signal from the PLD can be chosen. The rate measurement is implemented via an integrator with a defined pulse as input. For every event (either discriminator or PLD signal) a fixed pulse is integrated. Therefore the voltage level is proportional to the rate of signals at the input. The integration constant is of the order of half a second.

8.1.6 Temperature

During operation the pixel electronics consumes about 3 W power per pixel. The critical temperature for the modules and the circuits is estimated to be 60 degrees centigrade. In order to cool the electronics the prototype camera is equipped with twelve fans. Six in the front part to blow air into the camera and six in the rear part to exhaust the air again. To monitor the temperature in

---

[1] pixels which are illuminated by the image of bright stars have to be switched off in advance to protect the PMT

the camera every pixel is equipped with two temperature sensors in the vicinity of the temperature critical parts. It is planed to read out the temperature information once or twice times every second and to shut down the camera automatically in the case of the temperature exceeding a save threshold.
The temperature monitoring also helps to explore the efficiency of the cooling system, i.e. if each pixel is cooled enough. Furthermore, it allows to check for possible temperature dependent effects. So far, with the temperature variations in the lab, no temperature dependent effects, besides small baseline drifts within the expectations, are measured.
If unexpected temperature dependencies in the camera would occur, the information from the temperature sensors could be used to correct the measured data.

8.1.7 Further Monitoring

To ensure the reliability of the camera a good monitoring is needed. The actual values of the operating voltages, the high voltage and the current of the PMT and the status of the high voltage module can be read out. This information is very useful to identify pixel with malfunctions. In total there are 11 channels on each pixel for monitoring purposes.

8.1.8 Programmable Parameters on the Pixel

Table 8.1 shows the parameters which can be programmed on the pixel. The programming scheme is explained in Section 8.3. These parameters can be programmed individually on each pixel. This is important, for example, when a star is imaged into a pixel. Then the pixel is disabled from the trigger generation or switched off in the case of a bright star. Another example is the individual calibration of the high voltage of the HV converters to set a homogeneous gain in the camera.

parameter	range	main effect
discriminator threshold	(0 – 15) p.e.	trigger
multiplicity (next neighbors)	0 – 6	trigger
gate width	(10 – 25) ns	amplitude
high voltage (PMT)	(0 – 1600) V	PMT gain
rate input (discriminator or PLD)	–	rate
gate delay	(0 – 5) ns	amplitude
discriminator signal delay	(0 – 5) ns	trigger

TABLE 8.1: Programmable parameters on the pixel electronics

8.2 Segment

Sixteen pixels together with the *backplane* and the *segment controller* (see below) build a *segment*, which is the next lower level of modularity (after the pixel) of the Smart Pixel Camera (see Figure 8.1). The segment is a logical unit for the programming and the readout. The pixels are plugged into a backplane, which is a 12-layer circuit board with connectors to the pixel and the segment controller. All signals coming from or going to the pixel are distributed over the backplane. These are the commands for the programming, the readout of the event and monitoring informations and the discriminator signals needed for the generation of the Next Neighbor trigger. It is designed in a way that the signal propagation time for the discriminator signals to the neighboring pixels are identical, which is crucial for the first step of the trigger generation. In addition the signal propagation through the backplane is optimized for a good quality of the transmitted signals. The supply voltages for the pixels are also distributed via the backplane. One backplane segment supports 16 pixels. Neighboring backplanes are connected to each other by signal lines to facilitate trigger originating in inter-segmental coincident signals in neighboring pixels. The pixel are arranged in a hexagonal structure. Every pixel[2] is the middle of a hexagon and has therefore six direct neighbors.

The backplane is equipped with capacitors to isolate the pixels from each other electronically.

The transmission of signals from the segment to the trigger management board and the camera controller is done though the segment controller.

8.3 Camera Controller

The camera controller is the main controlling unit of the Smart Pixel camera. The main task of the camera controller is to synchronize the different parts of the camera. It provides all control signals like clocks and strobe signals. Furthermore the programming of the pixels and the trigger management board is done via the camera controller.

Programming

Every pixel has an unique address, which is composed of the absolute address of the segment controller and the position of the pixel on the segment. Via this address every pixel can be programmed individually. The programming of a pixel is done in two steps via a serial command bus. First a 16 Bit command (4 Bit data, 8 Bit address of the segment controller, 3 Bit segment command and one Bit for the broadcast mode (see below)) is send to the segment controller. In the programming of a pixel the first step is needed to select the pixel. In the second step again a 16 Bit (consisting of 8 Bit data, 3 Bit function and 5 Bit command) is sent to all pixels. The pixel which was selected in the first step additionally gets a strobe signal and computes the command. In the broadcast mode (i.e. the last bit is set in the first step) all pixels get the strobe signal and therefore all pixels compute the command. This method is very useful when all pixel should obtain the same command.

The transmission clock for the serial commands is programmable and normally

---

[2] except of pixels at the edge of the camera

operated at 10 MHz. Therefore the time needed for the programming is $\sim 2 - 3\,\mu$s/cmd.
A test of the reliability of the programming is described in Hauser (2004). During the test the programming of 10^6 commands showed not a single failed transmission. The programming is very reliable.

Readout and Digitization

The information obtained on the pixel, 3 channels for event data (High-gain, Low-gain, TAC) and 11 channels for monitoring, is provided as analog levels. These are multiplexed on one output line which is connected to another multiplexer on the segment controller where the signals from 16 pixels are multiplexed. In Figure 8.7 the scheme of the multiplexing is shown. The black channel is the active channel. The clock is provided by the camera controller with a frequency of 10 MHz. With every clock cycle the segment controller switches to the next pixel and the last readout pixel gets a strobe signal which causes the pixel multiplexer to switch to the next readout channel. The advantage of this scheme is that the pixel multiplexer do not need to be fast as the sampling rate of the pixel channels is 10/16 MHz. In the camera are 16 times more pixels than segment controller and therefore this scheme reduces the costs of the camera.
The digitization is performed by FADCs operated in multiplexing mode. They are equipped with two memory banks which are accessed asynchronous. This means that one of the banks is used to store the digitized data in a multi-event buffer, while the other one is accessed by the CPU to write the digitized data to a FIFO module. This procedure decouples the data taking and digitization from the reading of the digitized data into the storage. A discussion about the resulting regimes of dead time can be found in Section 9.5.4. In the SPC prototype the FADC modules are SIS3301 from Struck with a range of 14 Bits. With a dynamic range in the high gain channel of ~ 150 p.e. one p.e. corresponds to ~ 100 ADC-channels.
The digitization is properly synchronized with the switching of the multiplexer with a relative phase such that the analog levels have sufficiently saddled at the moment the digitization takes place.

8.4 Trigger Management Board

The trigger management board (TMB) distributes the camera trigger. Like the other non-commercial components, it was developed at the MPI for nuclear physics in Heidelberg. Figure 8.8 shows the trigger management board. A crucial design feature was that the signals from every segment have the same propagation time through the board. Therefore all inputs and outputs are distributed in a circle around the main computing device. The transition time through the TMB follows a Gaussian distribution with a standard deviation of ~ 0.2 ns.
The design of the TMB also aimed for a minimal transit time for the trigger signals. This is crucial because the analog signal from the PMT has to be stored

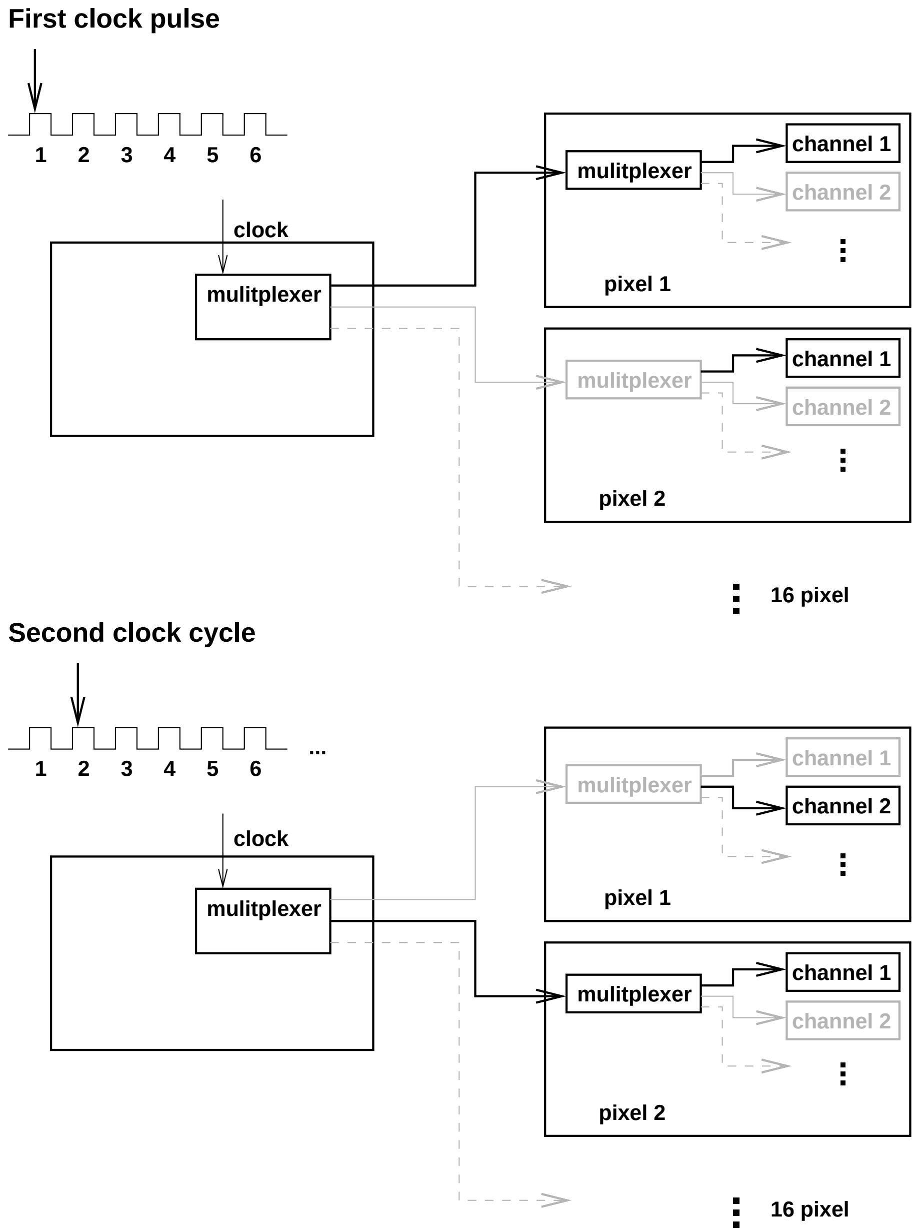
First clock pulse
1 2 3 4 5 6
clock
mulitplexer
mulitplexer
channel 1
channel 2
pixel 1
mulitplexer
channel 1
channel 2
pixel 2
16 pixel
Second clock cycle
1 2 3 4 5 6 ...
clock
mulitplexer
mulitplexer
channel 1
channel 2
pixel 1
mulitplexer
channel 1
channel 2
pixel 2
16 pixel

FIGURE 8.7: Multiplexing scheme of the readout. The black channel denotes the active channel which is connected to the FADC. The clock and strobe line from the segment controller to the pixel and the signal line from the pixel to the segment controller are not drawn.

until the trigger decision is made (see section 8.1.2).
The input of the trigger can be set to different channels. These are internal, external, pedestal and monitor trigger. The internal trigger is the normal operation mode of a camera of an IACT. In this mode a camera trigger is generated when a trigger signal from the pixels arrives at the TMB. As mentioned before (see section 8.1.1) a pixel generates a trigger signal when a programmable

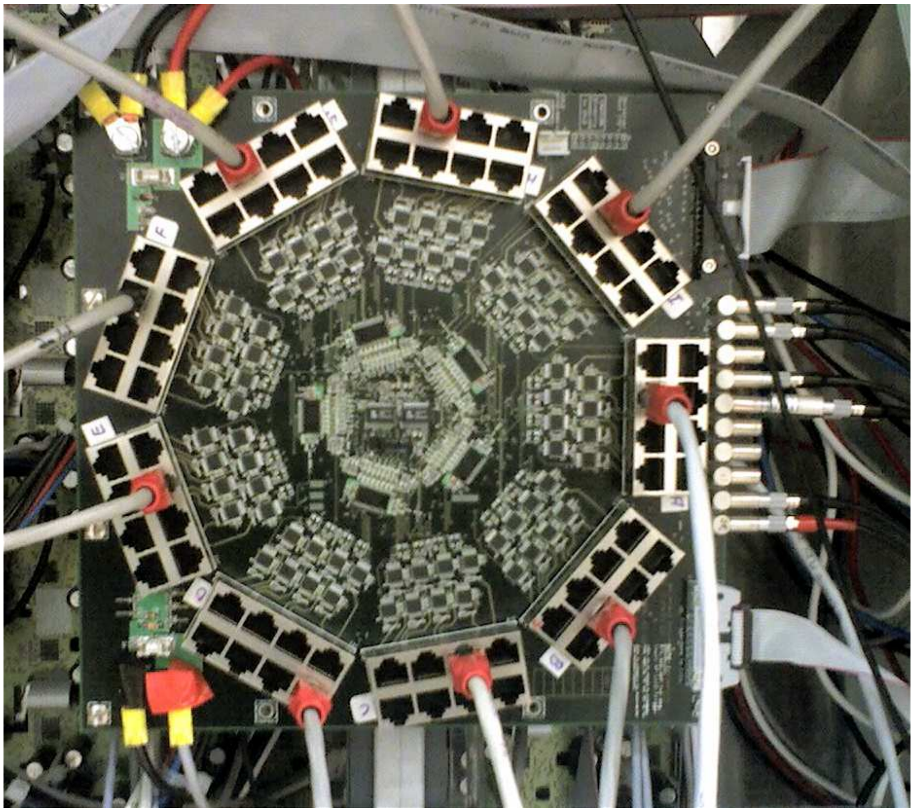

FIGURE 8.8: Trigger Management Board. The design aimed for homogeneous propagation time of the trigger signals. Therefore the inputs and outputs of the trigger signals are distributed around the main processing device in the middle of the board.

number of neighboring pixels have registered a PMT signal exceeding the set threshold. In the external trigger mode a camera trigger is generated and sent to the pixels when a TTL signal reaches the associated input channel. The external trigger signal can be delayed up to 512 ns in steps of 2 ns. This mode is used to calibrate the programmable delays in the SPC and the time measurement on the pixels. It is also used to to readout the camera temporal correlated to a light source. The pedestal trigger mode is used to monitor the pedestals of the different measurement channels.

The TMB has a latched register, which stores the information on which segment the trigger occurred. In addition a template can be set to check whether pixels on a certain combination of segments have generated trigger signals in the same time (within few nanoseconds).

The TMB is controlled by the camera controller. In the programming it is treated like an additional segment.

8.5 Housing

The housing of the prototype is a self supporting aluminum structure being capable to take 1022 pixel. It is equipped with 12 fans to keep the temperature in a acceptable range. The dimensions are 160 cm × 180 cm. Fully equipped with pixels it will have a weight of ~ 850 kg.

8.6 Software

To perform the test on the SPC prototype a system software was developed. The software was designed to be capable to perform all tasks, a Cherenkov telescope camera is confronted with. Because of several different tasks the camera has to compute at the same time the software was developed with multi-thread methods. This means that the software runs several programs in parallel which communicate over software interfaces. The program, monitoring the temperature, should run regardless of what the rest of the software is doing and be able to switch off the camera or at least to print out warnings on the monitor in the test phase. A monitor program was implemented which shows the actual values in the different pixel channels. This is very useful to find and characterize malfunctions in the prototype.

The main program, controlling the readout and the setting the commands on the hardware, was developed modular to simplify the development and maintenance of the program.

Chapter 9

Tests with the Prototype

In the frame of a diploma thesis (Hauser, 2004) the design and the properties of the pixel electronics was tested and improved. The tests concentrated on the performance of the SPE and the connection to the next neighbors. The next step was the systems integration of a prototype camera. The number of pixels of the prototype was chosen in a way that the tests on the prototype reflect the performance of a camera with up to $\sim$ 1000 pixels. The minimal number of pixels for such a prototype is 128. To reduce the costs in the case of a major problem in the pixel electronics the first test were performed with 64 pixel. Figure 9.1 shows the prototype camera used for the tests. The mechanics of the prototype is capable to host up to 1022 pixels. The 128 test pixels can

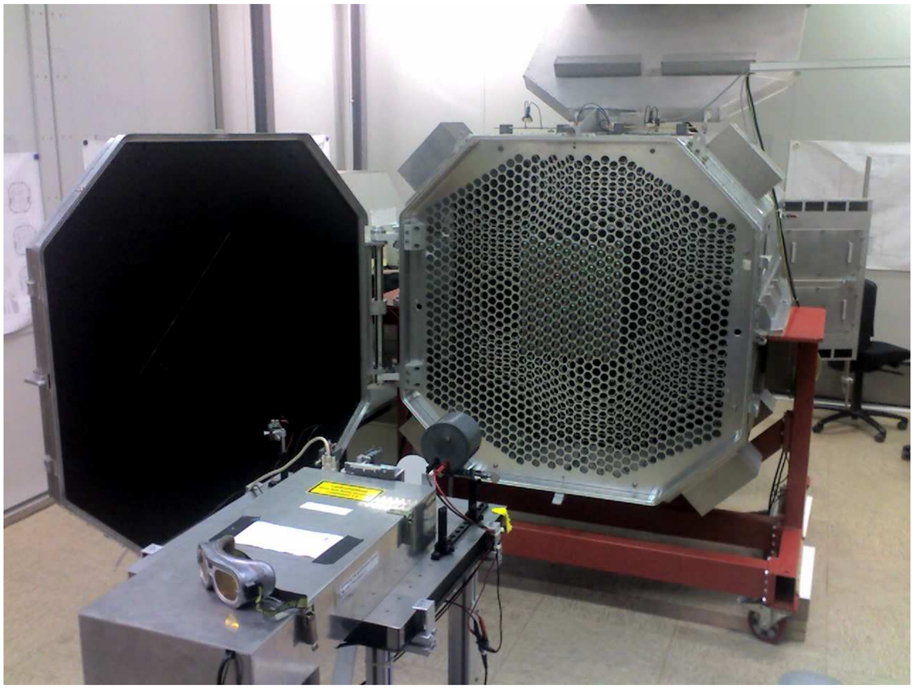

FIGURE 9.1: Camera prototype with 128 pixels.

be seen in the middle of the camera. In the foreground the test bench for the simulation for the light contributions in a telescope can be seen (see also Figure 9.2).

To operate the camera during the tests, a system software was developed which is capable to set all parameters and operate the camera in the different operation modes.

During this work many new test methods have been developed, which allow the precise and detailed understanding of the camera properties. Some of the most important measurements to calibrate the camera are shown in this chapter.

9.1 Test Bench

A test bench was build in the lab, to simulate the different light conditions to which a camera is exposed in a telescope (see Figure 9.2). This was done to characterize the properties of the camera under controlled conditions. The short (in the order of nanosecond) light pulsed expected from air showers are simulated using pulsed LEDs driven by fast amplifiers. The LEDs can be triggered with rates up to $O(100\,\text{kHz})$. At a distance of 2.5 m the light yield is adjustable from ~ 1 p.e./pixel up to about 40 p.e./pixel. The full width at half maximum (FWHM) of the light pulses stays below 5 ns for all intensities. A detailed characterization can be found in Glück (2006).

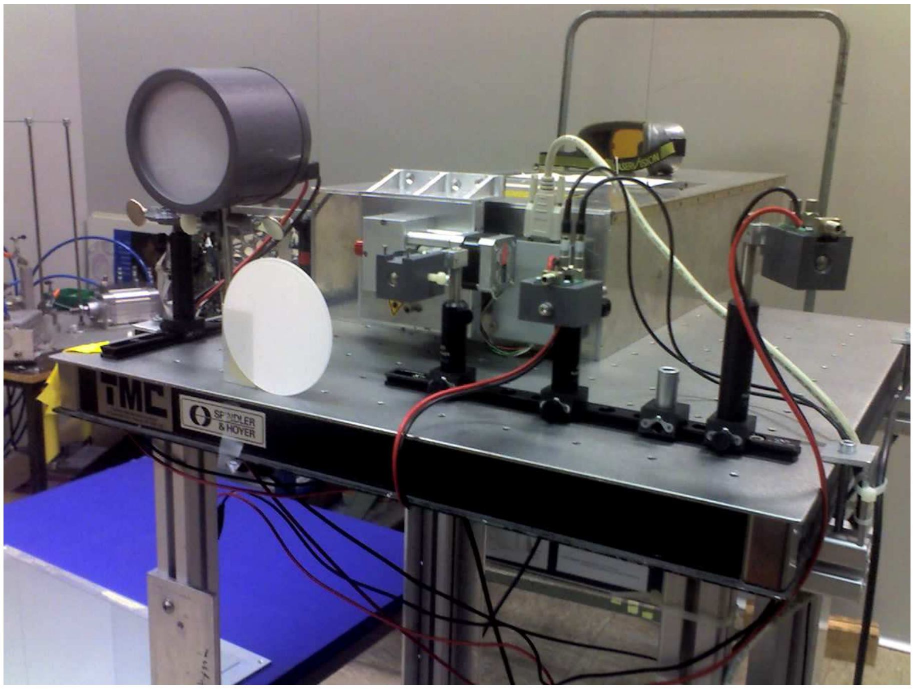

FIGURE 9.2: Test bench to simulate the different light sources a camera in a telescope would be exposed to.

As a second source for the simulation of photons from Cherenkov showers a pulsed nitrogen laser in combination with a scintillator as wavelength shifter, a filter wheel and a diffuser is used. The maximum repetition rate for the laser is in the order of 10 Hz. The FWHM of the light pulse is below 3 ns. The light intensity can be adjusted with a neutral density filter wheel up to $\sim 3000,$p.e.. The NSB light is simulated with a continuous LED in combination with a diffuser. Its intensity can be adjusted computer controlled. The photons from this source arriving at the camera are statistically distributed in time. The maximal rate with which the photons arrive at the pixels is about 10^9 p.e./s.

9.2 Calibration of the Delays

The different delays on the pixels and on the trigger board have to be calibrated and monitored. Therefore methods for the calibration of delays were developed in a way that they can be easily applied routinely also in a completely equipped camera.

Discriminator Delay

The gain of the different PMTs varies from pixel to pixel because of differences in the production and aging. Therefore the gain of the PMTs has to be adjusted by the variation of the high voltage supply. This, however, changes the transit time in the PMTs. The time which is needed to generate and distribute a trigger signal must not depend on the pixel which generated the trigger in the first place. Otherwise the fixed timing on in the SPC would result in phase errors in the signal determination of some pixels. Additionally the trigger logics, which reacts on coincidences in neighboring pixels must rely on a homogeneous transition time through the PMTs of the pixels. The discriminator delay is implemented to ensure a homogeneous timing in the trigger path. The discriminator signal can be delayed up to five nanoseconds in steps of single nanoseconds. In this section it is described how the discriminator delay is calibrated for the whole camera.

The calibration makes use of the possibility to measure the time between a discriminator signal and the camera trigger (Section 8.1.3) on each pixel. The calibration method is illustrated in the top panel of Figure 9.3. One pixel is enabled for the generation of the trigger for the readout of the camera and it therefore provides the start of the time measurement in each pixel. This means that the time, which is measured in the other pixels reveals information about the transition time of the signal in the triggering pixel. The mean of the time values derived by this procedure is written into a table. This is done for all pixels. This means one pixel after an other is enabled to generate the trigger and the rest of the pixels are used to derive the mean of the time values. The variation of the mean values in the table is then minimized by changing discriminator delay of the pixels whose value is more than 0.6 ns away from the mean of all values.

The light pulses for the calibration are generated by the laser. To reduce the effect of different trigger times because of different numbers of photons in the pixels and therefore different rise times the intensity is about 1000 p.e. per pixel.

The discriminator threshold is of the order of a few p.e. The bottom panel of Figure 9.3 shows the distribution of the mean time of all pixels after the calibration. The distribution of the propagation time through the pixels after

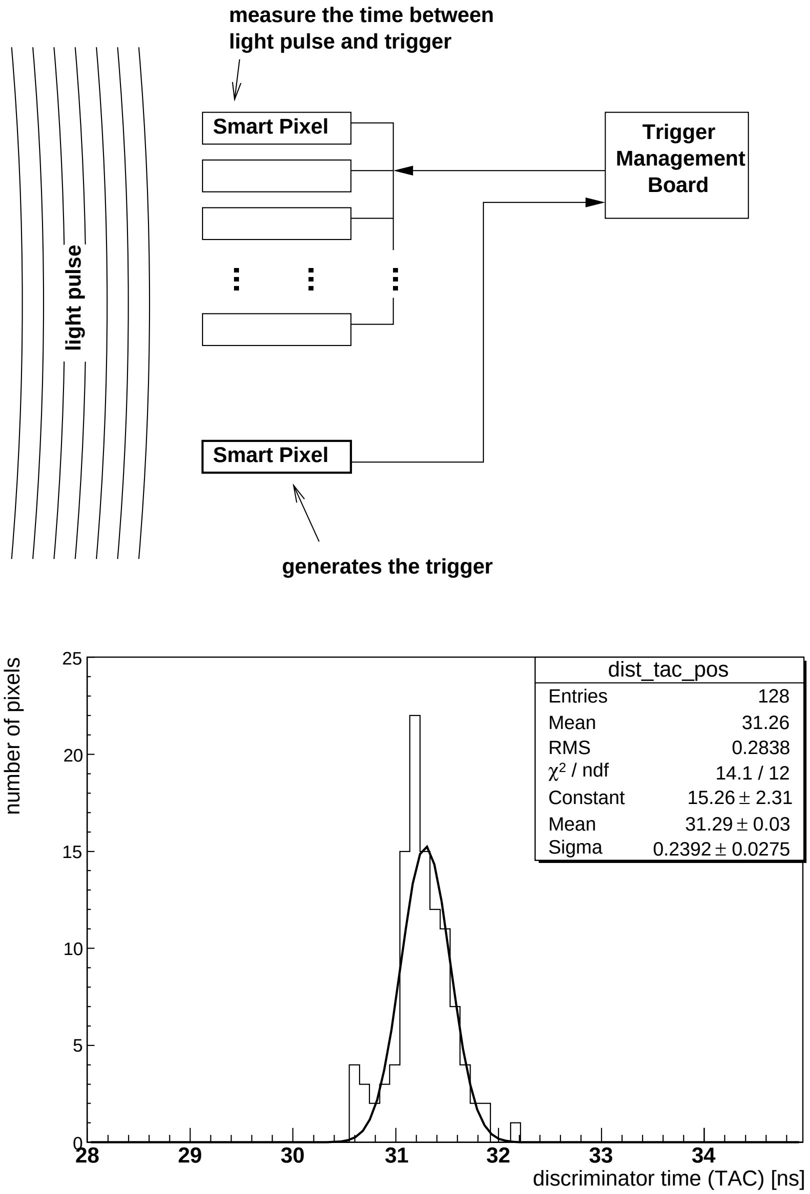

FIGURE 9.3: Calibration of the discriminator delay. *Top:* Calibration method. To measure the trigger timing of one pixel all pixels are illuminated by a bright light pulse and the time information of all pixels is read out. *Bottom:* Distribution of the mean time which is needed for the generation of the trigger signal. The zero of the x-axis is arbitrary.

calibration has a standard deviation (obtained by a Gaussian fit) of $\sim 0.2\,\mathrm{ns}$.

This is the standard deviation of the time which is needed to distribute the trigger for the measured pixels. Therefore, after calibration the duration until the trigger is distributed is within $\sim 0.2\,\mathrm{ns}$ over the field of view of the prototype camera.

Gate Delay

The position of the PMT pulse in the gate has to be optimized to reduce the influence of jitter and background photons. In the first step the relative positions of the gates of all pixels is calibrated. This is done using the trigger input on the trigger management board. The external trigger can be delayed on the trigger management board up to 512 ns in steps of 2 ns. The amplitudes of all pixels are measured as a function of the external delay and the optimal delay (i.e. the delay for which the result of the integration is maximal) is derived. An example is shown in the bottom panel of Figure 9.4. In the top panel of Figure 9.4 a sketch of the principle of the calibration is shown. After calibration the standard deviation of the optimal external delays is 0.4 ns. A variation in the gate positions would result in a phase error. As can be seen in 8.5 a variation of 0.4 ns does not influence the integration.

Trigger Delay

In the calibration of the gate delay the relative positions of the integration gates for all pixels are optimized with the use of an external trigger. The position of the gates with respect to an internal trigger have to be calibrated globally for the whole camera. For this purpose a delay module on the trigger management board is used, which delays the camera trigger before it is sent back to the pixels.

9.3 Amplitude Measurement

9.3.1 Calibration

The aim of the amplitude calibration is to derive the conversion factor from the ADC values into number of photo electrons released at the photo cathode of the PMT for every pixel in the camera. The conversion factors are used in the analysis to calculate the number of p.e. for every pixel in the picture.

The amplitude measurement is calibrated using single photo electron spectra. These are amplitude distributions derived with an illumination of low intensity corresponding to a signal in the PMTs of the order of 1 p.e./pixel. The illumination is generated with the pulsed LEDs. The LEDs and the readout are triggered by the same source with an appropriate relative delay. For the calibration at least two peaks have to be identified by a fit: the *pedestal peak*, originating in readout sequences where no p.e. was emitted at the cathode and the *single p.e. peak*, originating in sequences where exactly one p.e. was emitted.

The amplitude difference between these two peaks, obtained by a fit, is the

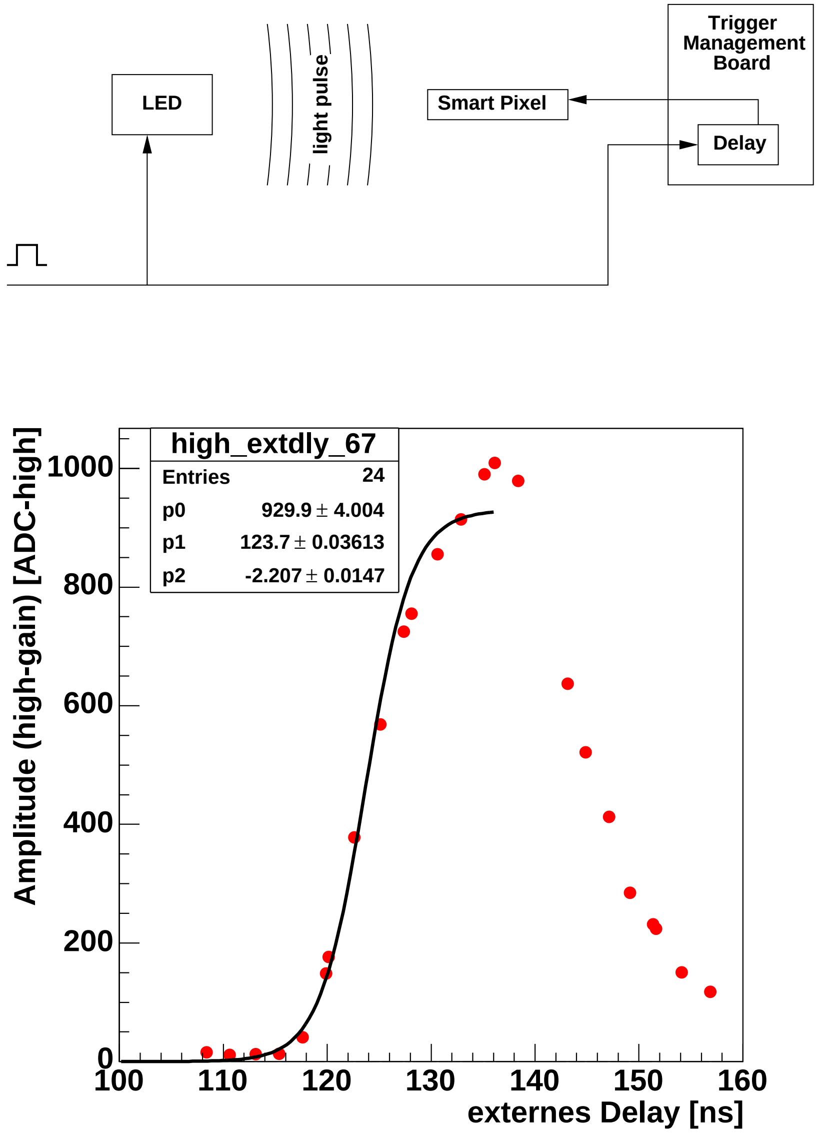

FIGURE 9.4: Calibration of the gate delay. *Top:* Calibration principle. The delay in the trigger management board is varied to find the optimal position of the gate with respect to the PMT pulse. *Bottom:* Example of the amplitude as a function of the delay.

conversions factor from ADC units to p.e. The width of the pedestal peak is the result of electronic noise on the pixel electronic. The width of the single p.e. peak is a result of a combination of electronic noise and fluctuations in the amplification in the PMT.

In Figure 9.5 an example of a single p.e. spectrum is shown. The high voltage of the PMT is set to the standard value to obtain an amplification of $\sim 2 \times 10^5$. One can clearly resolve the two peaks. In addition an indication for

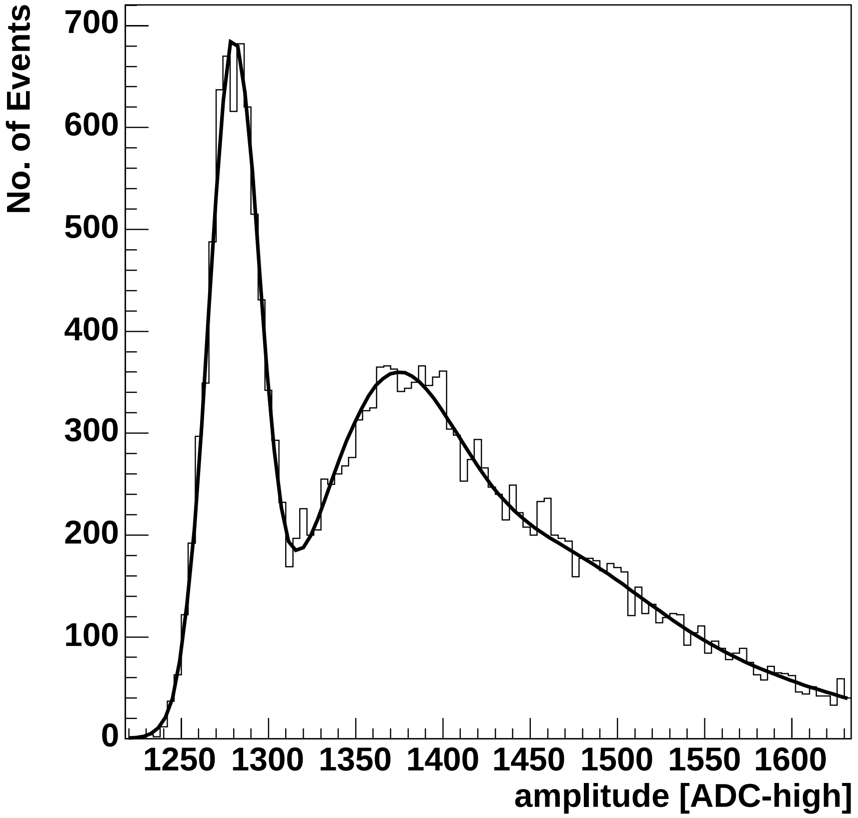

FIGURE 9.5: Single p.e. spectrum of a typical pixel obtained with an integration gate width of 13 ns.

a shoulder, corresponding to two p.e. emitted at the cathode, can be seen at ~ 1480 ADC-Units. This shows, that the Smart Pixel can easily be calibrated using single p.e. spectra. A calibration cycle takes only a few seconds due to the possible readout rates of the order of kHz.

9.3.2 Amplitude Resolution

The resolution of the amplitude measurement is obtained using the pulsed LED for amplitudes up to ~ 40 p.e. and the pulsed laser for amplitudes beyond this value. At different intensities 1000 events each, are taken. The amplitude distribution for each pixel is obtained by comparing the amplitude in the pixel with the mean of the amplitudes in the rest of the pixels for each event. This is done to correct for pulse to pulse variations in the laser intensity. In Figure 9.6 the relative amplitude resolution of one pixel function of the amplitude is shown. The solid line is the expectation from the Poisson distribution of photo electrons emitted at the cathode ($\sqrt{N}/N$). The measured resolution is slightly worse. There are additional contributions to the variation in the amplitude determination. One part is the electronic noise which was already

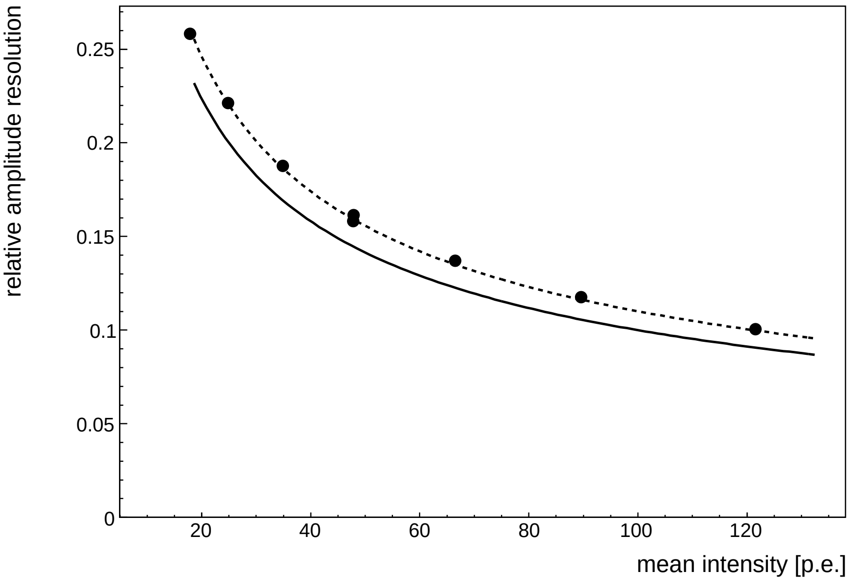

FIGURE 9.6: Relative resolution of the high gain channel for different signal amplitudes for a integration gate width of 13 ns.

seen in the single p.e. spectrum (σ_{el}/N). Another contribution comes from the phase error (see Figure 8.5), which is the displacements of the PMT signals in the integrator (σ_{phase}). The phase error scales with the amplitude. Fluctuations in the amplification of the PMT also worsens the resolution of the amplitude determination. This corresponds to the width of the single p.e. peak (σ_{SPE}/N). For a signal with N p.e. this contributes $\sqrt{N}$ times.
If one takes into account these contributions the resolution is expected to be

$$\begin{aligned} \left(\frac{\sigma_{\mathrm{amp}}}{N}\right)^2 &= \sqrt{\frac{1}{N} + \frac{\sigma^2_{\mathrm{SPE}}}{N} + \frac{\sigma^2_{el}}{N^2} + \sigma^2_{\mathrm{phase}}(\Delta T)} \sim \\ &\sim \sqrt{\frac{1}{N} + \frac{(0.5)^2}{N} + \frac{(0.25)^2}{N^2} + (0.05)^2} \end{aligned} \tag{9.1}$$

The main source for the amplitude variation is the Poisson distribution of the photo electrons. The amplitude resolution of the Smart Pixel is close to the theoretical limit. The difference is within the expectations. Therefore the amplitude measurement of the Smart Pixel is suited for the use in a Cherenkov telescope.

9.3.3 Noise

Due to their statistical arrival time distribution, photons from the NSB exhibit an additional and significant contribution of noise in the image. This is the reason why the integration gate is that short. In contrary to the photons from the shower, which arrive at the camera within a time window in the order of

10 ns, the photons from the NSB arrive with random arrival times. The rate of the typical expected NSB in Namibia was measured by Preuß et al. (2002) to $\sim 10^{12}\,\mathrm{sr}^{-1}\mathrm{s}^{-1}\mathrm{m}^{-2}$. The NSB photons contribute to the width of the pedestal distribution. With increasing NSB rate the width of the pedestal peak increases, as the probability that a NSB photon arrives at the integrator while it is gated for the signal integration increases. Due to AC coupling of the PMT to the electronics, the mean of the pedestal distribution does not change.
As mentioned before the variation of the width of the pedestal peak originates in statistical variations in the number of photo electrons emitted at the cathode and arriving at the integrator while it is gated ($N_{\mathrm{p.e.}}$). The width, which is defined here to be the root mean square (RMS) of the pedestal distribution, is given by $RMS = \sqrt{N_{\mathrm{p.e.}} + \sigma_{\mathrm{el}}^2}$. For a given gate width T_{gate} and a p.e. rate $r_{\mathrm{p.e.}}$ the number of photons in the gate is given by $N_{\mathrm{p.e.}} = T_{\mathrm{gate}} \cdot r_{\mathrm{p.e.}}$. It was here assumed that a signal from a photon electron is either completely in the gate or not at all. This is a good approximation if the gate width is much larger than the pulse width generated by a single p.e.. As this is not exactly the case for the integration gates used here the gate width in the relation above becomes an effective gate width. Following the relation the square of the pedestal width is proportional to the photo electron rate. The proportional factor is the effective gate width for photons from the NSB. The corresponding plot for the nominal gate width of 13 ns is shown in Figure 9.7. The slope of a linear fit to these data points is the effective gate width. Table 9.1 lists the effective gate width obtained with this method for all possible nominal gates on

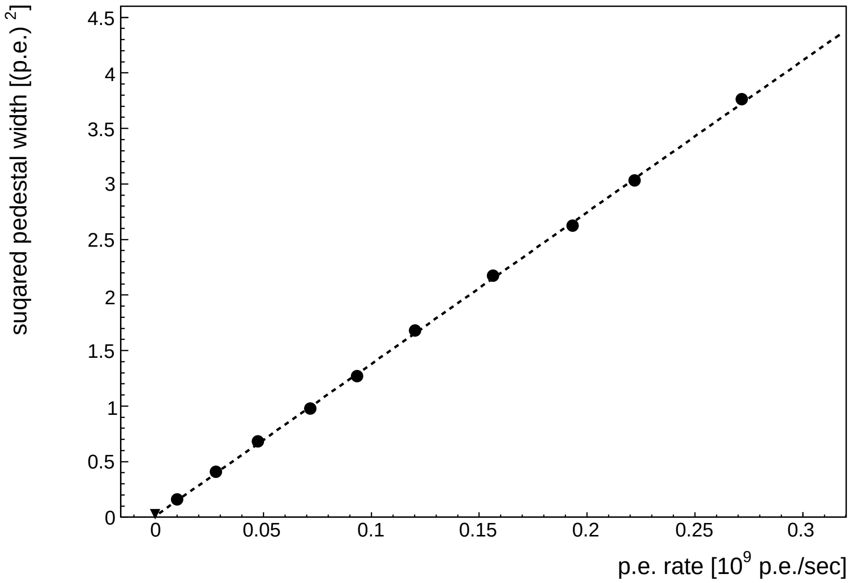

FIGURE 9.7: Square of the mean pedestal width of all pixels as a function of the number of photoelectrons emitted at the cathode per second with a integration gate width of 13 ns. The p.e. rate was determined by the PMI.

the Smart Pixel. The effective gate width is consistent with the nominal gate width. The difference could originate in different nominal gate widths on the pixels (e.g. measurements for a set width of 10 sn gave a range of 10.4 − 11.4 ns). A more realistic model of the integration of parts of pulses would be needed to explore the difference.

adjusted gate width (ns)	effective gate width (ns)
10	11.9
13	13.7
16	15.9
19	18.4
22	20.3
25	22.8

Table 9.1: Effective gates for the night sky background

9.4 Pixel Timing Information

The measurement of the arrival time of the signals in the pixels reveal information of the shower. As the electrons and positron in the shower are faster than the local speed of light, the Cherenkov photons from the bottom of the shower arrive earlier at the telescope than the photons emitted at the top. Therefore every shower image has a time gradient, which depends on the impact parameter. Most of the Cherenkov light from the shower arrives at the camera within a few nanoseconds. To study the time profiles of showers the resolution of the arrival time measurement should therefore be in the sub-nanosecond range.

The TAC on the pixel electronics measures the time of the discriminator signal with respect to the camera trigger signal. As the camera trigger starts the TAC, this information can be used to correct for possible displacements of the PMT signal with respect to the optimal position in the gate.

The TAC is calibrated using a programmable delay module, implemented for that purpose on the trigger management board. The delay module was calibrated using an oscilloscope in the lab (Glück, 2006).

9.4.1 Time Measurement Resolution

For each event and each pixel the amplitude and the discriminator trigger time with respect to the camera trigger (TAC) of the pixel is measured. In the left panel of Figure 9.8 the distribution of the time measurement of one pixel is shown. The right panel Figure shows the resolution of the arrival time measurement as a function of the amplitude for a typical pixel. The measurement was performed using the pulsed diode with an external trigger signal. Close to the threshold (here 5 p.e.) the resolution worsens due to statistical fluctuations of the arrival time of p.e. within the pulse. At higher amplitudes the resolution always stays well below 0.4 ns. The resolution of the arrival time measurement on the SPE is qualified to measure the time profile of Cherenkov showers.

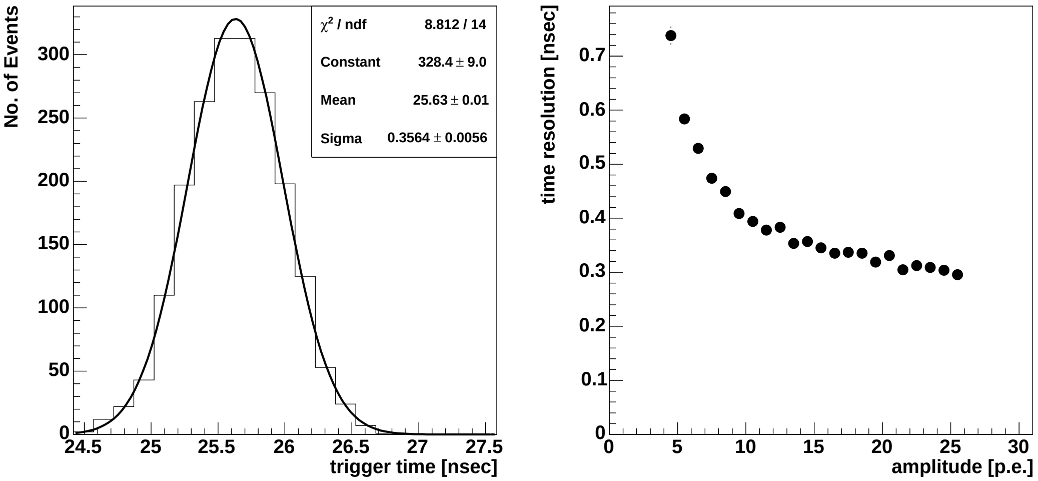

FIGURE 9.8: *Left* Distribution of the time measurement in one pixel *Right* Resolution of the time measurement as a function of the amplitude in the high gain. The threshold of the discriminator set to 5 p.e.

9.4.2 Effective Trigger Gate

The measurement of the arrival time on the pixel can be used to measure the effective gate for coincidences with neighboring pixels. This is done by illuminating the whole prototype camera with diffuse light and trigger on chance coincidences of two pixels. Every readout is then a coincidence by chance of the signals arriving at the pixels. For a given pair in the camera all events are selected for which only these pixels have recorded a signal over the discriminator threshold. This ensures that the trigger originated in the signals of these two pixels. The maximal difference of the arrival times in these pixels in then twice the width of the effective coincidence gate.

9.4.3 Diagnostic Power of the Time Measurement

In this section an example for the diagnostic power of the SPE is given.
The effective trigger gate described in the previous section has to be very short to minimize triggers due to chance coincidences. Therefore the propagation time of the discriminator signals to the PLD and to the neighbors has to be well understood. Figure 9.9 shows the timing of the generation of the trigger for different delays between the PMT signals arriving at the discriminators (for a coincidence in two neighboring pixels). It can be seen that always the later signal determines the time of the trigger. In the design of the SPE the option was foreseen to measure and calibrate the relative timing with the TAC on the pixels. The calibration of the propagation time is done in the PLD. Therefore the signal coming from the internal discriminator is loopthroughed the PLD to delay it until the signals from the neighbors arrive. The left panel of Figure 9.10 shows the measured time of one pixel as a function of the measured time of its neighbor for coincident signals before the calibration. Four branches can

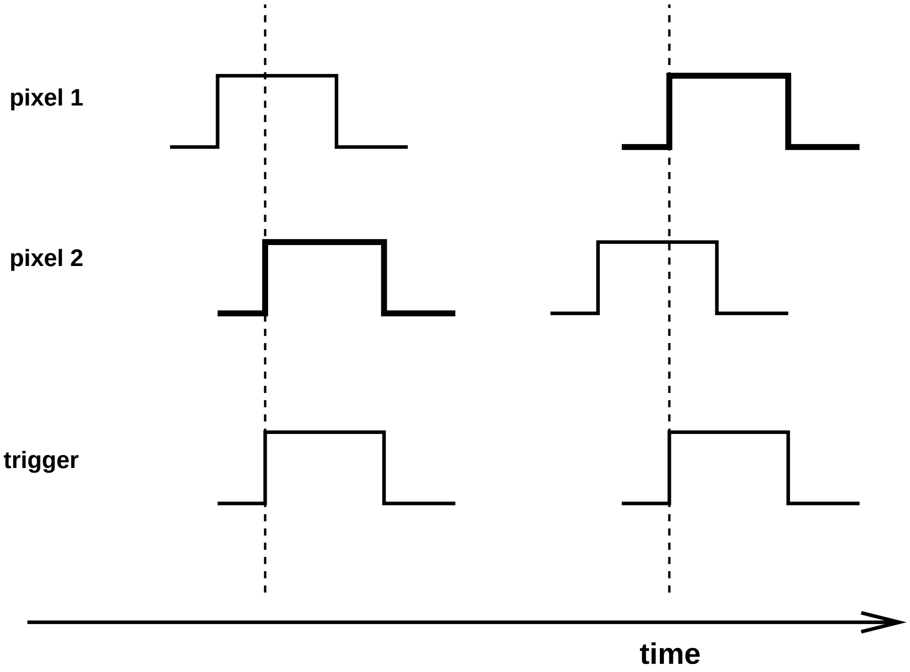

FIGURE 9.9: Trigger timing for a coincidence of two pixels.

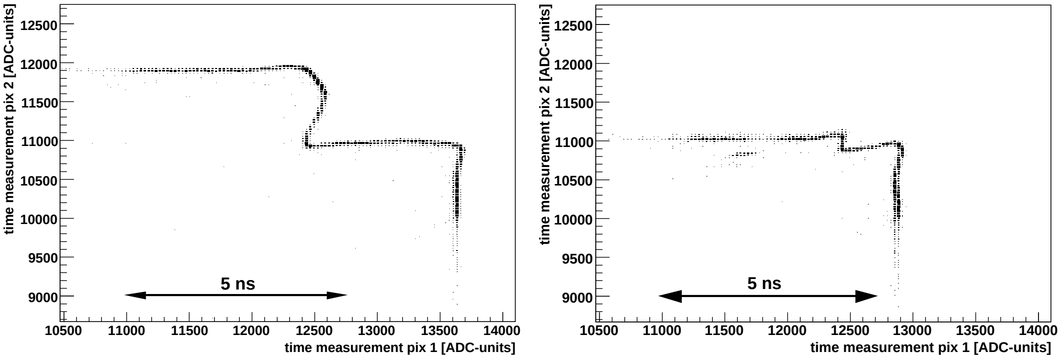

FIGURE 9.10: Arrival time of one pixel versus the arrival time of a neighboring pixel for all coincident events.

be seen in this two-dimensional distribution. A vertical branch corresponds to events where the pixel whose TAC is given on the x-axis determines the timing. The same states for a horizontal branch and the other pixel. The situation shown in the figure can be explained by the assumption that the propagation time of the internal discriminator signal is shorter than the propagation time of the discriminator signal coming from the neighboring pixel. Therefore signals which are coincident for one pixel are not coincident for its neighbor. The right panel of Figure 9.10 shows the distribution after the calibration.

Also with this type of checks, the function of the trigger system of each pixel can be tested in a telescope from dedicated test observations triggering on NSB photons.

9.5 Trigger Performance

The trigger performance of a camera for a Cherenkov telescope is a crucial parameter as the bulk of the photons arriving at the camera are originated in the NSB. In the amplification of the PMT three effects can produce signals which can induce to the generation of discriminator signals by the pixel electronics. These are pile-up of photon signals, fluctuations in the amplification and especially after-pulses from the PMTs.

9.5.1 Pixel Threshold

The trigger threshold and efficiency should be homogeneous over the focal plane. Inhomogeneities would result in a lower overall trigger efficiency or could result in systematic effects on astronomical observations. Therefore the discriminator thresholds on the pixels must be well calibrated as they are the first level of the camera trigger. In the SPC this calibration can be done in normal operation mode.

In the lab the threshold is calibrated by illuminating the pixels with the pulsed LED with different intensities. The readout of the camera is triggered by an external signal in temporal correlation to the pulsed light such that the PMT pulse fits optimal into the gate. As mentioned before the TAC measurement provides the information whether a pixel has recorded a signal above the discriminator threshold (Section 8.1.3).

The main window of Figure 9.11 shows the amplitude distributions of all events (dash-dotted line) and of the events when the discriminator triggered (solid line). The ratio of the solid histogram and the dashed-dotted histogram shows the shape of the threshold. The threshold is defined as the amplitude at which 50% of the events are registered by the discriminator. The width of the threshold is defined as the difference in the amplitudes at which 10% and 90% of the events exceed the discriminator threshold, respectively. An example for a threshold distribution around 6 p.e. is shown in Figure 9.12 in the left panel. The right panel shows the corresponding distribution of width of the threshold. In the range of 4 p.e. to 6 p.e. the width is in the order of only $1.0 - 1.5$ p.e..

9.5.2 Discriminator Rate

The measurement of the discriminator rate is calibrated using a counter on the camera controller. The prototype camera is illuminated with diffuse light and each pixel, one at a time, is activated for the generation of a trigger signal. The counter is used to count the number of camera trigger signals. This number is compare with the ADC value measured on the pixel electronics. The different rates needed for the calibration are achieved by varying the illumination or the discriminator threshold.

Figure 9.13 shows the discriminator rate as a function of the discriminator

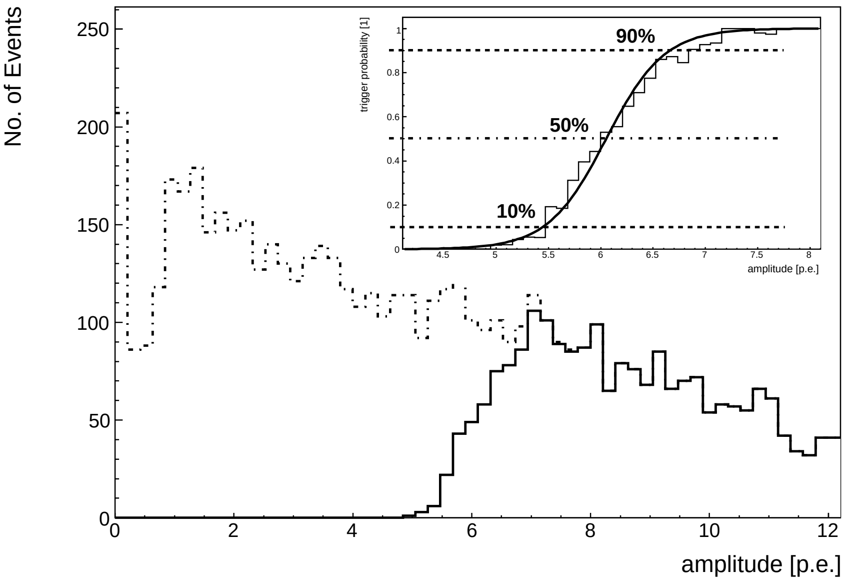

FIGURE 9.11: *Main window*: amplitude distribution of all events (dash-dotted line) and only of events exceeding the discriminator threshold of that pixel (solid line). *Small window*: determination of the threshold. This plot is obtained by calculating the ratio of the amplitude distribution of the events that exceeded the pixel threshold and the amplitude distribution of all events. By definition the threshold is the amplitude where 50% of the events generate a first level trigger. It is marked in the plot by a dash-dotted line. In addition the 10% and the 90% level are plotted; these can be used to define the width of the threshold.

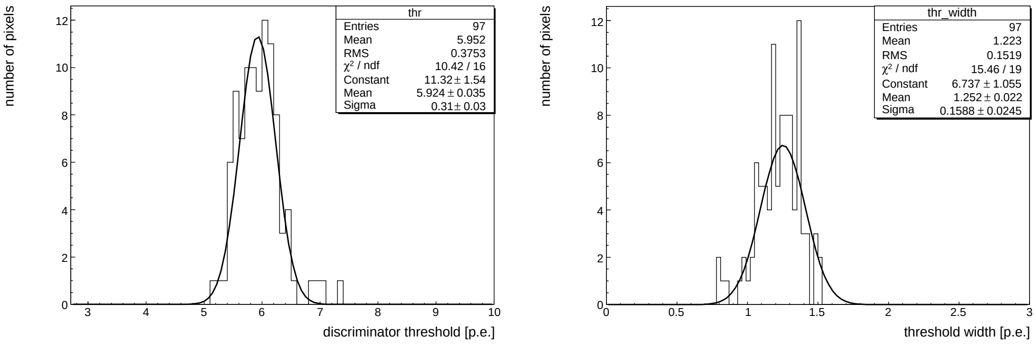

FIGURE 9.12: Distribution of the threshold and its width on 97 pixels for set a nominal threshold.

threshold. There are two main regions visible in the figure. At higher thresholds the rate is dominated by after-pulsing of the PMTs. For lower thresholds the pile-up and triggers due to gain fluctuations in the PMT contribute to the discriminator rate. This behavior is normal for detectors based on PMTs.

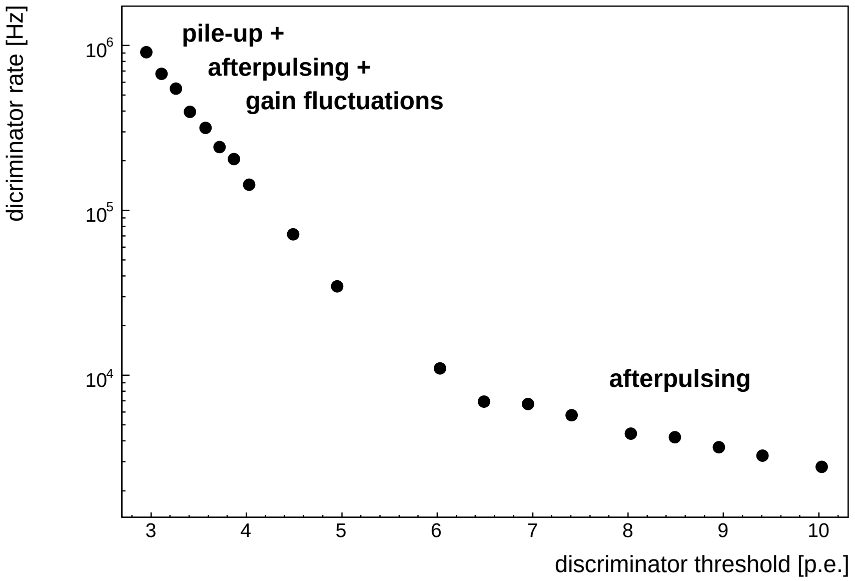

FIGURE 9.13: Rate of the discriminator signals over the discriminator threshold for a photo electron rate of $\sim 100\,\text{MHz}$.

9.5.3 Accidental Rate

Coincidences by chance of photons from the NSB on neighboring pixels can produce camera trigger when the threshold is only a few p.e. The measurement of the discriminator rates on the pixels is used to calculate the expected trigger rate because of these coincidences. This calculated rate is used to study the trigger system of the pixel by comparing it with the measured rate. It is assumed here that the photons from the NSB are statistically distributed. Only the case of coincidences in two neighboring pixels is discussed as coincidences of NSB signals in more that two pixels are unusual.

A pair of pixels with the discriminator rates r_i and r_j, respectively, and the effective coincidence gate T_{ij} creates camera triggers with a rate $R_{ij} = 2 \cdot r_i \cdot r_j \cdot T_{ij}$. The trigger rate of the whole camera is then the sum over all pairs of neighboring pixels in the camera $R = \sum_{i \neq j} R_{ij}$.

The comparison of the calculated trigger rate and the measured trigger rate allows to test for correlations in the electronics. If discriminator signals on neighboring pixels are correlated the measured trigger rate is greater than the calculated one. Comparisons of these two rates have shown no correlation down to 4 p.e. at an illumination corresponding to a anode current of $2\,\mu\text{A}$, which is a rate of $\sim 6 \times 10^7\,\text{s}^{-1}$.

9.5.4 Dead Time

As a result of the two memory banks in the FADC, which can be accessed asynchronous the dead time has two different regimes. For low rates the dead time is dominated by the digitization of the different channels on the 16 pixels of every segment, which takes $\sim 5 - 9 \mu$s per event. For higher rates the digitized data can not be read fast enough from the memory bank of the FADC. A model was developed to calculate the expected dead time over the whole range. Figure 9.14 shows the result of the model. The dead time of the prototype is

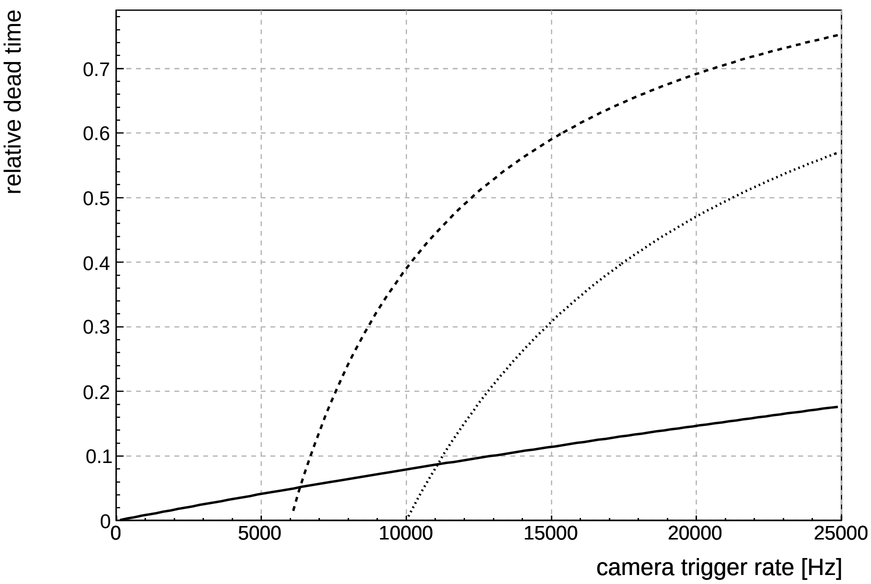

FIGURE 9.14: Calculated relative dead time as a function of the camera trigger rate for 1000 pixels. The solid line shows the deadtime due to digitization. The dashed line is the deadtime as a result of the reading of the digitized information from the memory bank of the FADC. In the case of two VME systems the regime, in which the dead time is dominated by the readout, is shifted to higher rates. This is shown by the dottet line which corresponds to the readout of the digitized date from the FADC in a camera with two VME systems.

dominated by the digitization up to ~ 6.3 kHz. At this rate, the dead time is only $\sim 6\%$ independent on the number of pixels. For higher rates the network bandwidth is dominating. For a rate of 10 kHz the dead time becomes $\sim 40\%$. The Smart Pixel camera could also be equipped with two VME systems resulting in a shift of the transition point (between digitization dominated and network dominated) to ~ 11 kHz. The resulting dead time at a rate of 10 kHz would be $\sim 9\%$.

Conclusion

In this work the analysis of three supernova remnants, Kepler's SNR, Vela Junior and SN1006 was presented. Additionally, a prototype of a new type of camera for future Cherenkov telescopes was set up and tested.

The analysis of Kepler's SNR showed no gamma-ray excess with data having a live time of 13 hrs. However, the derived upper limits could be used to constrain the total energy in accelerated protons. In the framework of a theoretical model of the gamma-ray emission of Kepler's SNR a lower limit on the distance close to an existing upper limit could be given. Furthermore, it was shown that for the high magnetic field expected to be present in the remnant any gamma-ray emission which would detected by a H.E.S.S.-like experiment would most likely be produced by accelerated protons.

Further observations of Kepler's SNR will help to reveal the type of the progenitor and the distance of this remnant.

In the analysis of Vela Junior the morphology of this widely extended source was studied. With a fit of a toy model to the radial profile, a width for the gamma-ray emitting shell could be derived. X-ray data from ASCA could be shown to be compatible with the gamma-ray emission. It could be shown that in a purely hadronic scenario the energy of the accelerated protons would have to be unreasonably large and therefore this model has to be questioned.

The third supernova remnant which was analyzed is SN1006. A significant excess at the north-eastern rim of the remnant was obtained. To the author's knowledge SN1006 is the faintest source of VHE gamma rays ever detected. The analysis of the whole data set on SN1006 will reveal interesting details of the gamma-ray emission. Especially an upper limit on the emission from the south-western spot in comparison with X-ray data could give new insights into the physics in the remnant.

In the second part of this work a new type of camera for future large arrays with multiple Cherenkov telescopes was presented. First the implementations of the different functions of the camera were discussed. Second the system integration and the main tests were shown. The tests could show that such a camera is well-suited to operate the expected tasks in a Cherenkov telescope of the next generation.

Bibliography

F. A. Aharonian. *Very high energy cosmic gamma radiation : a crucial window on the extreme Universe*. Very high energy cosmic gamma radiation : a crucial window on the extreme Universe, by F.A. Aharonian. River Edge, NJ: World Scientific Publishing, 2004, 2004.

F. A. Aharonian and A. M. Atoyan. Broad-band diffuse gamma ray emission of the galactic disk. *Astronomy and Astrophysics*, 362:937–952, October 2000.

F. A. Aharonian, A. M. Atoyan, and T. Kifune. Inverse Compton gamma radiation of faint synchrotron X-ray nebulae around pulsars. *MNRAS*, 291: 162–176, October 1997.

F. Aharonian et al. Calibration of cameras of the H.E.S.S. detector. *Astroparticle Physics*, 22:109–125, November 2004a.

F. Aharonian et al. Detection of TeV γ-ray emission from the shell-type supernova remnant RX J0852.0-4622 with HESS. *Astronomy and Astrophysics*, 437:L7–L10, July 2005.

F. Aharonian et al. Upper limits to the SN1006 multi-TeV gamma-ray flux from HESS observations. *Astronomy and Astrophysics*, 437:135–139, July 2005.

F. Aharonian et al. A detailed spectral and morphological study of the gamma-ray supernova remnant RX J1713.7-3946 with HESS. *Astronomy and Astrophysics*, 449:223–242, April 2006a.

F. Aharonian et al. Observations of the Crab nebula with HESS. *Astronomy and Astrophysics*, 457:899–915, October 2006b.

F. Aharonian et al. H.E.S.S. Observations of the Supernova Remnant RX J0852.0-4622: Shell-Type Morphology and Spectrum of a Widely Extended Very High Energy Gamma-Ray Source. *ApJ*, 661:236–249, May 2007.

F. A. Aharonian et al. High-energy particle acceleration in the shell of a supernova remnant. *Nature*, 432:75–77, November 2004b.

G. Allen. Evidence of 10-100 TeV Electrons in Supernova Remnants. In *International Cosmic Ray Conference*, volume 3 of *International Cosmic Ray Conference*, pages 480–+, August 1999.

D. W. Arnett. A Possible Model of Supernovae: Detonation of ^{12}C. *Astrophysics and Space Science*, 5:180–+, 1969.

B. Aschenbach. Discovery of a young nearby supernova remnant. *Nature*, 396: 141–142, November 1998.

B. Aschenbach, A. F. Iyudin, and V. Schönfelder. Constraints of age, distance and progenitor of the supernova remnant RX J0852.0-4622/GRO J0852-4642. *Astronomy and Astrophysics*, 350:997–1006, October 1999.

W. Baade. Nova Ophiuchi of 1604 AS a Supernova. *ApJ*, 97:119–+, March 1943.

W. Baade and F. Zwicky. Cosmic Rays from Super-novae. *Proceedings of the National Academy of Science*, 20:259–263, 1934.

C. Badenes, K. J. Borkowski, and E. Bravo. Thermal X-Ray Emission from Shocked Ejecta in Type Ia Supernova Remnants. II. Parameters Affecting the Spectrum. *ApJ*, 624:198–212, May 2005.

A. Bamba, R. Yamazaki, T. Yoshida, T. Terasawa, and K. Koyama. A Spatial and Spectral Study of Nonthermal Filaments in Historical Supernova Remnants: Observational Results with Chandra. *ApJ*, 621:793–802, March 2005.

J. F. Beacom and P. Vogel. Can a supernova be located by its neutrinos? *Phys. Rev. D*, 60(3):033007–+, August 1999.

R. H. Becker, A. E. Szymkowiak, E. A. Boldt, S. S. Holt, and P. J. Serlemitsos. Is the remnant of SN 1006 Crablike. *ApJL*, 240:L33–L35, August 1980a.

R. H. Becker, N. E. White, E. A. Boldt, S. S. Holt, and P. J. Serlemitsos. X-ray spectrum of Kepler's supernova remnant. *ApJL*, 237:L77–L79, May 1980b.

A. R. Bell. The acceleration of cosmic rays in shock fronts. I. *MNRAS*, 182: 147–156, January 1978.

E. Berezhko. Nonlinear Kinetic Theory of Cosmic-ray Acceleration in Supernova Remnants. *Space Science Reviews*, 99:295–304, October 2001.

E. G. Berezhko, L. T. Ksenofontov, and H. J. Völk. Gamma-ray emission expected from Kepler's supernova remnant. *Astronomy and Astrophysics*, 452:217–221, June 2006.

D. Berge. *A detailed study of the gamma-ray supernova remnant RX J1713.7-3946 with H.E.S.S.* PhD thesis, Ruprecht-Karls-Universität Heidelberg, 2006.

D. Berge, S. Funk, and J. Hinton. Background modelling in very-high-energy γ-ray astronomy. *Astronomy and Astrophysics*, 466:1219–1229, May 2007.

W. P. Blair, P. Ghavamian, K. S. Long, B. J. Williams, K. J. Borkowski, S. P. Reynolds, and R. Sankrit. Spitzer Space Telescope Observations of Kepler's Supernova Remnant: A Detailed Look at the Circumstellar Dust Component. *ApJ*, 662:998–1013, June 2007.

O. Bolz. *Absolute Energiekalibration der abbildenden Cherenkov-Telescope des H.E.S.S. Experiments und Ergebnisse erster Beobachtungen des Supernova-Überrests RX J1713.7-3946*. PhD thesis, Ruprecht-Karls-Universität Heidelberg, 2004.

C. P. Burgess and K. Zuber. Footprints of the newly discovered Vela supernova in Antarctic ice cores? *Astroparticle Physics*, 14:1–6, August 2000.

E. Cappellaro, R. Evans, and M. Turatto. A new determination of supernova rates and a comparison with indicators for galactic star formation. *Astronomy and Astrophysics*, 351:459–466, November 1999.

G. Cassam-Chenaï, A. Decourchelle, J. Ballet, U. Hwang, J. P. Hughes, R. Petre, and et al. XMM-Newton observation of Kepler's supernova remnant. *Astronomy and Astrophysics*, 414:545–558, February 2004.

A. Daum et al. First results on the performance of the HEGRA IACT array. *Astroparticle Physics*, 8:1–2, December 1997.

A. Decourchelle and J. Ballet. Modeling the X-ray spectrum of Kepler's supernova remnant. *Astronomy and Astrophysics*, 287:206–218, July 1994.

A. Decourchelle and R. Petre. Determination of the thermal and non-thermal emissions in the X-ray spectrum of Kepler's supernova remnant. *Astronomische Nachrichten*, 320:203–+, 1999.

J. R. Dickel, R. Sault, R. G. Arendt, K. T. Korista, and Y. Matsui. The evolution of the radio emission from Kepler's Supernova remnant. *ApJ*, 330: 254–263, July 1988.

R. Diehl et al. Radioactive ^{26}Al from massive stars in the Galaxy. *Nature*, 439: 45–47, January 2006.

J. B. Doggett and D. Branch. A comparative study of supernova light curves. *AJ*, 90:2303–2311, November 1985.

E. A. Dorfi. Cosmic Ray Production Rates in Supernova Remnants. *Astrophysics and Space Science*, 272:227–238, 2000.

L. O. Drury, W. J. Markiewicz, and H. J. Voelk. Simplified models for the evolution of supernova remnants including particle acceleration. *Astronomy and Astrophysics*, 225:179–191, November 1989.

K. K. Dyer, S. P. Reynolds, and K. J. Borkowski. Separating Thermal and Nonthermal X-Rays in Supernova Remnants. II. Spatially Resolved Fits to SN 1006 AD. *ApJ*, 600:752–768, January 2004.

G. J. Feldman and R. D. Cousins. Unified approach to the classical statistical analysis of small signals. *Phys. Rev. D*, 57:3873–3889, April 1998.

M. Fich, L. Blitz, and A. A. Stark. The rotation curve of the Milky Way to 2 R(0). *ApJ*, 342:272–284, July 1989.

A. V. Filippenko. Optical Spectra of Supernovae. *Annual Review of Astronomy and Astrophysics*, 35:309–355, 1997.

V. N. Gamezo et al. Thermonuclear Supernovae: Simulations of the Deflagration Stage and Their Implications. *Science*, 299:77–81, January 2003.

F. F. Gardner and D. K. Milne. The supernova of A.D. 1006. *AJ*, 70:754–+, November 1965.

B. Glück. Test und Inbetriebnahme einer Kamera für Cherenkov Teleskope. Master's thesis, Ruprecht-Karls-Universität Heidelberg, 2006.

B. R. Goldstein. Evidence for a supernova, of A.D. 1006. *AJ*, 70:105–+, February 1965.

D. A. Green. Statistical studies of supernova remnants. *MNRAS*, 209:449–478, July 1984.

D. A. Green. Galactic supernova remnants: an updated catalogue and some statistics. *Bulletin of the Astronomical Society of India*, 32:335–370, December 2004.

S. F. Gull. The X-ray, optical and radio properties of young supernova remnants. *MNRAS*, 171:263–278, May 1975.

I. Hatsukade, H. Tsunemi, K. Yamashita, K. Koyama, Y. Asaoka, and I. Asaoka. The X-ray spectrum of Kepler's supernova remnant. *PASJ*, 42:279–286, April 1990.

D. Hauser. Entwicklung und Test einer Smart-Pixel-Kamera für hohe Ausleseraten. Master's thesis, Ruprecht-Karls-Universität Heidelberg, 2004.

HEGRA Collaboration. The time structure of Cherenkov images generated by TeV gamma-rays and by cosmic rays. *Astroparticle Physics*, 11:363–377, July 1999.

A. M. Hillas. Cerenkov light images of EAS produced by primary gamma. In F. C. Jones, editor, *International Cosmic Ray Conference*, volume 3 of *International Cosmic Ray Conference*, pages 445–448, August 1985.

W. Hillebrandt and J. C. Niemeyer. Type IA Supernova Explosion Models. *Annual Review of Astronomy and Astrophysics*, 38:191–230, 2000.

W. Hofmann et al. Comparison of techniques to reconstruct VHE gamma-ray showers from multiple stereoscopic Cherenkov images. *Astroparticle Physics*, 12:135–143, November 1999.

F. Hoyle and W. A. Fowler. Nucleosynthesis in Supernovae. *ApJ*, 132:565–+, November 1960.

A. F. Iyudin, B. Aschenbach, W. Becker, K. Dennerl, and F. Haberl. XMM-Newton observations of the supernova remnant RX J0852.0-4622/GRO J0852-4642. *Astronomy and Astrophysics*, 429:225–234, January 2005.

A. F. Iyudin et al. Emission from ^{44}Ti associated with a previously unknown Galactic supernova. *Nature*, 396:142–144, November 1998.

O. Kargaltsev, G. G. Pavlov, D. Sanwal, and G. P. Garmire. The Compact Central Object in the Supernova Remnant G266.2-1.2. *ApJ*, 580:1060–1064, December 2002.

K. Kinugasa and H. Tsunemi. ASCA Observation of Kepler's Supernova Remnant. *PASJ*, 51:239–252, April 1999.

D. Koester and G. Chanmugam. Physics of white dwarf stars. *Reports of Progress in Physics*, 53:837–915, 1990.

K. Koyama, R. Petre, E. V. Gotthelf, U. Hwang, M. Matsuura, M. Ozaki, and S. S. Holt. Evidence for Shock Acceleration of High-Energy Electrons in the Supernova Remnant SN:1006. *Nature*, 378:255–+, November 1995.

T.-P. Li and Y.-Q. Ma. Analysis methods for results in gamma-ray astronomy. *ApJ*, 272:317–324, September 1983.

M. S. Longair. *High energy astrophysics. Vol.1: Particles, photons and their detection*. High Energy Astrophysics, by Malcolm S. Longair, pp. 436. ISBN 0521387736. Cambridge, UK: Cambridge University Press, March 1992., March 1992.

M. S. Longair. *High energy astrophysics. Vol.2: Stars, the galaxy and the interstellar medium*. Cambridge: Cambridge University Press, —c1994, 2nd ed., 1994.

B. C. Marsden. Summary of information on the position of the supposed supernova of A.D. 1006. *AJ*, 70:126–+, February 1965.

Y. Matsui, K. S. Long, J. R. Dickel, and E. W. Greisen. A detailed X-ray and radio comparison of Kepler's supernova remnant. *ApJ*, 287:295–306, December 1984.

S. Mereghetti. The X-Ray Sources at the Center of the Supernova Remnant RX J0852.0-4622. *ApJL*, 548:L213–L216, February 2001.

J. C. Niemeyer and S. E. Woosley. The Thermonuclear Explosion of Chandrasekhar Mass White Dwarfs. *ApJ*, 475:740–+, February 1997.

G. G. Pavlov, D. Sanwal, B. Kızıltan, and G. P. Garmire. The Compact Central Object in the RX J0852.0-4622 Supernova Remnant. *ApJL*, 559:L131–L134, October 2001.

D. H. Perkins. *Particle astrophysics.* Publications of the American Astronomical Society, 2003.

S. Perlmutter et al. Measurements of Omega and Lambda from 42 High-Redshift Supernovae. *ApJ*, 517:565–586, June 1999.

S. Preuß, G. Hermann, W. Hofmann, and A. Kohnle. Study of the photon flux from the night sky at La Palma and Namibia, in the wavelength region relevant for imaging atmospheric Cherenkov telescopes. *Nuclear Instruments and Methods in Physics Research A*, 481:229–240, April 2002.

S. P. Reynolds and R. A. Chevalier. Nonthermal Radiation from Supernova Remnants in the Adiabatic Stage of Evolution. *ApJ*, 245:912–+, May 1981.

E. M. Reynoso, G. Dubner, E. Giacani, S. Johnston, and A. J. Green. The interior of the SNR RX J0852.0-4622 (Vela Jr) at radio wavelengths. *Astronomy and Astrophysics*, 449:243–250, April 2006.

E. M. Reynoso and W. M. Goss. A New Determination of the Distance to Kepler's Supernova Remnant. *AJ*, 118:926–929, August 1999.

A. G. Riess et al. Observational Evidence from Supernovae for an Accelerating Universe and a Cosmological Constant. *AJ*, 116:1009–1038, September 1998.

A. G. Riess et al. Type Ia Supernova Discoveries at z > 1 from the Hubble Space Telescope: Evidence for Past Deceleration and Constraints on Dark Energy Evolution. *ApJ*, 607:665–687, June 2004.

K. Scholberg. SNEWS: The SuperNova Early Warning System. In S. Meshkov, editor, *American Institute of Physics Conference Series*, volume 523 of *American Institute of Physics Conference Series*, pages 355–+, 2000.

V. Schönfelder et al. ^{44}Ti Gamma-Ray Line Emission from Cas A and RXJ0852-4622/GROJ0852-4642. In M. L. McConnell and J. M. Ryan, editors, *American Institute of Physics Conference Series*, volume 510 of *American Institute of Physics Conference Series*, pages 54–+, 2000.

L. I. Sedov. *Similarity and Dimensional Methods in Mechanics.* Similarity and Dimensional Methods in Mechanics, New York: Academic Press, 1959, 1959.

P. Slane, J. P. Hughes, R. J. Edgar, P. P. Plucinsky, E. Miyata, H. Tsunemi, and B. Aschenbach. RX J0852.0-4622: Another Nonthermal Shell-Type Supernova Remnant (G266.2-1.2). *ApJ*, 548:814–819, February 2001.

A. Smith, A. Peacock, M. Arnaud, J. Ballet, R. Rothenflug, and R. Rocchia. EXOSAT observations of the Kepler supernova remnant. *ApJ*, 347:925–933, December 1989.

F. R. Stephenson and D. A. Green. *Historical supernovae and their remnants, by F. Richard Stephenson and David A. Green. International series in astronomy and astrophysics, vol. 5. Oxford: Clarendon Press, 2002, ISBN 0198507666.* 2002.

T. Tanimori and et al. Recent status of the analyses for stereoscopic observations with the CANGAROO-III telescopes. In *International Cosmic Ray Conference*, volume 4 of *International Cosmic Ray Conference*, pages 215–+, 2005.

T. Tanimori et al. Discovery of TeV Gamma Rays from SN 1006: Further Evidence for the Supernova Remnant Origin of Cosmic Rays. *ApJL*, 497: L25+, April 1998.

H. Tsunemi, E. Miyata, B. Aschenbach, J. Hiraga, and D. Akutsu. Overabundance of Calcium in the Young SNR RX J0852-4622: Evidence of Over-Production of ^{44}Ti. *PASJ*, 52:887–893, October 2000.

J. P. Vallée. Metastudy of the Spiral Structure of Our Home Galaxy. *ApJ*, 566: 261–266, February 2002.

H. J. Völk, E. G. Berezhko, and L. T. Ksenofontov. Magnetic field amplification in Tycho and other shell-type supernova remnants. *Astronomy and Astrophysics*, 433:229–240, April 2005.

T. C. Weekes et al. Observation of TeV gamma rays from the Crab nebula using the atmospheric Cerenkov imaging technique. *ApJ*, 342:379–395, July 1989.

S. Woosley and T. Janka. The physics of core-collapse supernovae. *Nature Physics*, 1:147–154, December 2005.

V. N. Zirakashvili and F. Aharonian. Analytical solutions for energy spectra of electrons accelerated by nonrelativistic shock-waves in shell type supernova remnants. *Astronomy and Astrophysics*, 465:695–702, April 2007.

Danke

Es gibt viele Menschen, deren Unterstützung und Hilfe diese Arbeit zu dem gemacht haben, was sie heute ist. Allerdings sind hiermit nur die guten Dinge gemeint. Für etwaige Fehler und Unstimmigkeiten übernehme ich die volle Verantwortung.
Herr Werner Hofmann, Ihnen danken ich dafür, daß Sie mir die Möglichkeit gegeben haben an sehr interessanten Themen und in einer tollen Kollaboration arbeiten zu können. Danke auch dafür, daß Sie mich so gut betreut haben.
Herr Karl-Tasso Knöpfle, Ihnen danke ich dafür, daß Sie sich bereit erklärt haben als Gutachter meine Arbeit zu bewerten.
German Hermann, danke für die sehr gute Zusammenarbeit beim Aufbau und der Systemintegration der Smart Pixel Camera. Nicht zuletzt Deine Hilfe hat es mir ermöglicht mich in dieses Thema einzuarbeiten. Vielen Dank auch für die vielen Korrekturen während des Zusammenschreibes der Arbeit.
Bernhard Glück, Dir danke ich für die gute Zusammenarbeit und für die vielen sehr sorgfältigen Messungen.
Thomas Schwab, Christian Föhr, Thomas Wagner und Volker Wieder, Euch möchte ich für die sehr gute Zusammenarbeit danken. Wenn es in der Kamera Probleme gab, habt Ihr immer mit Rat und Tat geholfen das Problem zu lösen.
Matthieu Renaud, Dir danke ich dafür, daß Du mir ich unseren Gesprächen über Supernovaüberreste so viel beigebracht hast. Ausserdem möchte ich mich bedanken, daß Du immer ein offenes Ohr hattest, wenn ich mal wieder mit einer Frage oder einem Problem angekommen bin.
Christopher van Eldik, Danke für Deine Korrekturen und die Diskussionen über alle möglichen Bereiche des H.E.S.S. Experiments.
Wystan Benbow, Danke für Deine Hilfe bei all den Problemen und Fragen, die mir in den letzten drei Jahren über den Weg gelaufen sind.
Karl Kosack, Dir möchte ich Danken, daß Du immer ein offenes Ohr hattest, wenn mal was mit der Analyse nicht so klappen wollte. Und Danke auch für die legendären Geburtstagsfeiern.
Ihnen, Herr Heinz Völk, möchte ich für die vielen interessanten Gespräche über Supernovae und deren Überreste danken.
Danke, Kathrin Egberts und Rolf Bühler. Es war toll mit Euch zu arbeiten, aber auch mal nicht zu arbeiten.
Danke, Christoph Deil, für Deine Korrekturen, und dafür, daß Du so ein angenehmer Zimmerkollege bist.
Danken möchte ich auch Dir, Heidelberger H.E.S.S.-Gruppe. Es war und ist toll hier zu arbeiten. Weiter so!

Danke Tina, für die schöne Zeit, die wir miteinander hatten.
Danke, Frau Dr. Carrigan, daß wir zusammen Durchgehalten haben. Und natürlich auch für die Freundschaft nach der Arbeit. ”Monntag 17.43. Es ist kalt, wir haben nichts zu essen, draußen stürmts und wir sind müde ...”
Vielen Dank, Papa und Mama, daß Ihr mich immer unterstützt und immer an mich geglaubt habt in den letzten (fast) 31 Jahren.
Vielen Dank, Marlin, Janik, Anke, Kathrin (Nennung nach aufsteigendem Alter), daß es so viel Spaß macht mit Euch zusammenzusein und daß Ihr mich immer unterstützt habt.

Besonders möchte ich Dir Schicksal und Dir Internet danken, daß Ihr mir geholfen habt meine Isa zu finden.
Und Dir, geliebte Isa möchte ich danken, daß Du mich so sehr unterstützt hast. Es ist wunderbar mit Dir! Bemerkenswert!